The parametrically forced pendulum: a case study in $1\frac{1}{2}$ degree of freedom

H.W. Broer, I. Hoveijn, M. van Noort, C. Simó, G. Vegter

October 5, 2001

Abstract

This paper is concerned with the global coherent (i.e., non-chaotic) dynamics of the parametrically forced pendulum. The system is studied in a $1\frac{1}{2}$ degree of freedom Hamiltonian setting with two parameters, where a spatio-temporal symmetry is taken into account. Our explorations are restricted to sufficiently large regions of coherent dynamics in phase space and parameter plane. At any given parameter point we restrict to a bounded subset of phase space, using KAM theory to exclude an infinitely large region with trivial dynamics.

In the absence of forcing the system is integrable. Analytical and numerical methods are used to study the dynamics in a parameter region away from integrability, where the results of a perturbation analysis of the nearly integrable case are used as a starting point. We organize the dynamics by dividing the parameter plane in fundamental domains, guided by the linearized system at the upper and lower equilibria.

Away from integrability some features of the nearly integrable coherent dynamics persist, while new bifurcations arise. On the other hand, the chaotic region increases.

1 Introduction

We consider a parametrically forced pendulum in a Hamiltonian $1\frac{1}{2}$ degree of freedom setting, given by the equation of motion

$$\ddot{x} = (\alpha + \beta \cos t) \sin x. \tag{1}$$

Here $x \in \mathbb{S}^1$ is the deviation from the upper equilibrium and ranges over the whole circle. The equation is given in 'inverted pendulum format', meaning that $x = 0$ corresponds to the upper equilibrium, i.e., where the pendulum stands up, while $x = \pi$ denotes the lower equilibrium, i.e., where it hangs down. The independent variable is $t \in \mathbb{S}^1$. The parameters α, $\beta \in \mathbb{R}$ correspond to the square of the eigenfrequency of the (free) pendulum at the lower equilibrium, and the amplitude of the forcing, respectively. Indeed, $\alpha = \sqrt{g/\ell}$, where g denotes the gravitational acceleration and ℓ the length of the pendulum. Without loss of generality we restrict to $\alpha, \beta \geq 0$.

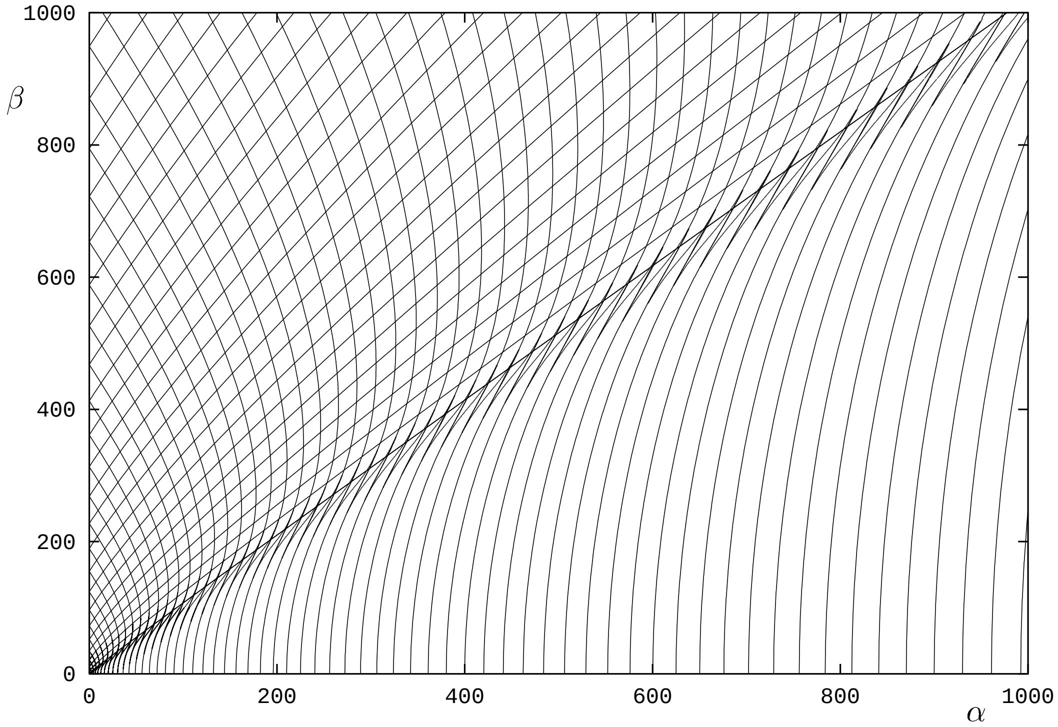

Figure 1: Numerically computed stability diagram of the parametrically forced pendulum (1) on a large scale, revealing a checkerboard structure. On the curves going from the left towards the top side the stability of the upper equilibrium changes, on the curves coming from the α axis the lower equilibrium changes stability. The stable regions above the line $\alpha = \beta$ are extremely small, and not visible at this scale. Below this line the upper equilibrium is unstable and the lower is mostly stable.

This system is widely studied within the context of classical perturbation theory, in several regions in phase and parameter space. The stability of the upper and lower equilibria of the pendulum is determined by the Mathieu equation, that is, the linearized equation at these points. See figure 1 for a stability diagram, also compare van der Pol and Strutt [PS28], Stoker [Sto50], Meixner and Schäfke [MS54], Hale [Hal63, Hal69], Weinstein and Keller [WK85, WK87], Levi et al. [Lev88, LW95], and Broer et al. [BL95, BS98, BS00]. Except near the diagonal $\alpha = \beta$, every line in figure 1 consists, in fact, of two stability curves, that are extremely close together. Hence the stable regions of the upper equilibrium are extremely narrow, as are those of the lower equilibrium above the diagonal, while below this diagonal the unstable regions of the lower equilibrium are very small. At the diagonal, consider up to some $\alpha_{\max}$ the measure of the intervals where the lower equilibrium is stable. It tends to $\alpha_{\max}/2$ as $\alpha_{\max} \to +\infty$, cf. [BLS].

Remark 1 : For large β/α, the Floquet multipliers of the Mathieu equation are extremely sensitive to small changes in the parameters. Therefore, in this region the algorithm that computes figure 1 locates the stability curves by checking for sign changes in these multipliers. Each sign change corresponds to two stability curves, with a narrow stable region in between. Indeed, the multipliers are both $+1$ on one boundary of the stable region, and both -1 on the other boundary. In between they move along the unit circle in the complex plane, while outside the stable regions both multipliers are real, one inside the unit circle, and one outside.

For small β/α the system is nearly integrable. This permits a local nonlinear bifurcation analysis at the two equilibria, near the resonance points of the lower equilibrium on the α axis, see Broer and Vegter [BV92], and near the degenerate point $(\alpha, \beta) = (0, 0)$, see Broer et al. [BHN98, BHNV99].

For sufficiently large velocity $y = \dot{x}$, depending on the parameters, the existence of invariant circles can be shown using KAM theory, e.g., see Moser [Mos89a, Mos89b] and You [You90], also compare Levi [Lev90] for a discussion of a similar system. These circles form a Cantor foliation that tends to full measure as $y \to +\infty$.

1.1 Setting of the problem

The goal of this paper is to explore the coherent (i.e., non-chaotic) dynamics of the forced pendulum, in dependence of the parameters (α, β), as a case study in $1\frac{1}{2}$ degree of freedom. By coherent dynamics we mean all non-chaotic phenomena, that is, all periodic and quasi-periodic dynamics, and their bifurcations. Emphasis lies on orbits of low period, since these usually generate the largest stability islands, cf. [LL92].

In this study we combine perturbation theory and numerical tools, adopting the programme of Broer et al. [BST98]. Indeed, analytical results obtained in certain parameter regions serve as a framework and a starting point for numerical continuation to a larger part of parameter space. Furthermore, at representative parameter points phase portraits are computed. Such an interaction between analytical and numerical methods seems a fruitful approach in the study of systems of this complexity.

Our explorations mostly deal with the Poincaré map P of the forced pendulum, defined on the cylindrical section $t = 0 \bmod 2\pi\mathbb{Z}$. This map has a spatial and a temporal symmetry. For any parameter point (α, β), the coherent dynamics of P at sufficiently large $|y|$ consists of invariant circles with strings of islands in between, as illustrated in figure 3. The islands are very hard to detect, since the largest ones are close to the chaotic domain. As an example, we have plotted a period 4 island in the top right diagram passing through $(x, y) = (0, 0.915)$ (indicated by the arrow). This island intersects the line $x = 0$ between $y = 0.914$ and $y = 0.926$, and goes horizontally from -0.14 to 0.14, where the related hyperbolic period 4 points are located. Figure 2 explains the coding of periodic points and bifurcations that will be used throughout this paper.

This region of invariant circles and small islands thus is well described by KAM theory, and therefore we exclude it from our analysis, thereby restricting to a ‘region

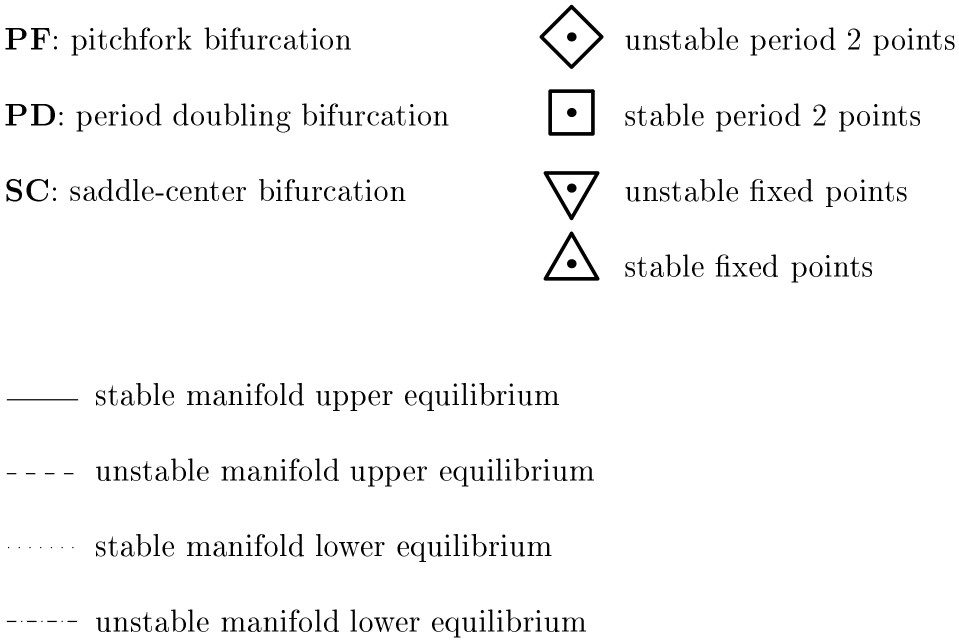

Figure 2: Coding of periodic points, invariant manifolds of equilibria, and bifurcations of the Poincaré map, used in phase portraits, bifurcation and stability diagrams.

of interest' in phase space. (For the free pendulum this coincides with the region between the separatrices.) In this 'region of interest', normal form theory yields an integrable approximation to P, valid for small β/α. This is continued numerically to larger parameter values. As the parameters increase, new bifurcations arise, that are studied as well. Furthermore, the 'region of interest' fills with chaos, and stable and unstable manifolds of saddle points are computed to visualize its structure.

1.2 Method and sketch of the results

Let us describe the results of this paper and the methods by which they are obtained. First the bound on the 'region of interest' is discussed. Then we introduce the concept of fundamental domains in the parameter plane. Finally the dynamics is studied in some of these domains.

Region of interest

As mentioned before, for any parameter point we restrict to a bounded 'region of interest' in phase space. Let us present some quantitative results on the size of this region. It seems to be bounded by $y \approx \pm 2\sqrt{\alpha + \beta}$ for all $(\alpha, \beta) \in \mathbb{R}^2_{\geq 0}$. This estimate follows from a numerical computation on a large part of the parameter plane. The same estimate, valid on parts of the parameter plane, is obtained by adiabatic theory. The estimate is very accurate for large α and β, but not so good near the origin of the parameter plane. We observe that for most (α, β) the 'region of

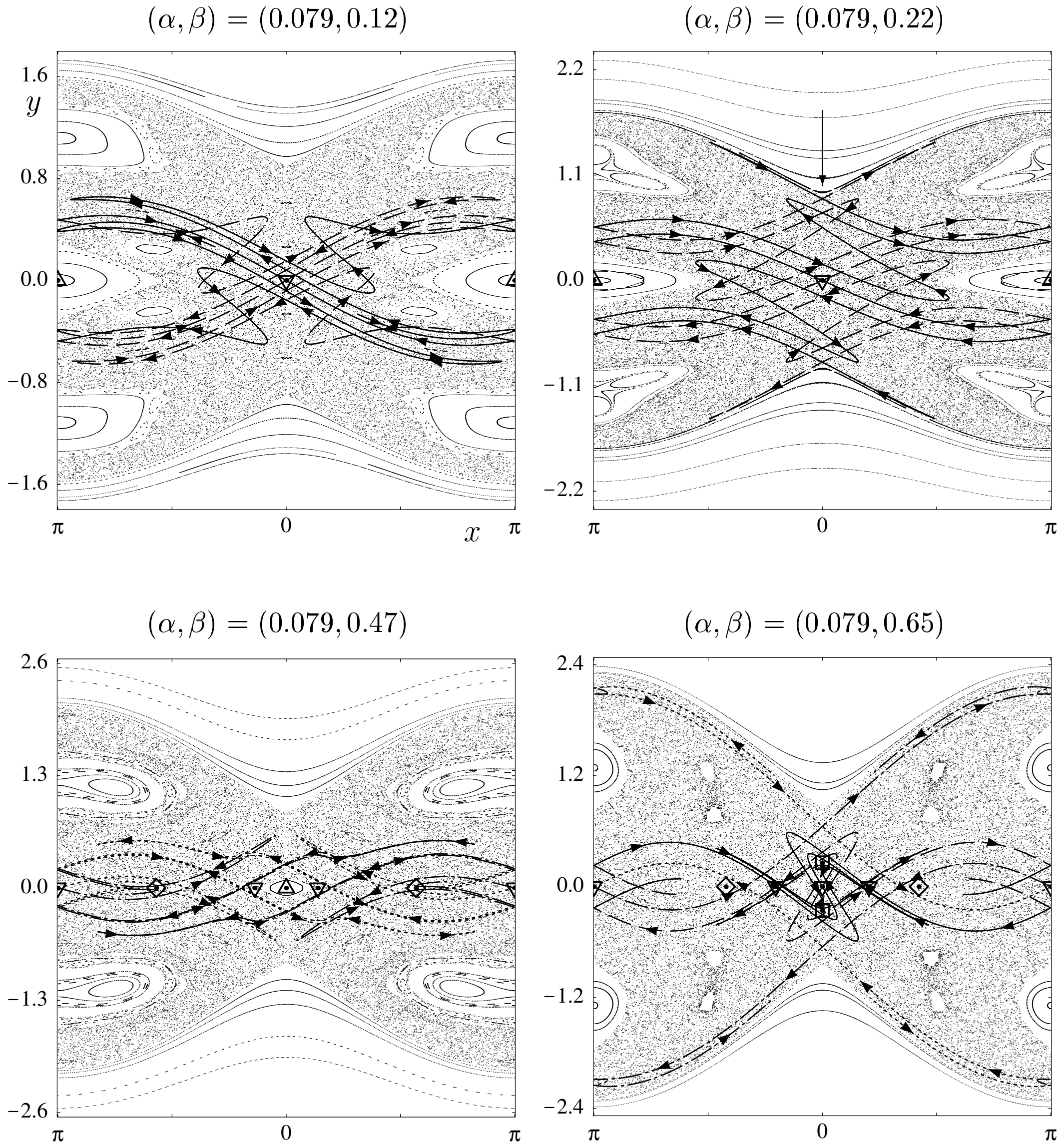

Figure 3: Phase portraits of the Poincaré map at $\alpha = 0.079$ and various β, as indicated. Outside a 'region of interest', the dynamics consists mainly of invariant circles winding around the cylinder. Inside, chaos increases with β, but coherent dynamics remains present. Both equilibria undergo period doubling and pitchfork bifurcations. Parts of invariant manifolds of (unstable) equilibria are also plotted. Invariant manifolds and periodic points born at the equilibria are marked according to the coding in figure 2. In some diagrams there are unmarked stable fixed points above and below the lower equilibrium, corresponding to resonant orbits of the vector field X with frequency 1 in the x-direction. In the bottom left diagram, these fixed points have destabilized in a period doubling bifurcation. For more details, we refer to sections 1.1 and 1.2.

interest' also includes orbits that in the integrable case $\beta = 0$ lie outside this region. For example, the large stable domains above and below the lower equilibrium in the phase portraits of figure 3 lie inside the 'region of interest', but correspond to a resonant invariant circle with rotation number one in the integrable system.

A rigorous bound on the 'region of interest' can be obtained by quantitative KAM theory. We pass to action-angle coordinates to get a well-defined perturbation problem, where the *fast* pendulum, with unbounded y, α and β, is the unperturbed case. We sketch how such a bound can be computed, for more concrete results referring to future research, cf. [BNS].

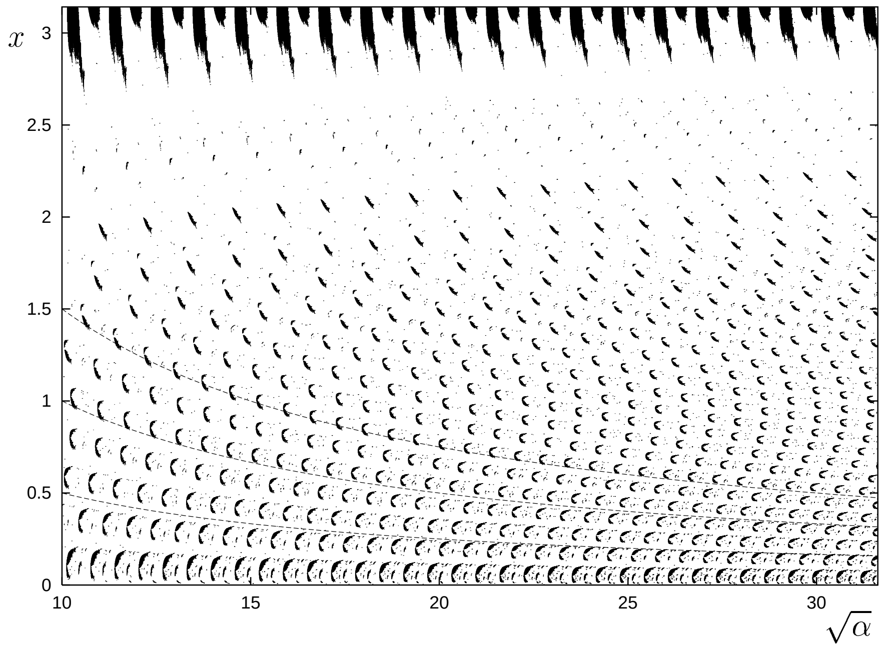

Figure 4: The location of coherent dynamics on the x-axis in phase space, plotted against $\sqrt{\alpha}$ on the line $\beta = \alpha$. The pattern of 'lobsters' is organized approximately in rows $x = \text{constant}/\sqrt{\alpha}$, as indicated by dashed curves.

Inside the 'region of interest' we estimate by numerical means the relative measure of coherent dynamics. For low parameter values this is correlated to large stable islands entering the region at its boundary, while for large α and β coherent regions near the x-axis and the line $x = \pi$ play an important role. Figure 4 displays the location of coherent dynamics on the x-axis as a function of $\sqrt{\alpha}$, on the parameter line $\beta = \alpha$. It clearly shows the stability domains around the lower equilibrium, as well as a very regular pattern of 'lobsters'. See section 3.5 for further details and a reason for that name.

Fundamental domains

We organize our explorations by dividing the parameter plane into so-called fundamental domains, based on the stability types of the upper and lower equilibria. Fig-

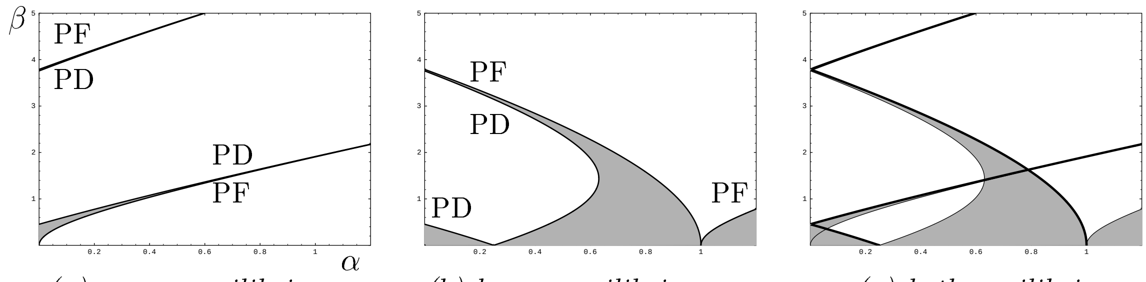

(a) upper equilibrium *(b) lower equilibrium* *(c) both equilibria*

Figure 5: Part of the (numerically computed) stability diagrams of the equilibria of the pendulum (1), first separate, then combined. Shading indicates stability. The diagrams are symmetric around the α axis. At curves labeled 'PF' or 'PD' pitchfork bifurcations or period doubling bifurcations take place, respectively. In the rightmost diagram, thickened curves correspond to boundaries of fundamental domains.

ure 5 shows the corresponding stability diagrams in the (α, β) plane, where shading indicates stability. The stability boundaries are curves of pitchfork (PF) or period doubling (PD) bifurcations, as indicated. The pitchfork bifurcation has codimension one due to the spatial symmetry of the system, see below.

Combining the two stability diagrams we see that the parameter plane consists of regions of four different types, depending on the stability types of the two equilibria. These regions are collected mostly in groups of four, one of each type, forming what will be called *fundamental domains*, again see figure 5, also compare figure 6 for a sketch of one domain. Most fundamental domains belong to four types, depending on the bifurcation type of their boundaries. Indeed, these domains have four sides, where opposite sides correspond to different bifurcation types, either pitchfork or period doubling, leading to a total of four possibilities.

The fundamental domains mostly appear in blocks of 2×2 domains, one of each type, as illustrated in figure 7. Moving across such a block, both 'horizontally' and 'vertically', one intersects two stability boundaries of PF type (where the trace of the linearized Poincaré map at the relevant equilibrium equals 2), two of PD type (where the trace is -2), and finally another one of PF type, in that order.

The stability types and bifurcations of the upper and lower equilibria are the same in fundamental domains of the same type. Since the stability islands around centers of lower period are usually the largest, the upper and lower equilibria are expected to influence the dynamics mostly. Therefore we restrict our study to a few fundamental domains near the origin of the parameter plane and farther away, and conjecture that the dynamics in other domains is similar. This conjecture is supported by the fact that the dynamics in the domains away from the origin is mainly chaotic (in the 'region of interest') and does not vary much. For the domains near the origin this is not true. Let us discuss both kinds of domains separately.

Remark 2 : Below the diagonal $\alpha = \beta$ there is a single row of fundamental domains. As noted before, the lower equilibrium is mostly stable here, and hence

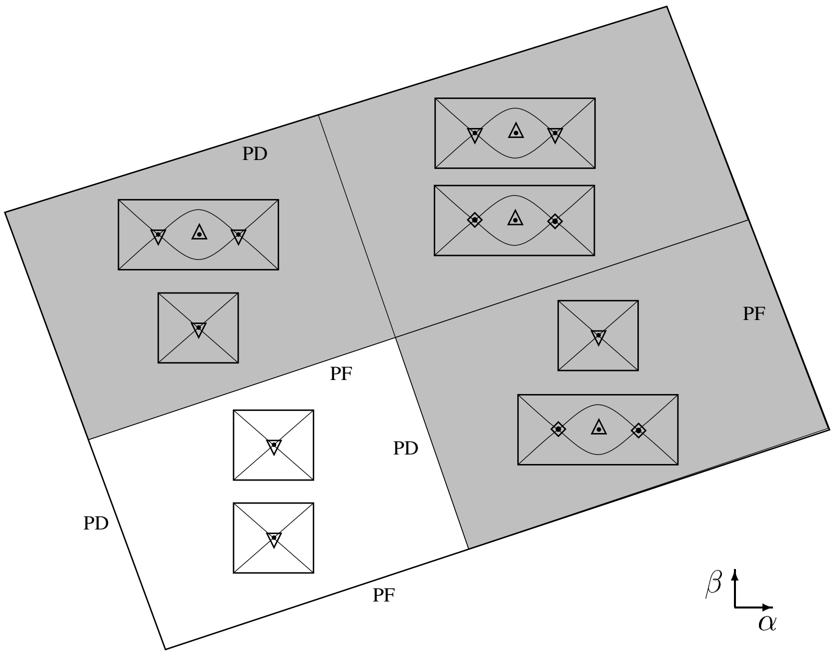

Figure 6: Sketch of one fundamental domain, with an indication of the stability types and bifurcations of the two equilibria. The bifurcations on the stability boundaries depend on the type of fundamental domain. In each region the upper equilibrium is in the top phase portrait, and the lower in the bottom one.

this region contains the largest part of the coherent, near integrable dynamics of the full problem.

Coherent dynamics near the origin of the parameter plane

The nearly integrable system for small β serves as a starting point for our study. This can be treated as a perturbation problem, in a neighborhood of any given point $(\alpha, \beta) = (\alpha_0, 0)$ on the α axis, with β and a 'detuning' parameter $\delta = \alpha - \alpha_0$ serving as perturbation parameters. It yields an integrable approximation to the Poincaré map, see [BV92, BHN98, BHNV99]. In the present paper the results of the perturbation analysis are extended to the non-integrable case by numerical continuation, where the symmetries are taken into account. We also simply compute phase portraits of P at representative parameter points.

Let us first briefly discuss the nearly integrable dynamics. In [BV92] normal forms for the integrable approximating map are given at the resonance points of the lower equilibrium $(\alpha, \beta) = (\frac{1}{4}k^2, 0)$, $k = 1, 2, \ldots$. Their local phase portraits at the lower equilibrium are reproduced in figure 8, compare [BV92, figure 8]. Up to a conjugacy the map P is an infinitely flat perturbation of the integrable approximation as the parameters go to the resonance point on the α axis and (x, y) tend to the lower equilibrium. Similar phase portraits for the degenerate point $(\alpha, \beta) = (0, 0)$ of the upper equilibrium are given in [BHN98, figures 2, 6] and [BHNV99, figures 2, 4],

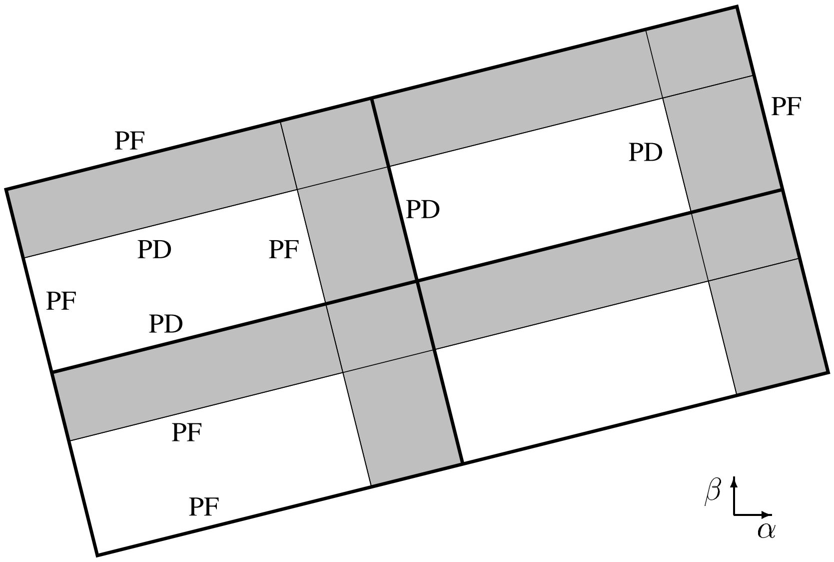

Figure 7: Sketch of one block of 2×2 fundamental domains, where the bifurcation types of the stability boundaries are indicated. As before, regions where one of the equilibria is stable are shaded, and boundaries of fundamental domains are thick.

and reproduced in figure 9. In this case the difference between P and the integrable approximation is infinitely flat as $(y, \alpha, \beta) \to (0, 0, 0)$, for all $x \in \mathbb{S}^1$.

Some features of the nearly integrable dynamics, like periodic points and their bifurcations, persist as the perturbation increases. Because of the symmetries, the periodic points of P bifurcating off at upper and lower equilibria have to move either in the x or in the y direction. Numerical continuation shows that as β increases, they either go towards the upper equilibrium, or escape from the equilibria in the y direction. As an example, figure 10 displays bifurcation diagrams of both equilibria for $\alpha = 0.079$, with β as bifurcation parameter.

We also find secondary bifurcation points on the branches bifurcating from the upper and lower equilibria, that are not found in the perturbation analysis of [BHN98, BHNV99, BV92], since this analysis only concerns a small neighborhood in phase-parameter space of a resonant or degenerate equilibrium. These bifurcations are also pitchfork or period doubling points, again see figure 10, and because of the spatio-temporal symmetry the crossing branches have to be tangent to the x- or y-axis at the bifurcation point. There is numerical evidence that they are the start of period doubling cascades, see [KH98, McL81].

More bifurcations can be found. For example, figure 3 shows large stable islands above and below the lower equilibrium, with the central fixed point undergoing a 1:3 resonance and a period doubling bifurcation. Apparently the eigenvalues of the linearized Poincaré map at the fixed point move along the complex unit circle from the saddle-center position (where both eigenvalues are 1) at $\beta = 0$ to the period doubling position (where the eigenvalues are -1) at some nonzero β, passing through

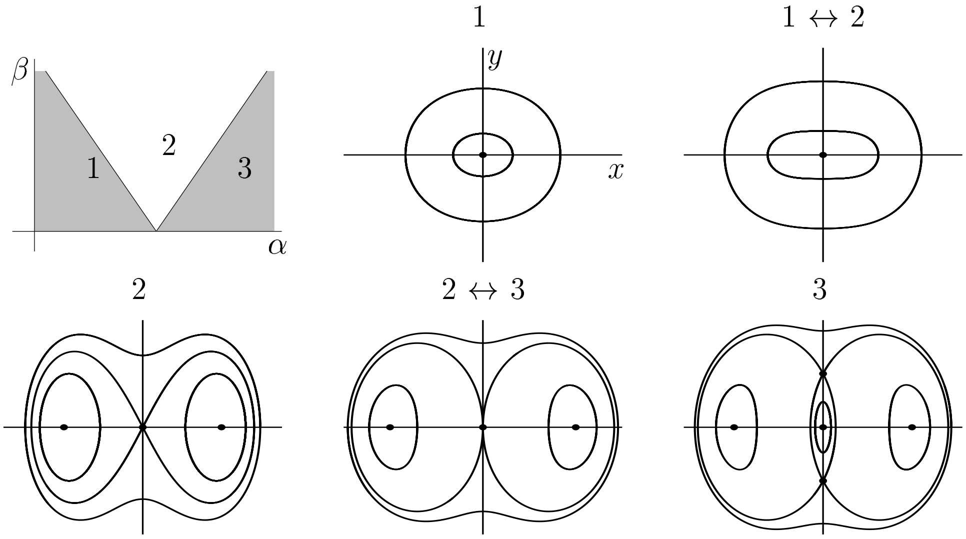

Figure 8: Stability diagram and phase portraits of an integrable approximation to P at a resonance point $(\alpha, \beta) = (\frac{1}{4}k^2, 0)$, $k \in \mathbb{Z}_{>0}$, of the lower equilibrium. The stability boundaries have k-th order of contact at the resonance point (the case $k = 1$ is displayed). The bifurcations on the boundaries are of pitchfork type if k is even, and of period doubling type otherwise, and thus generate fixed and period two points, respectively. Apart from this, in our case of spatio-temporal symmetry, the phase portraits of the integrable approximation are qualitatively the same for all k.

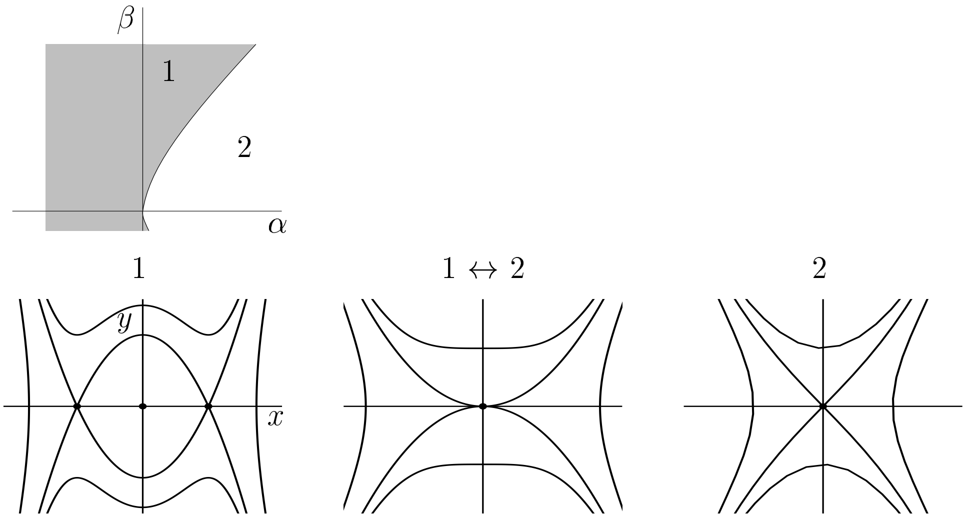

Figure 9: Stability diagram and phase portraits of an integrable approximation to P at the degenerate point $(\alpha, \beta) = (0, 0)$ of the upper equilibrium. The stability boundary consists of pitchfork bifurcations.

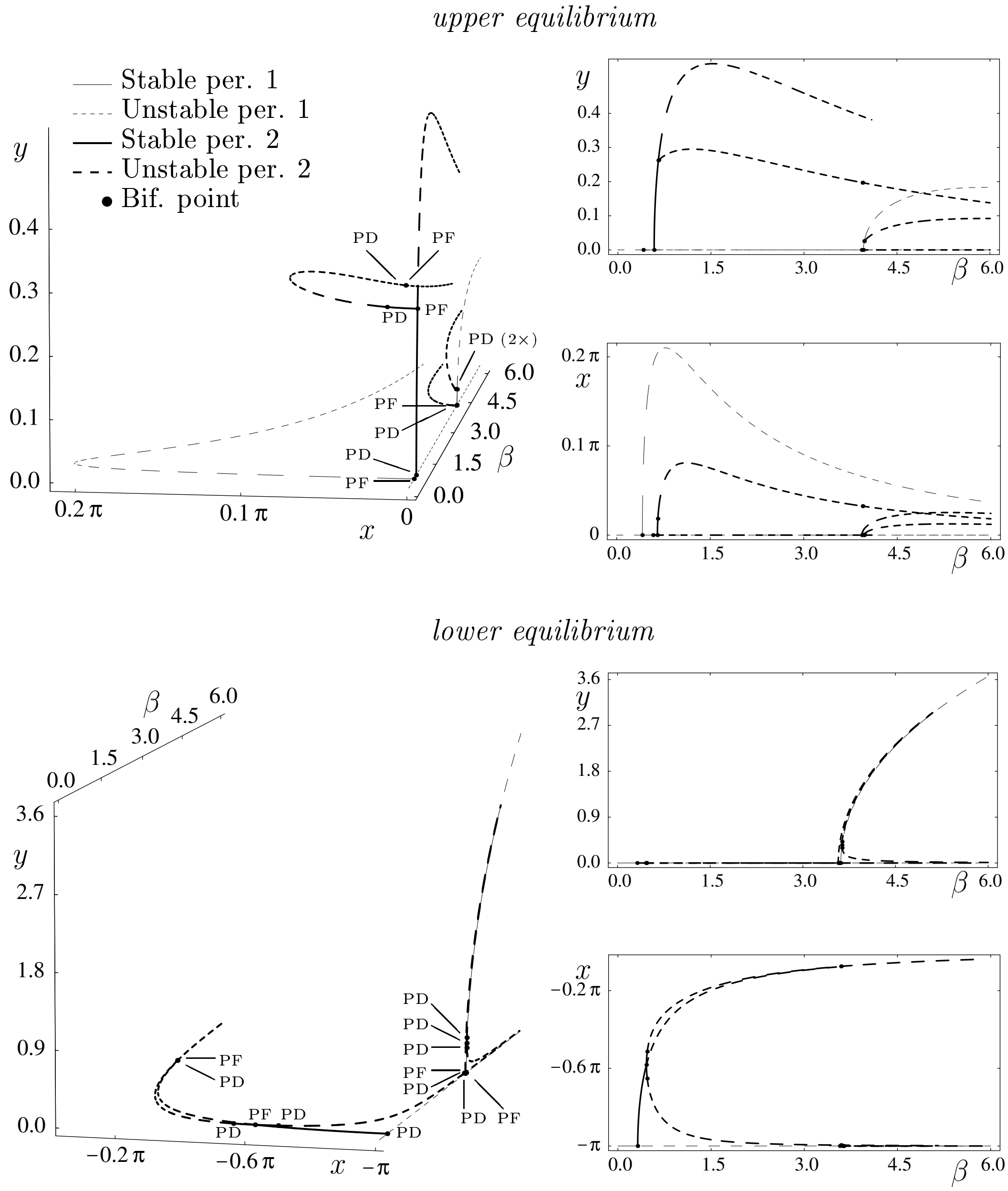

Figure 10: Bifurcation diagrams on the parameter line $\alpha = 0.079$ in (β, x, y)-space, and projected onto the (β, x)- and (β, y)-planes. They display period one and two points of P bifurcating from the upper and lower equilibria. The lines parallel to the β axis correspond to the positions of the equilibria. For simplicity only the branches in one quadrant of (β, x, y)-space are displayed, the others are their symmetric counterpart under reflection in the (β, x)- or (β, y)-plane.

all resonances $e^{\pm 2\pi i p/q}$ in between.

Coherent dynamics away from the origin of the parameter plane

As the perturbation increases, chaos seems to fill the 'region of interest' in phase space, compare figure 3. However, coherent dynamics does remain with small measure for all α, β. Moreover, the total relative measure of the set of islands is of order one as $(\alpha, \beta) \to \infty$ with $\alpha > \beta$, as shown by Neishtadt et al. [NST97], compare also [BLS] for the case $\alpha < \beta$. Above the line $\alpha = \beta$ the dynamics does not seem to vary much with the parameters in a qualitative sense.

1.3 Acknowledgments

We thank Boele Braaksma, Alan Champneys, Francesco Fassò, Àngel Jorba, Bernd Krauskopf, and Evgeny Verbitski for valuable discussion during the preparation of this paper. The research of the fourth author has been partially supported by grants BFM2000-805 (Spain), 2000SGR-27 (Catalonia) and INTAS00-221. The computer clusters (HIDRA and EIXAM) of the UB-UPC Dynamical Systems Group have been widely used.

1.4 Overview

Let us give a short overview of the remainder of this paper. In section 2 the system is introduced and some properties are discussed. We also present a codification of the fundamental domains. Section 3 applies KAM theory to show persistence of Diophantine invariant circles of P, and gives estimates on the measure of these circles and on the 'region of interest'. Appendix B discusses a numerical method for obtaining such an estimate. In section 4 the Poincaré map P is studied in several fundamental domains. The integrator used in the numerical explorations is based on Taylor series expansions, and for completeness is discussed in appendix C, see also [BS98].

2 Preliminaries

In this section some properties of the system, like symmetries, are discussed. Moreover, a codification of the fundamental domains is given.

Properties of the system

The system (1) of the parametrically forced pendulum can be written as a vector field

$$X(x, y, t; \alpha, \beta) = \frac{\partial}{\partial t} + y\frac{\partial}{\partial x} - (\alpha + \beta\rho(t))V'(x)\frac{\partial}{\partial y}, \tag{2}$$

where $y = \dot{x}$ denotes velocity as before, $(x, y, t) \in \mathbb{S}^1 \times \mathbb{R} \times \mathbb{S}^1$, $\rho(t) = \cos t$, $V(x) = \cos x - 1$, and $(\alpha, \beta) \in \mathbb{R}^2$. This vector field is Hamiltonian, with time-dependent Hamilton function

$$H(x, y, t; \alpha, \beta) = \frac{1}{2}y^2 + (\alpha + \beta\rho(t))V(x). \tag{3}$$

The vector field X has several symmetries. Since V is even, it has a spatial symmetry given by $\mathcal{S} : (x, y, t) \mapsto (-x, -y, t)$. This means that $\mathcal{S}_* X = X$, and X is called $\mathcal{S}$-equivariant. Furthermore, X is $\mathcal{R}$-reversible, meaning that $\mathcal{R}_* X = -X$, where the temporal symmetry $\mathcal{R} : (x, y, t) \mapsto (x, -y, -t)$ is due to the evenness of ρ. There are other symmetries, involving both phase and parameter space. Indeed, since $V(x) = -V(x + \pi)$, X is $\mathcal{T}$-equivariant, where $\mathcal{T} : (x, y, t; \alpha, \beta) \mapsto (x + \pi, y, t; -\alpha, -\beta)$. Finally, X is $\mathcal{U}$-equivariant, with $\mathcal{U} : (x, y, t; \alpha, \beta) \mapsto (x, y, t + \pi; \alpha, -\beta)$, because $\rho(t) = -\rho(t + \pi)$. By these two symmetries without loss of generality we can restrict to the first quadrant $\alpha, \beta \geq 0$ of the parameter plane.

Remark 3 : In [BHN98, BHNV99, BV92] more general cases of V and ρ are considered, where the symmetries $\mathcal{S}$ and $\mathcal{R}$ are optional, while $\mathcal{T}$ and $\mathcal{U}$ play no role. In the present paper we restrict to the simplest case with maximal symmetry, and take the potential function $V(x) = \cos x - 1$ of the pendulum and the forcing function $\rho(t) = \cos t$ of the classical Mathieu case.

Since the system is 2π-periodic in time, it it natural to consider its Poincaré or stroboscopic map P on the section $t = 0$, corresponding to the flow over time 2π of X. The map P is defined implicitly by

$$(P(x, y), 2\pi) = X^{2\pi}(x, y, 0),$$

where X^t is the flow over time t of X. Since X is divergence free, P is area and orientation preserving. Moreover it inherits the symmetries of X. This means that P is S-equivariant and R-reversible, that is, $SPS = P$ and $RPR = P^{-1}$, where $S : (x, y) \mapsto (-x, -y)$ and $R : (x, y) \mapsto (x, -y)$. The symmetries $\mathcal{T}$ and $\mathcal{U}$ also carry over to symmetries of P in a trivial way.

Codification of the fundamental domains

As said before, the parameter plane is divided into fundamental domains, based on the stability types of the upper and lower equilibria. These are determined by the linearized system, given by the so-called Mathieu equation

$$\ddot{x} = (\alpha + \beta\rho(t))x.$$

The Poincaré map of the Mathieu equation equals the linearization of the map P at the upper equilibrium. Thus the Mathieu equation at the parameter point (α, β) determines the stability of the upper equilibrium $(x, y, t) = (0, 0, t)$ at (α, β), and,

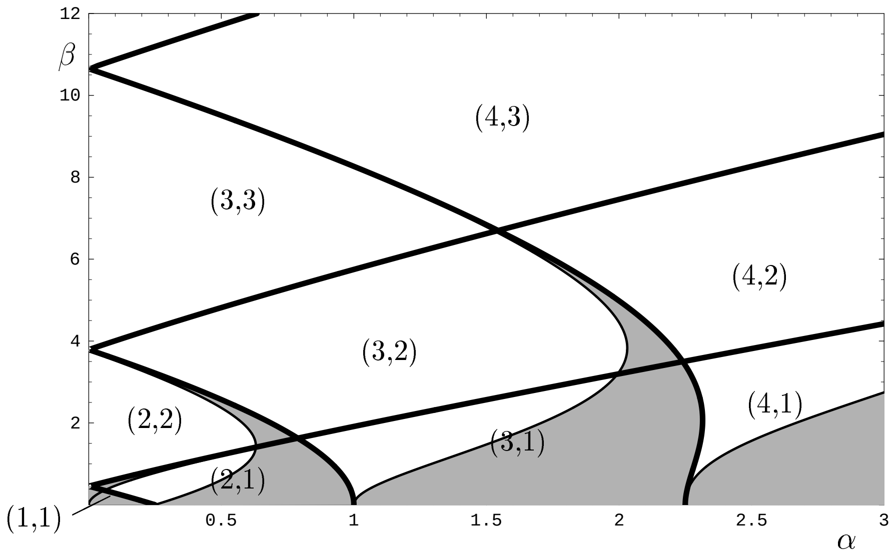

Figure 11: The stability diagram of the parametrically forced pendulum is a checkerboard of fundamental domains, that mostly consist of four stability regions. The domains are bounded by thickened (black) curves and codified as indicated. In the shaded regions the lower or upper equilibrium is stable. (In many domains these regions are too narrow to be seen.)

by the symmetry $\mathcal{T}$ of the nonlinear system, the stability of the lower equilibrium $(x, y, t) = (\pi, 0, t)$, at $(-\alpha, -\beta)$. Hence, combining the stability diagram of the Mathieu equation with a copy rotated around the origin over angle π results in a diagram where each parameter point shows the stability type of both equilibria. (Because of the symmetry $\mathcal{U}$ the copy can also be reflected in the β axis instead of rotated). This turns the parameter plane into a checkerboard, symmetric with respect to the α and β axes, see figures 1 and 5. The 'squares' of the checkerboard will be called 'fundamental domains', and mostly consist of four stability regions, as explained in section 1.2 and shown in figure 5(c).

We introduce a codification of the checkerboard. Each fundamental domain can be identified by a pair (column number, row number), starting with $(1, 1)$, as illustrated in figure 11. The stability regions in a fundamental domain can be identified by a third label equal to one of the strings 'UU', 'US', 'SU', 'SS', where the former (latter) letter determines the stability of the lower (upper) equilibrium; 'U' means unstable and 'S' stable.

Remark 4 : Some of the domains, namely those along the β axis, do not have four stability regions. We can add these fundamental domains with their symmetric counterparts (with respect to the β axis) to get squared domains. A disadvantage is that the codification of the four stability regions in such a square is different from that in squares lying entirely in the right half plane. Indeed, in the top left there is an 'SU' region (where the system has a stable lower and unstable upper equilibrium), while the top left regions of the ordinary squares are of type 'US' (i.e., with reversed stability types). Therefore we shall not use this.

3 Invariant circles and the 'region of interest'

We restrict our study of the coherent dynamics of the map P to a 'region of interest' in phase space, by excluding an infinitely large region of quasi-periodic dynamics interlaced with thin strings of islands. At any given parameter point, the 'region of interest' is bounded. In this region the fraction of integrability, that is, the relative measure of coherent dynamics, is estimated by numerical means.

It is well known from KAM theory that for y sufficiently large and satisfying a Diophantine condition, the dynamics of P is almost completely quasi-periodic, compare Moser [Mos89a, Mos89b], Chierchia and Zehnder [CZ89], and You [You90], also see Levi [Lev90, Lev91, LL91] for a similar system. In between these invariant circles of quasi-periodic motion one generically expects only strings of islands, also called Poincaré-Birkhoff chains. Indeed, the Poincaré-Birkhoff theorem [Bir13, Bir25] implies that in between any two invariant circles there exist periodic points of all intermediate rational rotation numbers. Moreover, the invariant circles form a Whitney smooth Cantor foliation of phase space that tends to full measure as $y \to +\infty$, see, e.g., Broer et al. [BHS96] and Pöschel [Pös82]. Thus the dynamics for y sufficiently large is well known, and we can restrict to a compact 'region of interest' in phase space by excluding the region of invariant circles and strings of islands, as announced in the introduction.

Remark 5 : Another well known perturbative setting appears when the integrable case $\beta = 0$ serves as unperturbed system, and persistence of Diophantine invariant circles can be shown for β sufficiently small, by a direct application of KAM theory, see Kolmogorov [Kol54], Arnol'd [Arn63], and Moser [Mos62], also compare Huang [Hua98].

Remark 6 : For sufficiently small β, one can also show persistence of Diophantine invariant circles around the lower equilibrium, by solving a similar KAM problem, but we do not pursue this particular matter any further in this paper.

We obtain the following results. At a given parameter point (α, β), invariant circles of P with Diophantine rotation number exist for $y > C(\alpha, \beta)$, for some increasing function $C > 0$. Moreover, in our real-analytic setting the relative measure of invariant circles is $1 - O(e^{-By})$ as $y \to +\infty$, for some constant $B > 0$, i.e., $y = +\infty$ is a Lebesgue density 'point' of the set of invariant circles for all parameter values.

Remark 7 : Such exponential estimates have been obtained in similar cases, see, e.g., Jorba and Villanueva [JV97] for a discussion of real-analytic Hamiltonian systems with a quasi-periodic reducible invariant torus.

Using a quantitative KAM theorem the location of the 'lowest' invariant circle of P can be estimated, thus providing a bound on the 'region of interest' for sufficiently large y at each α and β. Here 'lowest' invariant circle means an invariant circle that is a graph over x with $y > 0$ (i.e, it winds around the cylindrical phase space), and is sufficiently close to the circle $y = 0$. However, a quantitative KAM theory is rather complicated, involving normalization of a vector field given by elliptic integrals. Therefore we only indicate how such a bound can be obtained, cf. section 3.2, and refer for sharp results to future research [BNS].

The location of the 'lowest' invariant circle of P also can be estimated by numerical means. We demonstrate that, in the region $[0, 1000] \times [0, 1000]$ in the parameter plane, the 'lowest' invariant circle passes approximately through the point $(x, y) = (\pi, 2\sqrt{\alpha + \beta})$ in phase space. Thus the 'region of interest' is approximately bounded by $y = 2\sqrt{\alpha + \beta}$. This result is supported by estimates $y = 2\sqrt{\alpha}$, to first approximation as $\beta \to 0$, and $y = 2\sqrt{\alpha + \beta}$, to first approximation as $\alpha > \beta \to \infty$. These estimates are based on adiabatic theory.

In the 'region of interest' the fraction of integrability is close to 1 for $\alpha > \beta$ and close to zero for $\alpha < \beta$. In the latter region, it is correlated to jumps in the bound on the 'region of interest' for small α.

In the next subsection the vector field of the forced pendulum is rescaled and averaged using Neishtadt's theorem, rewriting it as a perturbation of an integrable system, where the perturbation size is exponentially small for large y. In subsection 3.2 we show persistence of invariant circles qualitatively, and obtain the asymptotics of the relative measure. Subsections 3.3 and 3.4 are concerned with the adiabatic and numerical estimates, respectively. Finally, section 3.5 discusses the fraction of integrability.

3.1 A well defined perturbation problem

To obtain a persistence result for large y we first need a well defined perturbation problem. For large y (compared to α and β) the motion of the forced pendulum is a small perturbation of motion on tori $y =$ constant, with frequency vector $(\dot{x}, \dot{t}) = (y, 1)$. This suggests the following translation, where ω is a localization parameter denoting the first frequency:

Lemma 8 *Let* $X = y\frac{\partial}{\partial x} + (\alpha + \beta \cos t) \sin x \frac{\partial}{\partial y} + \frac{\partial}{\partial t}$ *be the vector field of the forced pendulum. Consider the localization*

$$(x, y, t) \mapsto (\tilde{x}, \tilde{y}, \tilde{t}) = (x, y - \omega, t).$$

Then the transformed vector field is Hamiltonian, and given by

$$X(x, y, t; \alpha, \beta, \omega) = (\omega + y)\frac{\partial}{\partial x} + (\alpha + \beta \cos t) \sin x \frac{\partial}{\partial y} + \frac{\partial}{\partial t},$$

where the tildes are dropped for simplicity.

In the sequel the dependence on α and β is suppressed for simplicity. We note that the transformed vector field is $\mathcal{S}$-equivariant and $\mathcal{R}$-reversible, if the transformation $\omega \mapsto -\omega$ is included in the definition of these symmetries.

In the localized setting, y is considered to be a small variable, compared to ω. Hence, the vector field at large ω (i.e., large y in the original setting) can be seen as a small perturbation of the integrable vector field $\omega\frac{\partial}{\partial x}$. This vector field has a family of invariant tori $y = 0$, parameterized by ω. In the perturbed setting many of these still give rise to quasi-periodic dynamics, and their asymptotical relative measure can be estimated for $\omega \to +\infty$. In order to improve this estimate, we average the system such that the non-integrable part is exponentially small as $\omega \to +\infty$. Embedding the phase space $\mathbb{S}^1 \times \mathbb{R} \times \mathbb{S}^1$ in $\mathbb{C}^3$, we obtain the following theorem.

Theorem 9 *Let $D \subset \mathbb{C}^3$ be a bounded region containing the torus $y = 0$. Then there exists a neighborhood $\tilde{D}$ of D, such that for ω sufficiently large there exists an analytic, symplectic, time-preserving map $\Psi = \Psi_\omega : D \longrightarrow \tilde{D}$, piecewise analytic in ω, with*

$$\Psi - Id = O(\omega^{-1}) \text{ on } D, \text{ as } \omega \to +\infty,$$

and

$$\begin{aligned} \Psi_*^{-1} X(x, y, t; \omega) &= X_0(y, t; \omega) + X_1(x, y, t; \omega), \text{ where} \\ X_0(y, t; \omega) &= f(y, t; \omega)\frac{\partial}{\partial \varphi} + \frac{\partial}{\partial t} \text{ for some function } f, \\ X_1(x, y, t; \omega) &= O\left(e^{-B\omega}\right) \text{ as } \omega \to +\infty, \end{aligned}$$

for some constant $B > 0$.

For a proof we refer to [BNS]. It is based on averaging with respect to x, using Neishtadt's theorem for the estimates, compare, e.g., [Nei84, Ben88, Fas90, Sim94, BRS96, JV97, BR01].

3.2 Persistence and measure of invariant circles

The vector field $X_0 + X_1$ of theorem 9, regarded as a perturbation of X_0, is not in the right format to apply KAM theory. Thus we start with a lemma that takes it to a suitable form, and subsequently discuss the existence and measure of invariant circles of this system.

The unperturbed system X_0 has invariant tori $y = 0$ for each ω. We wish to show persistence of a large set of these tori under the perturbation X_1. However, the frequency of the tori in x-direction depends on t, obstructing a direct application of KAM theory. Therefore we first average X_0 with respect to t. Denote this average by $\hat{X}_0$:

$$\hat{X}_0(I; \omega) = \frac{1}{2\pi} \int_0^{2\pi} X_0(I, t; \omega) \mathrm{d}t,$$

and let $\hat{f}$ be the t-average of f. The next lemma transforms $X_0 + X_1$ to an exponentially small perturbation of $\hat{X}_0$:

Lemma 10 *There exists a smooth symplectic transformation, mapping $X_0 + X_1$ to*

$$\tilde{X}(x, y, t; \omega) = \hat{X}_0(y; \omega) + \tilde{X}_1(x, y, t; \omega),$$

where

$$\tilde{X}_1 = O\left(e^{-\tilde{B}\omega}\right) \quad \text{as } \omega \to +\infty,$$

for some constant $\tilde{B} \in (0, B)$. The transformation is given by

$$(x, y, t) \mapsto \left(x + \int^t \hat{f}(y; \omega) - f(y, t; \omega)\mathrm{d}t, y, t\right).$$

The proof of lemma 10 consists of a direct computation and is therefore omitted. For simplicity we drop the tildes from now on.

The unperturbed family $\hat{X}_0$ has invariant tori $y = 0$, with frequency vector $(\dot{x}, \dot{t}) = (\hat{f}(0; \omega), 1)$. For sufficiently large ω, $\hat{f}$ is a strictly increasing function of ω, and hence can be regarded as a new parameter, that we again call ω. For more details on this construction we refer to [BHT90, Hui88, §5a]. Thus we obtain the system

$$X(x, y, t; \omega) = X_0(\omega) + X_1(x, y, t; \omega), \tag{4}$$

with

$$X_0(\omega) = \omega\frac{\partial}{\partial x} + \frac{\partial}{\partial t}, \text{ and } X_1 = O\left(e^{-B\omega}\right).$$

The unperturbed system X_0 has invariant tori $y = 0$ with frequency vector $(\omega, 1)$. We now prove that the tori with Diophantine frequency vector persist under the perturbation X_1 if it is sufficiently small. Let the parameter ω range over an interval $\Omega = [\omega_m, \omega_M]$, with $\omega_M > \omega_m > 0$, and let

$$D = \{(x, y, t; \omega)\} = \mathbb{S}^1 \times \{0\} \times \mathbb{S}^1 \times \Omega$$

be a region in phase-parameter space that contains the invariant tori $y = 0$ of the unperturbed system. In this region the frequency ratio $\dot{x}/\dot{t}$ varies with ω, and in this sense the system is non-degenerate.

For $\sigma, \eta > 0$, let $D_{\sigma,\eta}$ be a complex neighborhood of D, given by

$$D_{\sigma,\eta} = (\mathbb{S}^1 + \eta) \times B(0, \sigma) \times (\mathbb{S}^1 + \eta) \times (\Omega + \sigma),$$

where $B(0, \sigma)$ is the closed ball in $\mathbb{C}$ with center 0 and radius σ, and, for any set $S \subset \mathbb{C}^n$ and any $\eta > 0$,

$$S + \eta = \bigcup_{w \in S} \{z \in \mathbb{C}^n : |z - w| < \eta\}.$$

Furthermore, define the set Ω^γ of Diophantine frequencies in Ω by

$$\Omega^\gamma = \{\omega \in \Omega : |p\omega + q| \geq \gamma |(p, q)|^{-\tau} \text{ for all } (p, q) \in \mathbb{Z}^2 \setminus \{0\}\}. \tag{5}$$

Here $\gamma > 0$ is a parameter and $\tau > 1$ is a constant. The dependence of Ω^γ on τ is suppressed in the notation.

A KAM theorem in the context of divergence free vector fields with codimension 1 invariant tori, cf. [Mos67, BHT90], shows the following: for ω_m sufficiently large, all invariant 2-tori of X_0 in D with frequency ω in Ω^γ and not too near the boundary of Ω, correspond to invariant 2-tori of the perturbed system X with the same frequency ratio ω. The perturbed invariant tori lie in a neighborhood of D in $\{(x, y, t; \omega)\} = \mathbb{S}^1 \times \mathbb{R} \times \mathbb{S}^1 \times \Omega$. The tori of X and X_0 are equivalent by a Whitney-smooth time-preserving diffeomorphism Ψ, depending on the parameters, that approximately maps D into D. The diffeomorphism Ψ is the identity in the t component, see [BHT90, Hui88, §7f].

The largeness condition on ω_m amounts to the following. By KAM theory there exists a $\delta > 0$, depending only on η (so in particular independent of γ, τ, σ, and Ω), such that all tori $y = 0$ of the unperturbed system X_0 with frequency ω in Ω^γ persist under the perturbation X_1 if

$$|X_1|_{\sigma,\eta} := \sup_{D_{\sigma,\eta}} ||X_1|| < \gamma\delta, \text{ and } 0 < \gamma \leq \sigma < 1, \tag{6}$$

see, e.g., [BHS96, §5.2]. Since $|X_1|_{\sigma,\eta} = O(e^{-B(\omega_m+\sigma)})$, this condition is obviously satisfied for $\gamma = \sigma = O(e^{-\tilde{B}\omega_m})$ for some $\tilde{B} \in (0, B)$, and $\omega_m > 0$ sufficiently large.

Remark 11 : In the usual KAM setting, persistence of a torus also requires the frequency vector to be non-degenerate, compare, e.g., [Kol54, Kol57, Arn88, Arn89]. One then finds a *conjugacy* between the tori of the perturbed and unperturbed systems. In our case, the frequency vector of X_0 has a constant component and is therefore degenerate in this strict sense. However, this non-degeneracy condition can be relaxed to the requirement that the frequency *ratio* is non-degenerate, i.e., varies with ω, see, e.g., [Mos67, BHT90]. In this setting the perturbed and unperturbed tori are just *equivalent* in general.

Remark 12 : An alternative way to show persistence of invariant tori is a direct construction by Poincaré-Lindstedt perturbation series (instead of constructing a conjugacy or equivalence), cf., e.g., Celletti and Chierchia [CC88a, CC88b], Greene and Percival [GP81], and Jorba et al. [JdlLZ99, JM99].

Remark 13 : The persistence result can also be obtained for the return map P of X on the section $t = 0$. In the localized setting of equation 4, it is a perturbation of the return map P_0 of X_0, given by

$$P_0 : (x, y) \mapsto (x + 2\pi\omega, y).$$

This is a pure twist map, having invariant circles $y = 0$ with rotation number ω, corresponding to the invariant 2-tori $y = 0$ of X_0, and we have to check persistence of these circles.

One now considers a region $\tilde{D} = \{(x, y; \omega)\} = \mathbb{S}^1 \times \{0\} \times \Omega$ in the phase space of P, that is completely foliated by invariant circles of P_0. Since P is area preserving, the twist theorem, cf. [Mos62], is applicable, and shows that for ω sufficiently large, the invariant circles of P_0 in $\tilde{D}$ with Diophantine rotation number (except those with ω near the boundary of Ω) are conjugate to invariant circles of P with the same rotation number. The perturbed invariant circles lie in a neighborhood of $\tilde{D}$. The rotation number is exactly equal to the frequency ratio of the vector field, and the Diophantine condition on ω is the same as in the previous case. The conjugacy between the invariant circles of P_0 and P is given by the same diffeomorphism Ψ, restricted to the section $t = 0$ where P is defined.

It remains to derive the asymptotics of the relative measure of invariant tori of X as $\omega_m \to +\infty$. Under condition 6, the relative measure of frequencies in Ω corresponding to persistent tori satisfies

$$\mu_{\mathrm{rel}}(\Omega) := \frac{\mu(\Omega^\gamma)}{\mu(\Omega)} = 1 - O\left(\frac{\gamma}{\omega_M - \omega_m}\right) \text{ as } \frac{\gamma}{\omega_M - \omega_m} \to 0,$$

cf. [BHS96, §5.2]. Taking $\gamma = O(e^{-\tilde{B}\omega_m})$, we obtain the following theorem.

Theorem 14 *Let X be the vector field of the forced pendulum in the form given by equation (4), and let $\Omega = [\omega_m, \omega_M]$. an interval of frequencies. Choose constants $\tau > 2$ and $\eta > 0$. For ω_m sufficiently large, take $\gamma = O(e^{-\tilde{B}\omega_m})$ such that condition (6) is satisfied, and let Ω^γ be the set of Diophantine frequencies in Ω, defined by (5). Then then relative measure of persistent tori in Ω, defined as above, satisfies*

$$\mu_{rel}(\Omega) = 1 - O\left(\frac{e^{-\tilde{B}\omega_m}}{\omega_M - \omega_m}\right) \text{ as } \omega_m \to +\infty, \text{ with } \omega_M > \omega_m.$$

This proves that the torus with frequency vector $(+\infty, 1)$ is a Lebesgue density point of the set of persistent tori. For the original system (2) this means the following: for large ω, one has $y \approx \omega$, where y is the phase variable in the original setting. Thus the invariant torus $y = +\infty$ of the original system is a Lebesgue density point of the set of invariant tori, and the relative measure is $1 - O(e^{-By})$ as $y \to +\infty$, for some constant $B > 0$.

To obtain a quantitative result on the persistence of invariant tori, condition (6) has to be evaluated explicitly. This involves estimates on the perturbation X_1 and on δ. The first requires an improvement of theorem 9, with estimates on X_0, X_1 and $\Psi - \mathrm{Id}$ in appropriate norms. For the latter one can use, for example, the explicit expression obtained by Delshams and Gutiérrez [DG96]. For other quantitative KAM theorems, designed mostly for specific systems, see, e.g., [Ben88, CC91, CFP87, CGL00, Loc99]. We plan to report on this in more detail in future research, cf. [BNS].

3.3 Adiabatic estimates of the 'region of interest'

Adiabatic estimates for the size of the 'region of interest' are obtained in two regions in the parameter plane: for β small compared to α, and for large (α, β), 'near infinity', with $\alpha > \beta$. In these regions the adiabatic estimates are

$$y = 2\sqrt{\alpha},$$

to first approximation as $\beta \to 0$, and

$$y = 2\sqrt{\alpha + \beta},$$

to first approximation as $\alpha > \beta \to +\infty$, respectively. We first discuss the estimate for small β/α.

The stability diagram of figure 1 shows that the upper equilibrium is unstable if $\alpha > \beta \geq 0$, also see [PS28, MS54]. For $\alpha > 0$ and β small compared to α, the 'region of interest' is approximately bounded by the invariant manifolds of the unstable upper equilibrium of P. Indeed, for $\beta = 0$ the system is integrable, and the separatrices of the upper equilibrium exactly bound the 'region of interest', while outside this region only invariant circles exist. Thus by KAM theory the map P has invariant circles arbitrarily close to the invariant manifolds of the upper equilibrium, if $\beta > 0$ is sufficiently small. Neishtadt's theorem [Nei84] implies that these manifolds lie in a neighborhood of the separatrices of the integrable system that vanishes as $\beta \to 0$. This proves the following lemma.

Lemma 15 *For $\alpha > 0$ the maximal y coordinate of the invariant manifolds of the unstable upper equilibrium satisfies*

$$y(\alpha, \beta) = 2\sqrt{\alpha} + f(\alpha, \beta),$$

where the remainder $f(\alpha, \beta)$ vanishes as $\beta \to 0$. The 'region of interest' is bounded by

$$y(\alpha, \beta) = 2\sqrt{\alpha},$$

to first approximation, as $\beta \to 0$.

To obtain an estimate for $\alpha, \beta \to +\infty$, with $\alpha > \beta$, we rescale to a slowly varying system by the following lemma:

Lemma 16 (rescaling) *Let $X = y\frac{\partial}{\partial x} + (\alpha + \beta \cos t) \sin x \frac{\partial}{\partial y} + \frac{\partial}{\partial t}$ be the vector field of the forced pendulum. Consider the rescaling*

$$(x, y, t; \alpha, \beta) \mapsto (\tilde{x}, \tilde{y}, \tilde{t}; \tilde{\alpha}, \tilde{\beta}, \varepsilon) = (x, \varepsilon y, t, \varepsilon^2 \alpha, \varepsilon^2 \beta) \ , \ X \mapsto \tilde{X} = \varepsilon X,$$

where $\varepsilon = (\alpha + \beta)^{-1/2}$. Then the rescaled vector field is Hamiltonian, $\mathcal{S}$-equivariant and $\mathcal{R}$-reversible, and is given by

$$X(x, y, t; \alpha, \beta, \varepsilon) = y\frac{\partial}{\partial x} + (\alpha + \beta \cos t) \sin x \frac{\partial}{\partial y} + \varepsilon \frac{\partial}{\partial t},$$

where the tildes are dropped for simplicity.

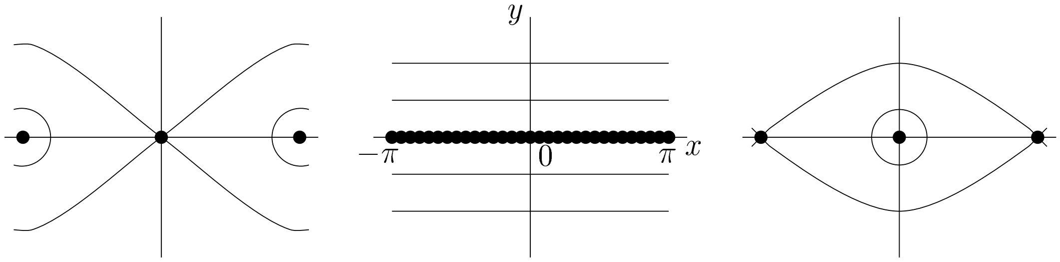

Figure 12: Sketch of the phase portrait of the unperturbed, frozen system $X_{|\varepsilon=0}$. If $\alpha+\beta\cos t>0$, then the upper equilibrium is unstable and the lower is stable. If $\alpha+\beta\cos t<0$ (can only occur if $\beta>\alpha$), the stability types are reversed. If $\alpha+\beta\cos t=0$ (only possible if $\beta\geq\alpha$), then the system is highly degenerate: all points on the x axis are in equilibrium.

The proof is a straightforward computation, and is therefore omitted. The new parameters α, β satisfy $\alpha+\beta=1$. The rescaled vector field X can be seen as a perturbation of the integrable, frozen vector field

$$X(x,y,t;\alpha,\beta,0)=y\frac{\partial}{\partial x}+(\alpha+\beta\cos t)\sin x\frac{\partial}{\partial y}.$$

In the original setting the frozen system is located at unbounded (y,α,β). The dynamics of the frozen system in the (x,y)-cylinder depends on the value of the 'parameter' t, see figure 12, while its integral curves coincide with the level sets of the Hamiltonian.

The region above the frozen separatrix is filled with invariant circles of the frozen system, and adiabatic theory can be applied to get an estimate on the 'lowest' invariant circle of the slowly varying system. Since $\alpha>\beta$, the unperturbed system has an unstable upper and a stable lower equilibrium, compare figure 12, and hence its lowest invariant circle is arbitrarily close to the separatrix

$$y=\sqrt{2(\alpha+\beta\cos t)(1-\cos x)}.$$

By adiabatic theory, an orbit of the perturbed system remains $O(\varepsilon)$ close to the frozen orbit with the same initial condition for infinite time, if it does not intersect the frozen separatrix, see, e.g., [Arn62, Arn88, EE91, NST97]. The 'lowest' frozen orbit that does not remain above the separatrix lies on the manifold

$$y=\sqrt{2(\alpha+\beta)(1-\cos x)}.$$

Thus the maximal y-coordinate of the invariant manifolds of the upper equilibrium of the perturbed system is given by

$$y=2\sqrt{\alpha+\beta}+\varepsilon\tilde{g}(\alpha,\beta,\varepsilon),$$

for some function $\tilde{g}$. Rescaling back to the original phase variables and parameters, and applying KAM theory, we arrive at the following lemma:

Lemma 17 *In the original coordinates, for $\alpha > \beta$ the maximal y coordinate of the invariant manifolds of the unstable upper equilibrium satisfies*

$$y(\alpha, \beta) = 2\sqrt{\alpha + \beta} + g(\alpha, \beta),$$

where $g(\alpha, \beta)$ is small compared to $\sqrt{\alpha+\beta}$ as $\alpha, \beta \to +\infty$. To first approximation as $\alpha, \beta \to +\infty$, the 'region of interest' is bounded by

$$y(\alpha, \beta) = 2\sqrt{\alpha + \beta}.$$

3.4 Numerical estimates of the 'region of interest'

We estimate numerically the size of the 'region of interest', by computing the location of the 'lowest' invariant circle of P on three evenly spaced grids in the parameter plane, namely in the regions $\{(\alpha, \beta)\} = [0, 10] \times [0, 10]$ with step 0.05 in both variables, $\{(\alpha, \beta)\} = [0, 100] \times [0, 100]$ with step 0.5, and $\{(\alpha, \beta)\} = [0, 1000] \times [0, 1000]$ with step 10. By location we mean the y-coordinate y_π of the invariant circle at $x = \pi$. This is a good estimate for the maximal y coordinate on this circle. Indeed, numerical experiments suggest that y_π is a local maximum on the invariant circle, except in a small neighborhood of $(\alpha, \beta) = (0, 0.22)$. Moreover, the only other reasonable candidate (regarding the numerical experiments of section 4) for a global maximum is the y value y_0 at $x = 0$, and numerical results in a large region in the parameter plane show that $y_\pi > y_0$ except in a small domain near the origin. Indeed, we find that $y_0 < 2$ for $(\alpha, \beta) \in [0, 1000] \times [0, 1000]$, see figure 13. The lower boundary is given by $\alpha = \frac{1}{2}\beta^3 + O(\beta^4)$, as illustrated in the figure. This is confirmed by a normal form computation. For details we refer to appendix A.

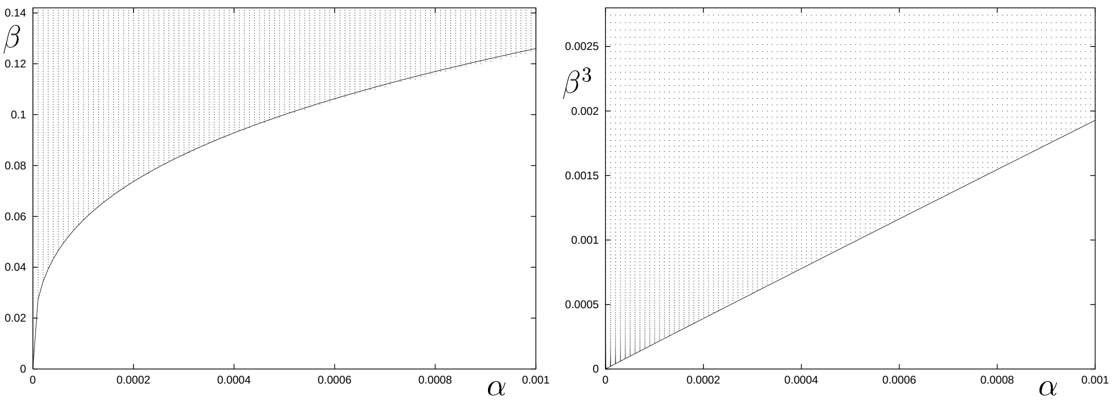

Figure 13: Left: region in the parameter plane where the y-coordinate y_0 of the 'lowest' invariant circle at $x = 0$ is larger than its y-coordinate y_π at $x = \pi$. The curve $\alpha = \frac{1}{2}\beta^3$, that approximates the lower boundary of the region, is also drawn. Right: the same region, in the (α, β^3)-plane, showing an even better approximation to the lower boundary, namely $\alpha = \frac{1}{2}\beta^3 - 0.15\beta^4$.

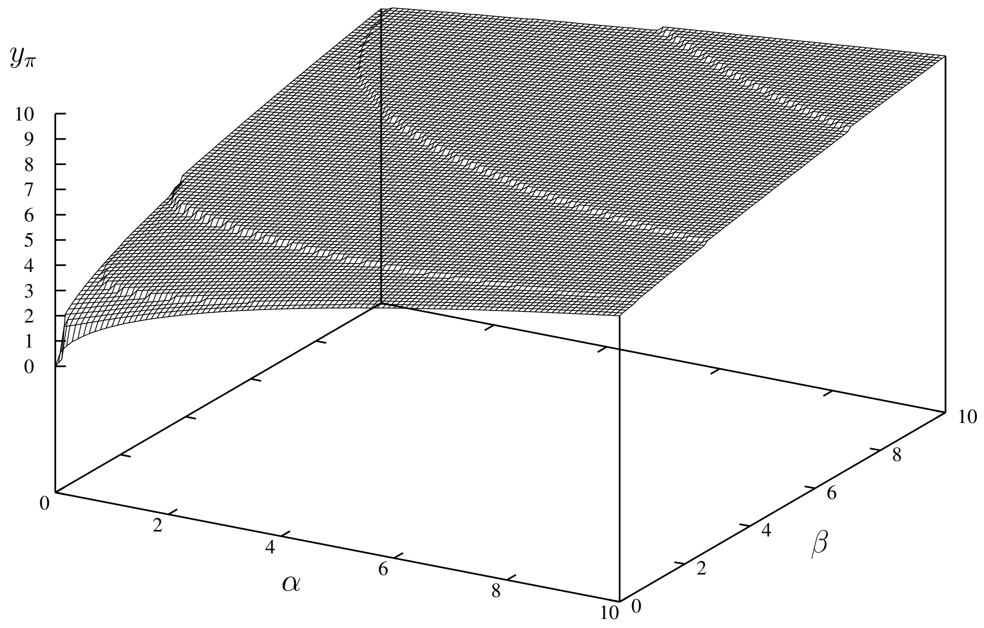

Figure 14: Graph over $(\alpha, \beta) \in [0, 10] \times [0, 10]$ of the location of the 'lowest' invariant circle of P, i.e., its intersection with $x = \pi$.

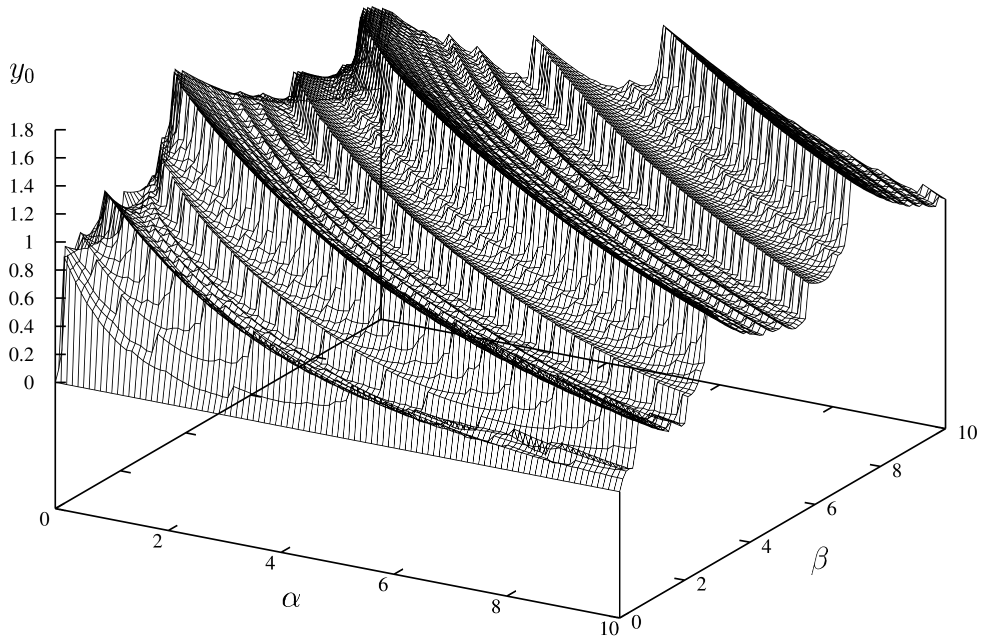

Figure 15: Graph over $(\alpha, \beta) \in [0, 10] \times [0, 10]$ of the intersection of the 'lowest' invariant circle of P with $x = 0$.

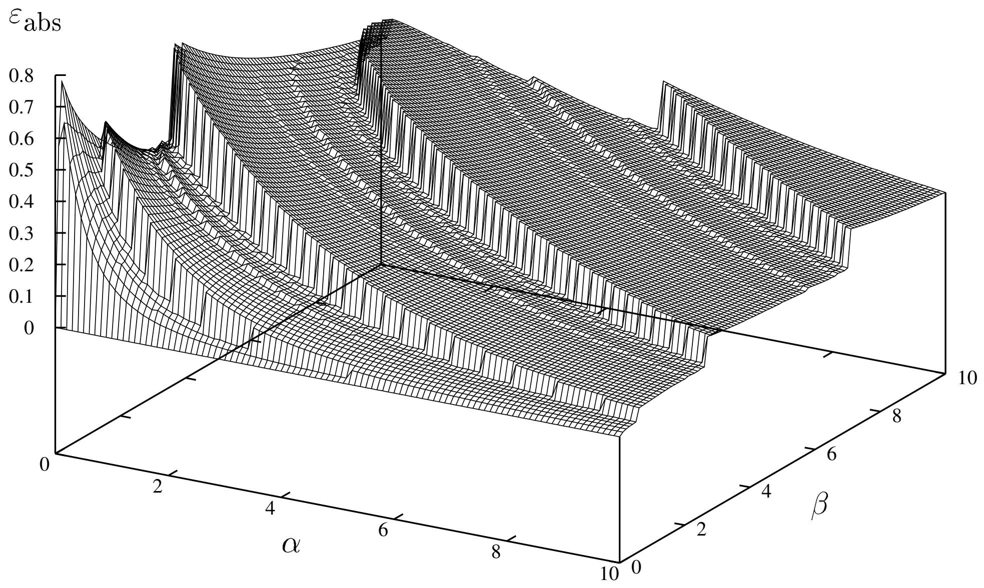

Figure 16: Absolute difference $\varepsilon_{\rm abs} = |y_\pi - y_{\rm adiab}|$ between the numerical and adiabatic estimates of the location of the 'lowest' invariant circle, on the domain $\{(\alpha, \beta)\} = [0, 10] \times [0, 10]$.

For a description of the method of computation of the location of the lowest invariant circle we refer to appendix B, also compare [STa]. Figure 14 shows this location in the region $[0, 10] \times [0, 10]$ in the parameter plane. The graph of y_0 is displayed in figure 15. The latter graph turns out to lie below the plane $y = 2$ (this is also true for the larger grids), while the adiabatic estimates, see section 3.3, suggest that the former is close to $y = y_{\text{adiab}} \equiv 2\sqrt{\alpha+\beta}$. The corresponding absolute difference $\varepsilon_{\text{abs}} = |y_\pi - y_{\text{adiab}}|$ is displayed in figure 16.

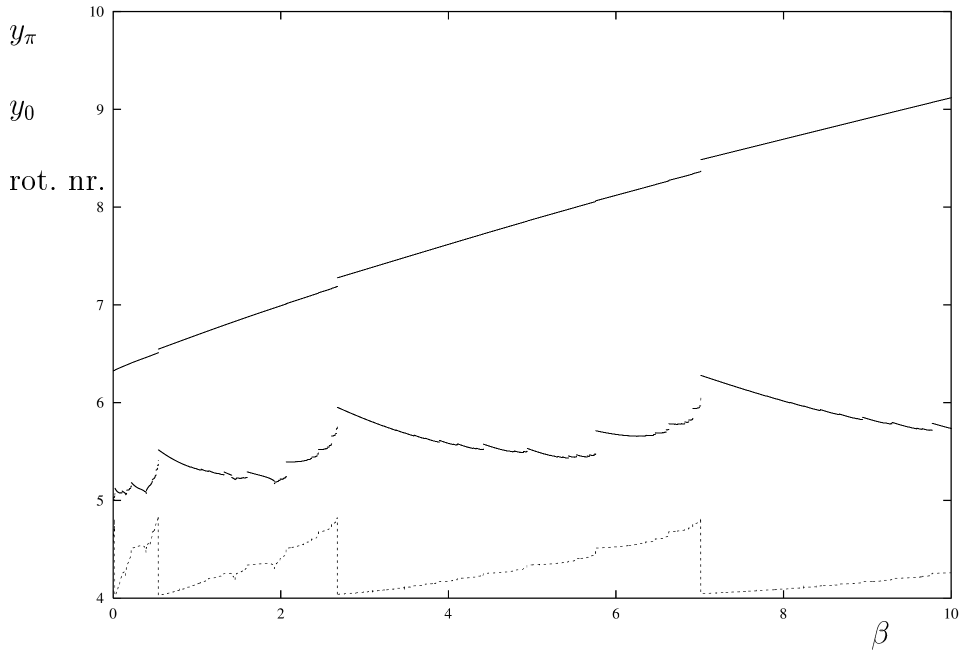

Figure 17: Graphs over $\beta \in [0, 10]$ of the intersection of the 'lowest' invariant circle with $x = \pi$ (upper graph) and $x = 0$ (middle), and its rotation number (lower), all for fixed $\alpha = 10$. To show all graphs conveniently in one plot, the latter two are translated vertically over 5 and 4, respectively.

In the three figures 14 – 16 one clearly sees jumps in the location of the 'lowest' invariant circle. These are due to destruction of the 'lowest' invariant circle as β grows, resulting in a jump in the estimate to a higher invariant circle. This can be seen very well in figure 17, where the intersections of the 'lowest' invariant circle with the lines $x = 0$ and $x = \pi$, as well as its rotation number, are displayed as graphs over $\beta \in [0, 10]$, while $\alpha = 10$ is fixed. This results in a 'devils staircase', where the largest discontinuities in the graphs correspond to jumps of the 'lowest' invariant circle over an island of low period. Figure 18 shows the rotation number of the 'lowest' invariant circle as a graph over (α, β). In both figures we observe steep cliffs where the rotation number jumps from a value near 1 to a value near 0, corresponding to jumps of the 'lowest' invariant circle over large stable domains.

The jumps of the 'lowest' invariant circle occur on curves in the parameter plane, that are indicated in figure 19. In fact, we plot in this figure the points where the

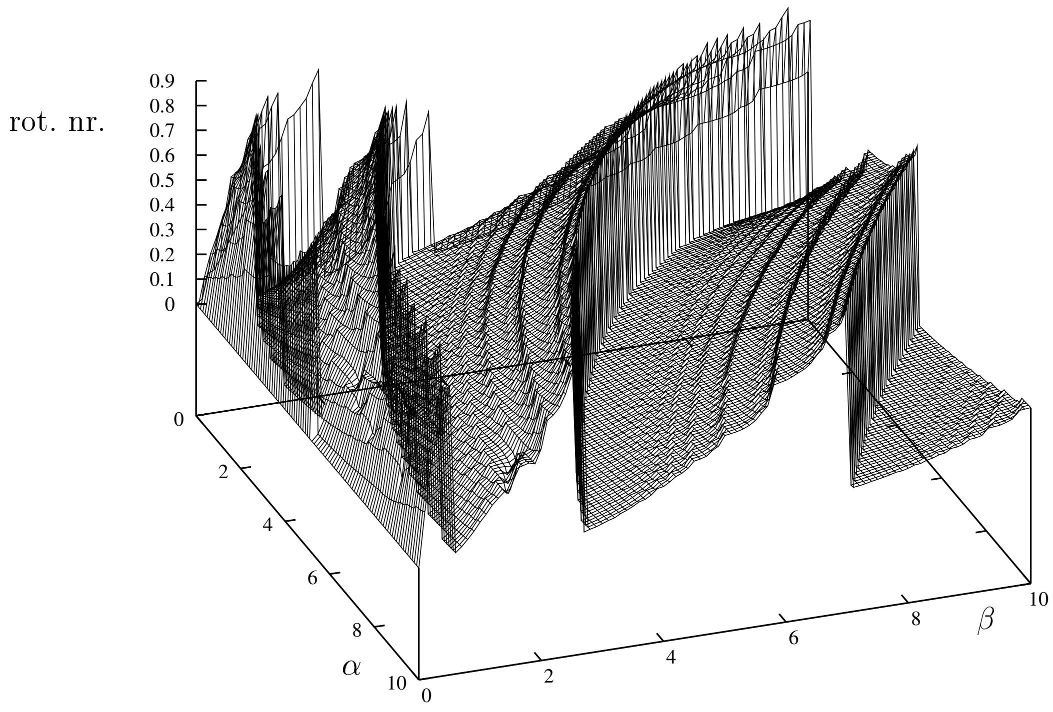

Figure 18: Graph over $(\alpha, \beta) \in [0, 10] \times [0, 10]$ of the rotation number of the 'lowest' invariant circle. The cliffs correspond to the jumps in the location of this circle.

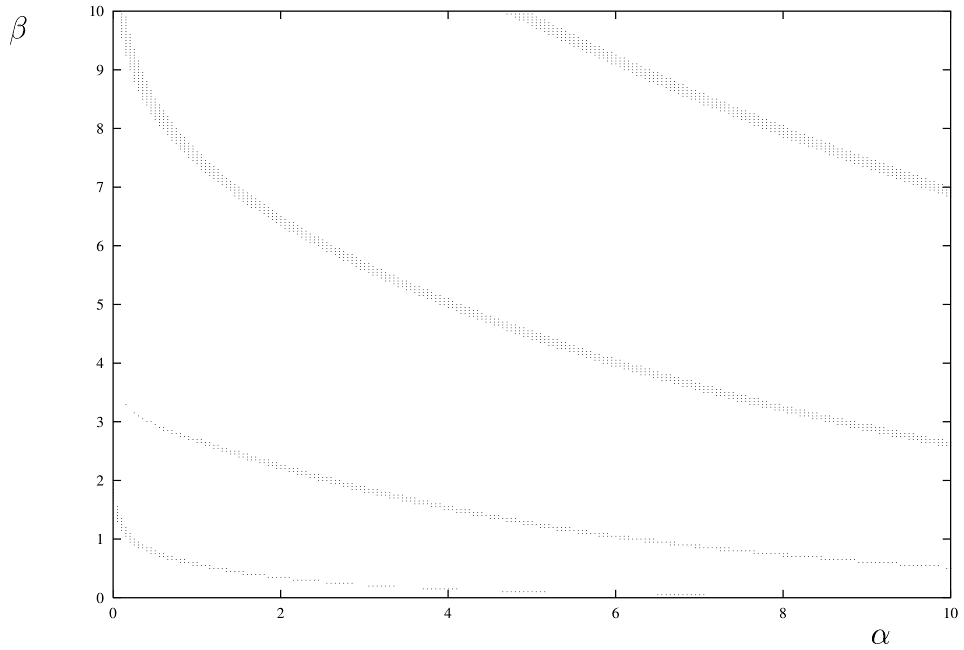

Figure 19: Location of the cliffs in figure 18. Actually we plot the points where the rotation number is larger than 0.7.

rotation number is close to 1 (in this case, larger than 0.7), i.e., the points where the largest jumps take place.

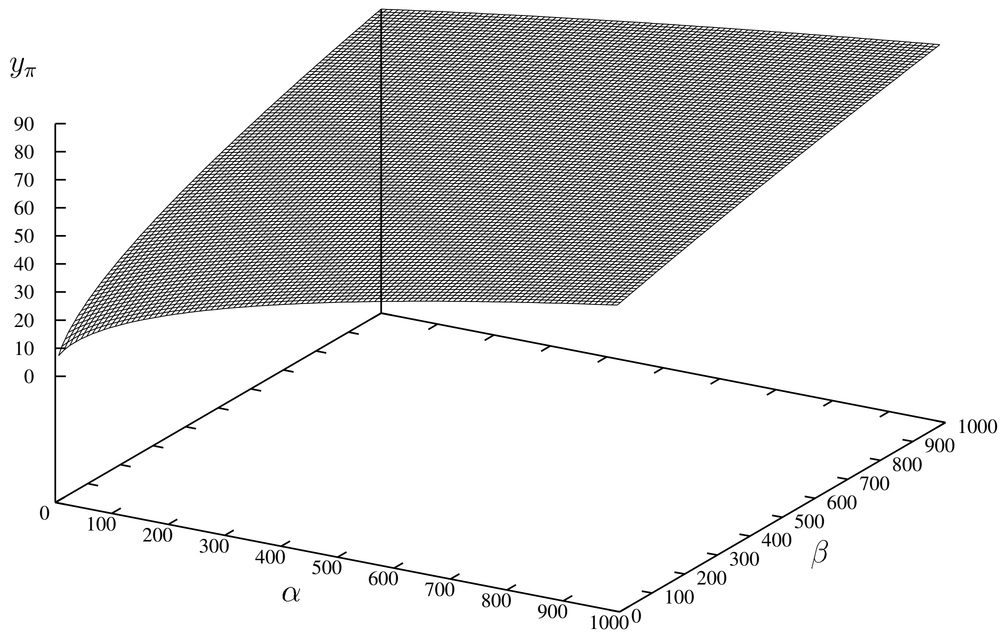

Figure 20: Graph over $(\alpha, \beta) \in [0, 1000] \times [0, 1000]$ of the location of the 'lowest' invariant circle of P.

Figures 20 and 21 show the location of the 'lowest' invariant circle and the absolute difference ε_{abs} on the large grid $\{(\alpha, \beta)\} = [0, 1000] \times [0, 1000]$. Again we can see the location of the jumps, and it is clear that the relative difference decreases as α and β increase.

grid	ε_{abs}	ε_{rel}	$\varepsilon_{\text{rel}}(5)$	$\varepsilon_{\text{rel}}(50)$	$\varepsilon_{\text{rel}}(500)$
10×10	0.77	0.92	0.11	-	-
100×100	0.67	0.32	0.10	0.021	-
1000×1000	0.35	0.049	0.049	0.014	0.0026

Table 1: The maximal relative difference ε_{rel} between the numerical and adiabatic estimates of the location of the 'lowest' invariant circle, in all three grids. Further, $\varepsilon_{\text{rel}}(k)$ is the same difference restricted to the region $||(\alpha, \beta)|| > k$ of the grid.

Table 1 presents for the three grids the maximal absolute and relative differences ε_{abs} and ε_{rel} between the numerical and adiabatic estimates. By relative difference we mean the absolute difference divided by the maximum of y_π and y_{adiab}. In formula:

$$\varepsilon_{\text{rel}} = \left| \frac{y_\pi - y_{\text{adiab}}}{\max(|y_\pi|, |y_{\text{adiab}}|)} \right| .$$

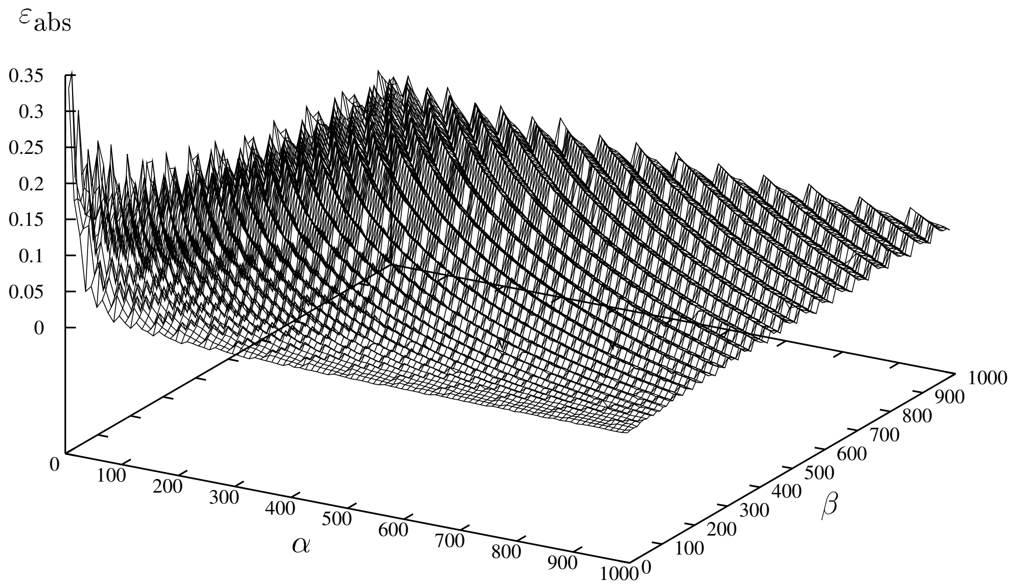

Figure 21: Absolute difference $\varepsilon_{\text{abs}} = |y_\pi - y_{\text{adiab}}|$ between the numerical and adiabatic estimates of the location of the 'lowest' invariant circle, on the domain $\{(\alpha, \beta)\} = [0, 1000] \times [0, 1000]$.

The relative difference decreases rapidly when α, β increase, compare figure 16. To illustrate this, the table also states, for several k, the maximal relative difference $\varepsilon_{\text{rel}}(k)$ in the part of the grid where $||(\alpha, \beta)|| > k$.

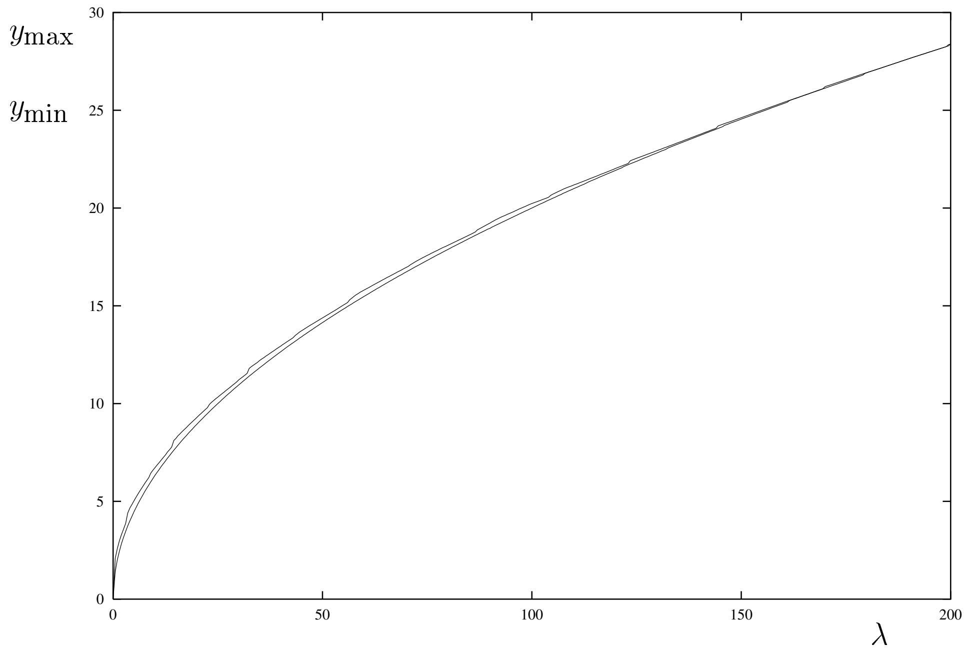

Figure 22: Graph over $\lambda \in [0, 200]$ of the maximal and minimal values of the location of the 'lowest' invariant circle in grid points on the line $\lambda = \alpha + \beta$.

The adiabatic estimate y_{adiab} is constant on lines of constant $\alpha + \beta$. For the region $[0, 100] \times [0, 100]$ in the parameter plane, figure 22 shows the maximal and minimal values $y_{\max}$ and $y_{\min}$ of the numerical estimate in grid points on lines $\alpha + \beta =$ constant, plotted against $\alpha + \beta$. In formula:

$$y_{\max}(\lambda) = \max_{\alpha,\beta} \left(y_\pi(\alpha, \beta) \right),$$

where the maximum is taken over all (α, β) in the grid with $\alpha + \beta = \lambda$, and $y_{\min}$ is defined analogously. As $\alpha + \beta$ increases the two graphs seem to converge, which again suggests that for large α, β the adiabatic estimate y_{adiab} is very accurate.

3.5 The fraction of integrability

To get a better global understanding of the dynamics in the 'region of interest' we estimate the fraction of integrability f in this region, as a function of the parameters (α, β). We define the fraction of integrability to be the relative measure of coherent dynamics in the 'region of interest', and estimate it numerically. For details and a discussion of the method of computation, cf. [Sim01].

Figure 23 shows the fraction of integrability in the domain $[0, 100] \times [0, 100]$ in the parameter plane. For a better view, a logarithmic scale is used. A contour plot

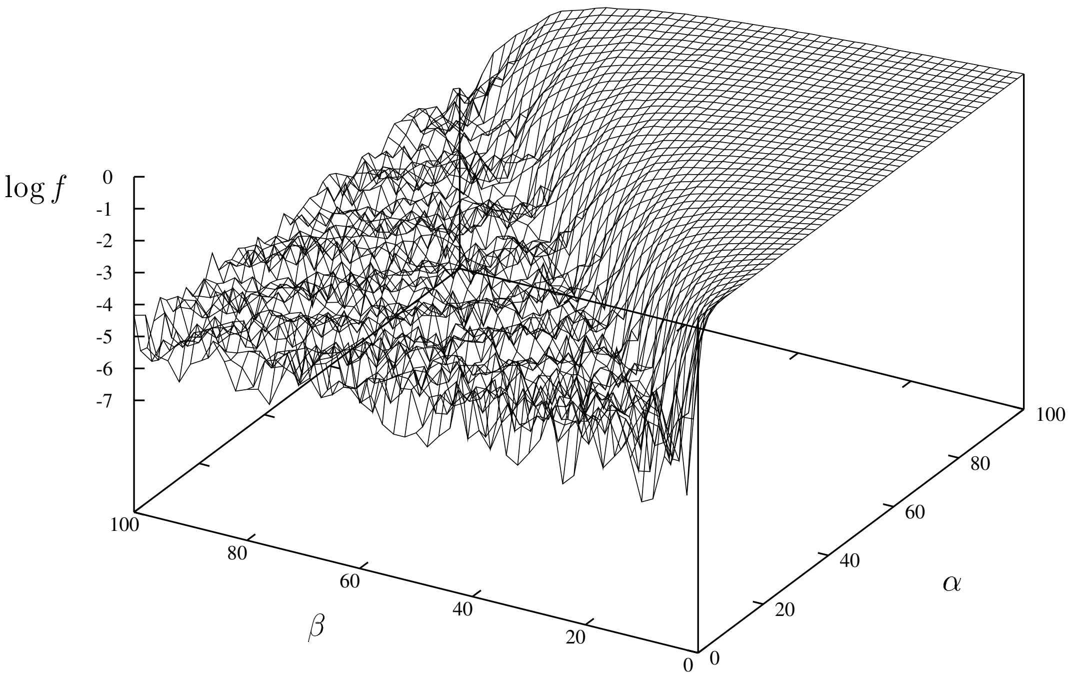

Figure 23: Graph over $(\alpha,\beta) \in [0,100] \times [0,100]$ of $\log f$, the logarithm of the fraction of integrability.

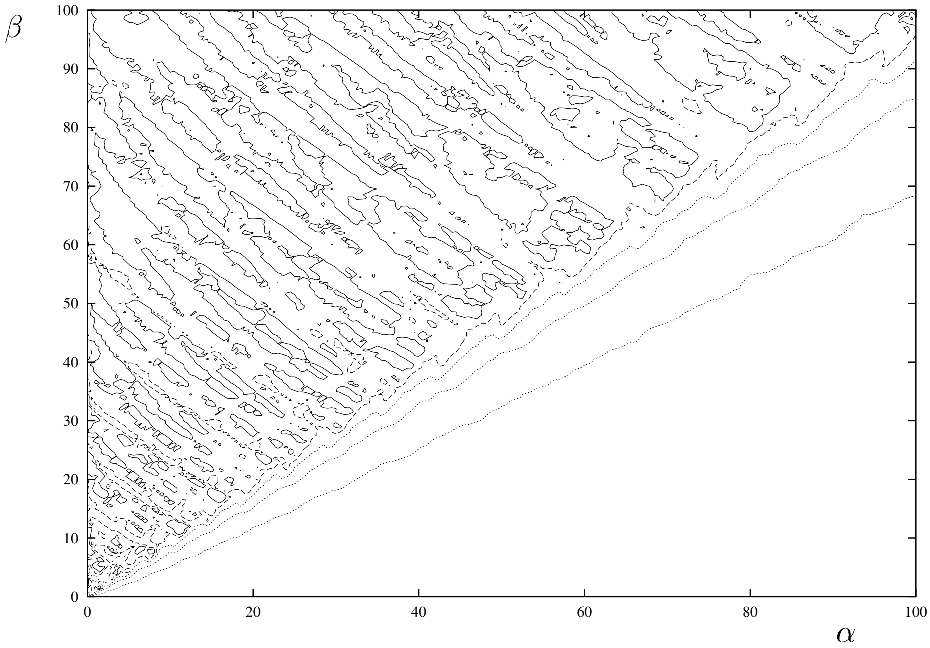

Figure 24: Contour plot of $\log f$, in the domain $\{(\alpha,\beta)\} = [0,100] \times [0,100]$. On the solid curves $\log f = -5$, on the dashed curves it is -4 and on the dotted curves it equals -3, -2 or -1.

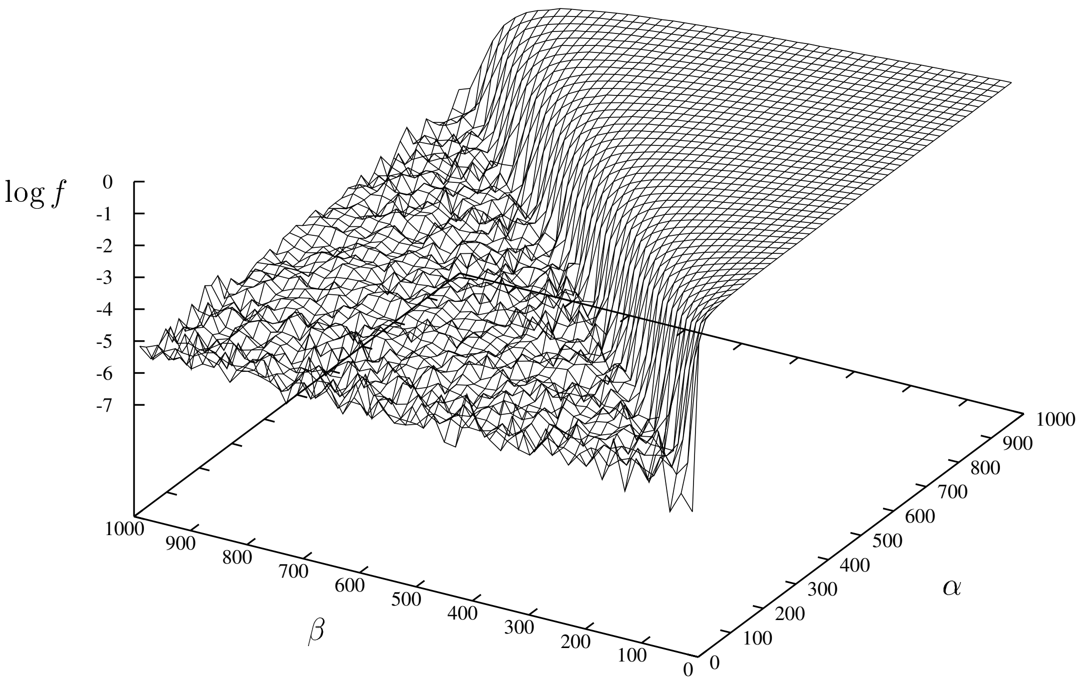

Figure 25: Graph of $\log f$ over $(\alpha, \beta) \in [0, 1000] \times [0, 1000]$.

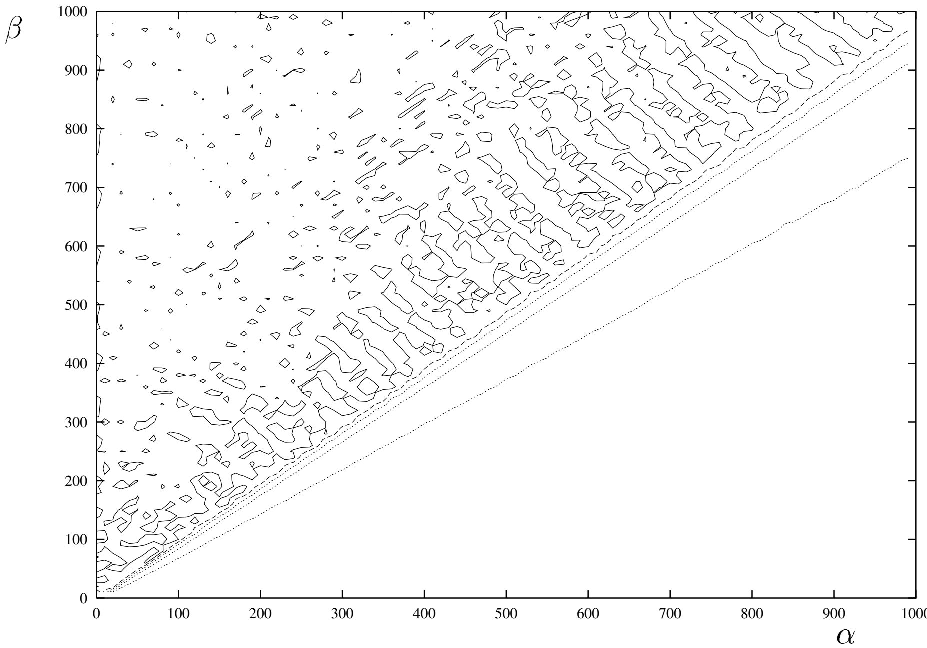

Figure 26: Contour plot of $\log f$ for $(\alpha, \beta) \in [0, 1000] \times [0, 1000]$, where $\log f$ equals -5 on the solid curves, -4 on the dashed ones, and -3, -2 or -1 on the dotted curves.

on the same domain is displayed in figure 24. Figures 25 and 26 show the same in the larger domain $[0, 1000] \times [0, 1000]$. Clearly, the fraction of integrability suddenly drops from nearly 1 to nearly 0 as β/α increases through 1. In the region where $\beta/\alpha > 1$ an intricate structure can be observed. For small α, changes in the fraction of integrability are correlated to jumps of the 'lowest' invariant circle, but for larger α this correlation is lost, compare figure 27.

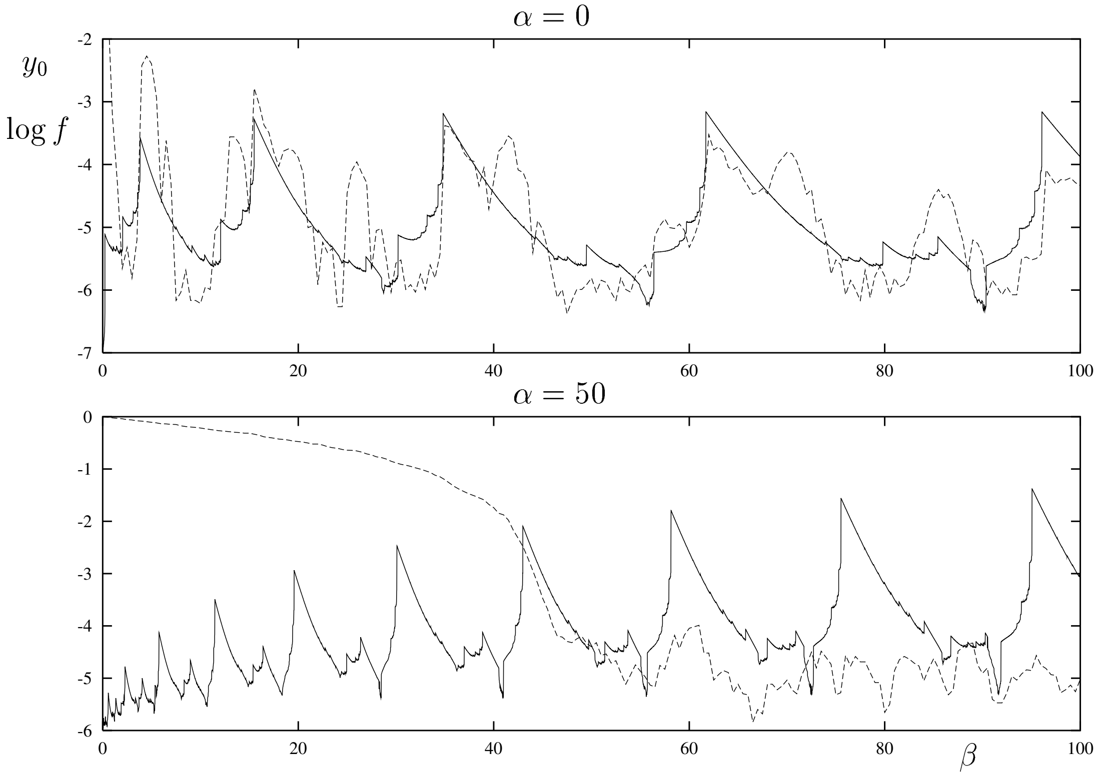

Figure 27: Graphs over β of y_0 (solid curve) and $\log f$ (dashed curve) for fixed $\alpha = 0$ and 50. For convenience the first curve is rescaled by $y \mapsto 2y - 7$ in the upper diagram, and by $y \mapsto 2y - 6$ in the lower one. At $\alpha = 0$ the jumps in y_0 are clearly accompanied by increases in f. At $\alpha = 50$ this correlation is lost.

For a more detailed analysis, we plot on the line $\beta = 1.21\alpha$ the rotation number of the 'lowest' invariant circle and the fraction of integrability, as a function of $\sqrt{\alpha}$, see figure 28. In the displayed domain, the rotation number is well approximated by a sawtooth of frequency 1.66, while the fraction of integrability has frequency [1] close to 1.49. Thus these phenomena are unrelated.

A possible explanation for this loss of correlation is that for small α the jumps correspond to large islands that enter the 'region of interest', and thus contribute to the coherent dynamics, while at large α these islands are smaller and at the

[1] We matched it with a first order harmonic, which captures the frequency with an error of less than 0.1%. To get a better fit with the data, one has to add more harmonics, but since we are only interested in the frequency, this is not needed for our purposes.

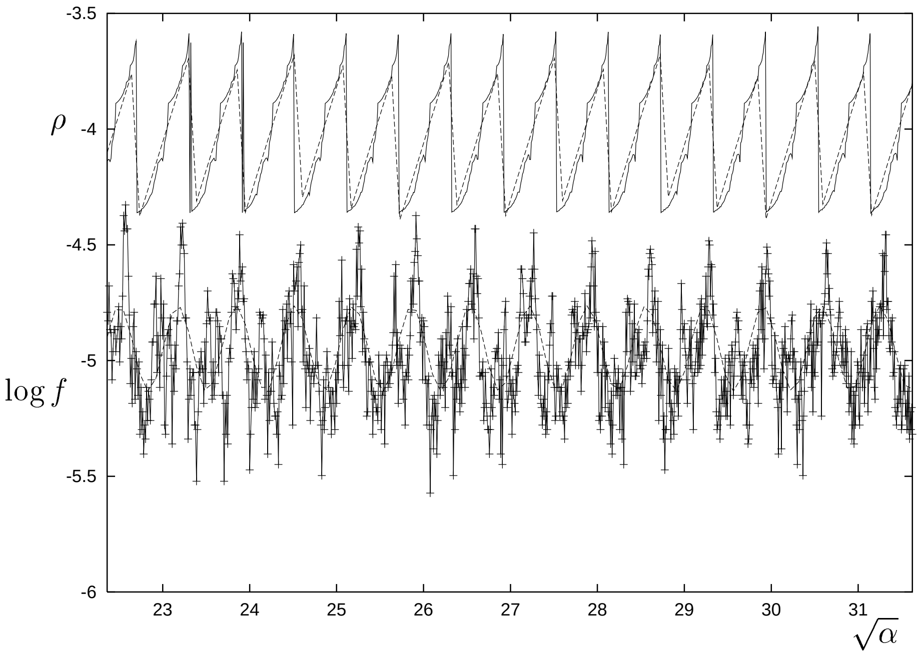

Figure 28: The rotation number ρ of the 'lowest' invariant circle (upper graph), and the logarithm $\log f$ of the fraction of integrability (lower graph), plotted as functions of $\sqrt{\alpha}$ on the line $\beta = 1.21\alpha$, together with approximating periodic functions (dashed). The first is translated vertically over -4.5 for convenience, and is well approximated by the 'sawtooth' $\rho = a\{b(\sqrt{\alpha} - c)\} - 4.5$, where $\{\ \}$ denotes the fractional part, and $a = 0.728 \pm 5 \cdot 10^{-3}$, $b = 1.66366 \pm 3 \cdot 10^{-5}$, $c = 0.47089 \pm 4 \cdot 10^{-5}$. The second resembles $\log f = a \sin(2\pi b(\sqrt{\alpha} - c)) + d$, where $a = 0.184 \pm 7 \cdot 10^{-3}$, $b = 1.485 \pm 1 \cdot 10^{-3}$, $c = -0.56 \pm 2 \cdot 10^{-2}$ and $d = -4.948 \pm 8 \cdot 10^{-3}$.

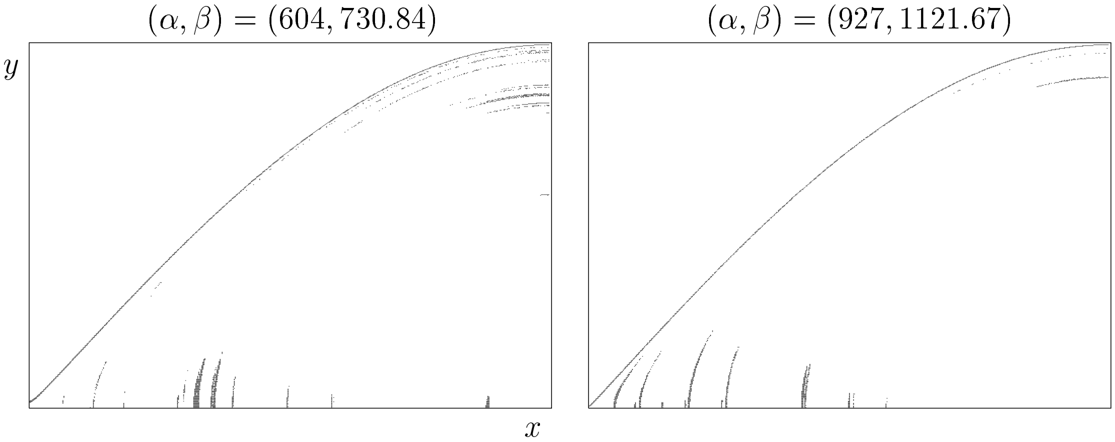

Figure 29: The location of coherent dynamics in the 'region of interest' in phase space, at the indicated parameter points on the line $\beta = 1.21\alpha$. The displayed domain is $(x, y) \in [0, \pi] \times [0, C(\alpha, \beta)]$ in both cases, where C is the maximal y-coordinate of the 'lowest' invariant circle.

same time the 'region of interest' is larger. Moreover, as we will see below, there are other stable islands, mostly around fixed and period two points, that change the fraction of integrability, also compare section 4. To analyze this we compute at parameter points on the line $\beta = 1.21\alpha$ the regions in phase space where the dynamics is coherent. Figure 29 shows two typical examples. We observe that the integrable dynamics is concentrated on the horizontal axis and, to a lesser extent, the line $x = \pi$.

Figures 30 and 32 display the location of integrable dynamics on these two lines, respectively, as a function of $\sqrt{\alpha}$, on the same parameter line $\beta = 1.21\alpha$ as before. They show a very nice, regular pattern of 'lobsters'. (The name is suggested by the magnification displayed in figure 31.) In the first figure, the lobsters are organized in horizontal strips of the form $x = \text{constant}/\sqrt{\alpha}$, as indicated. In the second figure, the pattern follows the shape $y = 2\sqrt{\alpha+\beta} - \text{constant}/\sqrt{\alpha}$, where the first term is the adiabatic estimate of the 'region of interest' for large parameter values. We remark that the vertical axis in figure 32 is scaled by this factor, hence in this figure the pattern is given by the graph of $1 - \text{constant}/\alpha$.

At other lines of constant β/α we obtain a similar pattern, compare figure 4 above. In this diagram, taken on the parameter line $\beta = \alpha$, we also find large islands near the lower equilibrium. A blowup of a small part of figure 30 is shown in figure 31.

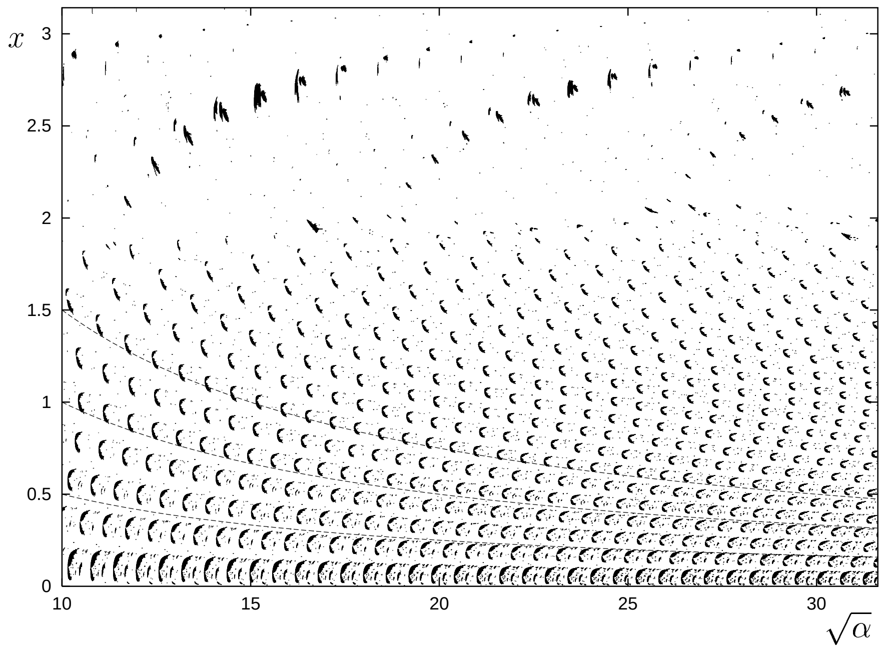

Figure 30: The location of coherent dynamics on the x-axis in phase space, plotted against $\sqrt{\alpha}$ on the line $\beta = 1.21\alpha$. The pattern of lobsters is organized in rows $x = \text{constant}/\sqrt{\alpha}$, as indicated by the dashed curves.

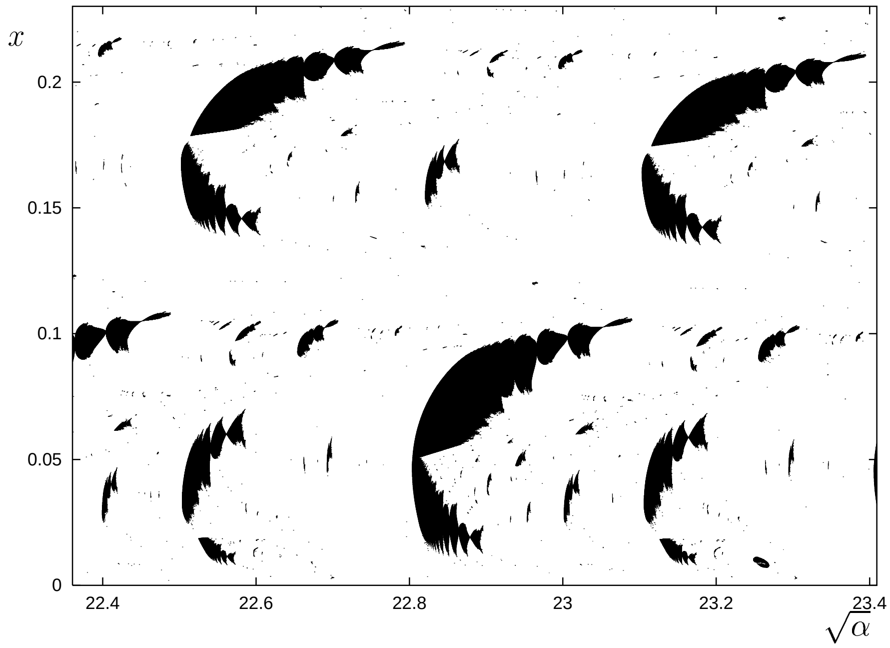

Figure 31: Blowup of a part of figure 30, showing a pattern of large and 'baby' lobsters.

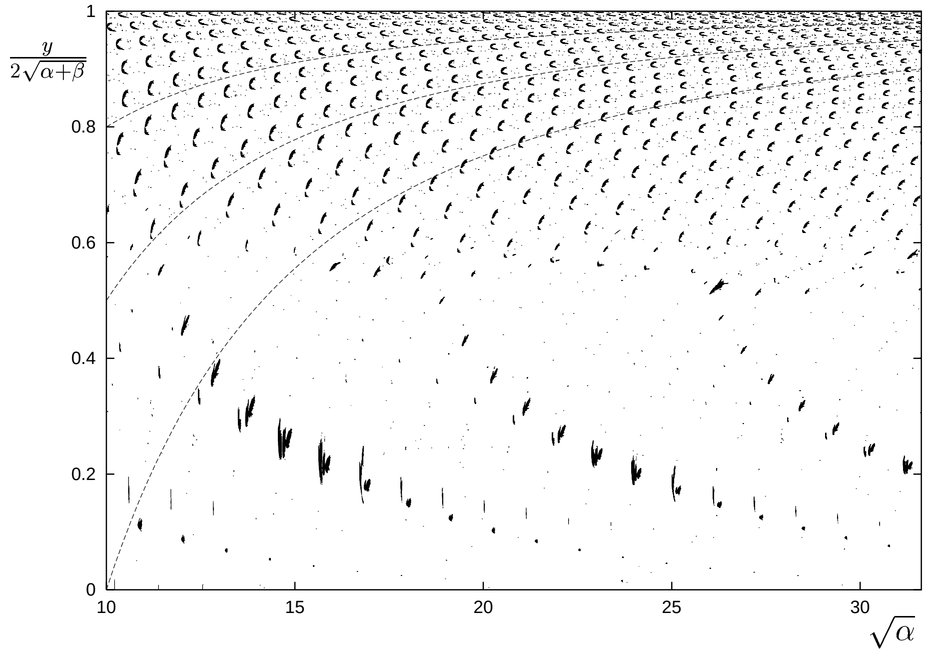

Figure 32: The location of coherent dynamics on the line $x = \pi$ in phase space, plotted against $\sqrt{\alpha}$ on the line $\beta = 1.21\alpha$. The lobsters are lying in rows of the form $y = 2\sqrt{\alpha + \beta} - \text{constant}/\sqrt{\alpha}$, as indicated by the dashed curves.

4 Numerical study of the coherent dynamics

The goal of this section is to study the coherent (and to a lesser extent the non-coherent) dynamics of the Poincaré map in several fundamental domains in the parameter plane, and to determine to what extent this dynamics differs from one domain to another. The concept of fundamental domains was introduced in section 2. In some fundamental domains near the origin of the parameter plane and some further away, this dynamics is described using both analytical and numerical means. An integrable approximation to the Poincaré map P, valid for small β, is used as a starting point for the investigation of the dynamics. Analytical results regarding periodic orbits, their stability type and bifurcations can be extended to a larger part of the parameter plane by numerical continuation. Numerical methods (like continuation) also serve to describe aspects of the coherent dynamics not covered by the integrable model.

As said before, in section 1.2, it is our conjecture that fundamental domains of the same type show similar dynamics. This is true for the stability types and bifurcations of the two equilibria. Moreover, there are other bifurcations with large contributions to the coherent dynamics, that are unrelated to the equilibria, but nonetheless seem to comply with the fundamental domain structure. Near the origin of the parameter plane the dynamics of the nonlinear system varies largely from one domain to the other. In domains farther away there is a big chaotic component in the 'region of interest', that seems to be due mainly to invariant manifolds of unstable equilibria. On the other hand, other islands of stability, not associated to the equilibria, become important. We refer to Simó [Sim01] and section 3.5 for more details.

4.1 Method and sketch of the results

Let us now describe our method of research and its results in more detail. To describe the dynamics of P in an arbitrary fundamental domain, we start with the integrable approximation, obtained by Broer et al. [BHN98, BHNV99, BV92], using perturbation theory. This yields a 'skeleton' for the dynamics in any fundamental domain in the parameter plane, that is, it describes the stability types and bifurcations of the upper and lower equilibrium of the forced pendulum. The dynamics of P is restricted by its symmetries S and R, see section 2.

Using these analytical ingredients, the dynamics of the Poincaré map is investigated numerically. First, to get an overview of the phenomena that can occur, we simply compute phase portraits of the Poincaré map by numerical integration, where the locations of periodic points bifurcated from the equilibria and stable and unstable invariant manifolds of the equilibria (when unstable) are shown. Then follows an analysis of the observed dynamical objects. Here numerical continuation is used to obtain bifurcation diagrams, locate periodic points, and compute curves of codimension one bifurcation points in the parameter plane.

We consider some fundamental domains near the origin of the parameter plane, and only one farther away, since for large parameter values the Poincaré map restricted to the 'region of interest' is mainly chaotic, and seems to vary little (in a qualitative sense) with the parameters. The two equilibria are unstable except in very narrow regions in the parameter plane. Thus we conclude that, for fundamental domains far away from $(\alpha, \beta) = (0, 0)$ the Poincaré map has little coherent dynamics and is qualitatively the same in domains of the same type.

In the domains near the origin the coherent dynamics is very rich. To start with, we retrieve the bifurcations of the upper and lower equilibria that were found in the integrable skeleton. Because of the symmetries S and R the location of a periodic point born in a bifurcation at one of the equilibria is restricted to the lines $y = 0$, $x = 0$ and $x = \pi$.

There are several phenomena in these phase portraits that are not found in the skeleton. Numerically computed bifurcation diagrams show that the periodic points bifurcating from the upper and lower equilibrium rapidly undergo further bifurcations if they are stable. For numerical evidence that this is the start of period doubling cascades we refer to Kim and Hu [KH98] and McLaughlin [McL81]. All periodic points seem either to go towards the upper or lower equilibrium or to escape from the equilibria in the y direction as the parameter β increases.

Furthermore, there are large stable regions above and below the lower equilibrium, coming from the broken invariant circle winding around phase space with rotation number 1, i.e., consisting of points where the underlying vector field has frequency 1 in the x-direction. The fixed point in the center of the stable region undergoes period doubling and pitchfork bifurcations. Moreover, we find $1:3$ resonance bifurcations here, and expect also $p : q$ resonances of higher order.

There are more stable regions on the x-axis, originating from a saddle-center bifurcation. Both the stable and unstable period two points born at this bifurcation undergo pitchfork bifurcations.

At any periodic point subharmonic bifurcations occur when the eigenvalues of the linearized Poincaré map pass through a resonance. We investigate this for the two equilibria, concentrating on the $1 : 3$ resonance. All bifurcations mentioned above take place on curves in the parameter plane, that for large parameter values either converge to the α axis or to one of the stability boundaries of the upper equilibrium.

Finally there is chaos. Invariant circles around stable periodic points and winding around the cylindrical phase space are interlaced with resonant dynamics. Indeed, the Poincaré-Birkhoff theorem [Bir13, Bir25] implies that in between any two invariant circles there exist periodic points of all intermediate rational rotation numbers. Moreover, there is a 'chaotic sea' in the 'region of interest', that seems to grow as β increases. At the same time the stable domains in this region seem to get smaller, although their relative measure remains positive, due to the fact that the number of islands increases with α and β, see Neishtadt et al. [NST97] and Giorgilli et al. [GLS97]. In particular this shows that there is no ergodicity in the whole region of interest, even at high parameter values, also compare section 3.5 where we computed the fraction of integrability in this region.

The 'chaotic sea' mentioned above can be associated with a transversal hyperbolic periodic point that generates it by homoclinic intersections, as follows. When invariant manifolds of hyperbolic points have transversal intersections, most nearby orbits form clouds. It is generally conjectured that the closure of these orbits is an ergodic set of positive Lebesgue measure, see Arnol'd and Avez [AA68]. On the other hand, generically the 'chaotic sea' is densely filled with islands of elliptic periodic points, see Robinson [Rob70]. So the 'chaotic sea' probably is a nowhere dense set of positive area. A similar phenomenon was first observed in the Hénon-Heiles system, cf. Hénon and Heiles [HH64] and, e.g., Moser [Mos68], and can be found in many other examples.

Remark 18 : This can be compared to the dissipative case of the Hénon family, for which Benedicks et al. [BC91, BY93] show that there exists a set of parameter points (a, b) of positive Lebesgue measure where the map has a strange attractor. This is the closure of the unstable manifold of the saddle point, and is ergodic with respect to an SBR measure. For other parameter values it has a periodic attractor. For a parameter set of positive Lebesgue measure the Hénon attractor has a positive Lyapunov exponent almost everywhere, cf. [BY93, You98]. It is widely conjectured that the same holds for 'chaotic seas' of other conservative and dissipative systems, in particular the standard map, compare Viana [Via00].

Let us present an overview of the remainder of this section. The integrable skeleton is described in section 4.2, the phase portraits of P are computed in section 4.3, and section 4.4 analyzes their dynamical features. Section 4.5 presents an extended stability diagram in the parameter plane, including curves of codimension one bifurcation points.

4.2 Integrable skeleton

As mentioned before, the integrable approximation of the Poincaré map of the forced pendulum, obtained by Broer et al. [BHN98, BHNV99, BV92], is valid for small β, and by continuation yields a skeleton for the dynamics on the whole parameter plane, that describes the stability types and bifurcations of the upper and lower equilibrium, as well as the configuration of the periodic points bifurcating from them. In this section the skeleton is described, first for an arbitrary fundamental domain, then in more detail for the fundamental domains that are studied in the following subsections.

We recall that figures 8 and 9 show stability diagrams and phase portraits of the integrable approximations near the lower and upper equilibrium, respectively. The following lemma shows that *all* the bifurcations (except subharmonics of period ≥ 3) of the two equilibria are given by these integrable approximations, and hence the stability types and bifurcations of the equilibria (and the configuration of periodic points resulting from the bifurcations) are known at any parameter point.

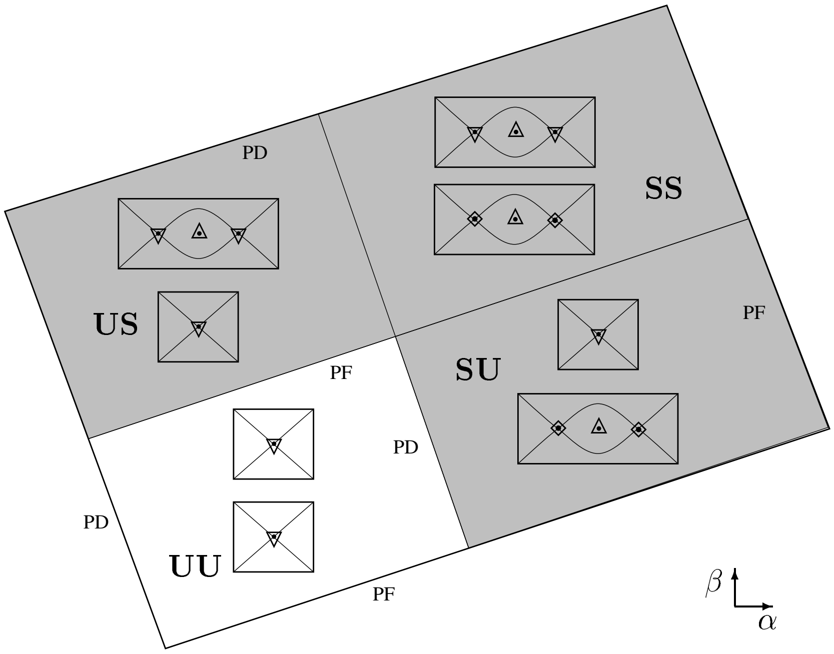

Figure 33: Sketch of the phase portraits of the integrable skeleton in a fundamental domain. The bifurcations on the stability boundaries may differ depending on the type of domain. In each region the upper equilibrium is in the top phase portrait, and the lower in the bottom one.

Lemma 19 *The eigenvalues of the linearized Poincaré map at the upper or lower equilibrium are ± 1 on curves in the parameter plane of the form*

$$\mathbb{R} \ni \beta \mapsto (\alpha, \beta) = (f(\beta), \beta) \in \mathbb{R}^2,$$

for some analytic function f. At these curves the stability of the equilibrium changes.

The lemma implies that all stability curves intersect the α axis (possibly at negative α values), and hence are already present in the integrable approximation. A proof of the lemma is given in appendix D.

The stability boundaries form the boundaries of the fundamental domains, and depending on the bifurcation types at these boundaries, there are four types of fundamental domains (and some special cases near the α and β axes), see section 2. Figure 33 shows for one of the types a stability diagram with phase portraits of the skeleton. We note that the stability types of the periodic points bifurcating from the equilibria can change due to further bifurcations. Furthermore, the schemes are not in proportion, as in the actual phase portraits the periodic points are mostly very close to the upper equilibrium, or far away (in y-direction) from both equilibria.

The diagram only shows the periodic points that bifurcate in this domain. Of course there may be other periodic points present that bifurcated from the equilibria in other domains. For the other types of fundamental domains the picture looks the

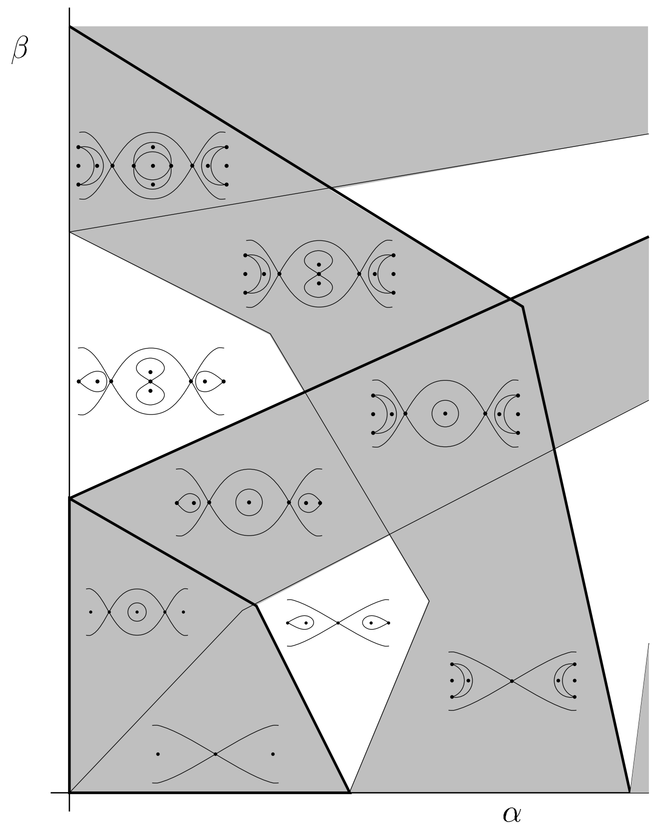

Figure 34: Sketch of the phase portraits of the integrable skeleton in the fundamental domains $(1,1)$, $(2,1)$, and $(2,2)$, where all periodic points bifurcated from the equilibria are indicated, as well as the direction (x or y) in which they bifurcate. The boundaries of the fundamental domains are indicated by thicker curves.

same, except that the bifurcations and periods of the points bifurcating from the equilibria differ.

In the next subsection phase portraits of P are computed in the three fundamental domains $(1,1)$, $(2,1)$ and $(2,2)$ near the origin, and the domain $(12,6)$ farther away. For an explanation of the codification we refer back to figure 11. Figure 34 contains the skeletons for the first three domains. The domains are not proportional, in order to show the phase portraits of the skeletons more clearly. The phase portraits also indicate the direction in which the bifurcated periodic points go. Because of the symmetries S and R of P this has to be either the x- or y-direction. It is not useful to show skeletons for the last two domains, since they have too many periodic points.

Remark 20 : The lowest stability boundary of the upper equilibrium is a curve passing through $(\alpha, \beta) = (0,0)$. The others are obtained by computing a stability boundary of the lower equilibrium and reflecting it in the β axis, as explained in section 2, also see figure 5. Thus the bifurcations of the upper equilibrium can easily be deduced from those of the lower equilibrium. Because of the symmetry involved here, the local phase portraits at the upper equilibrium have to be rotated over 90 degrees compared to those of the lower equilibrium in figure 8, see Broer and Vegter [BV92].

4.3 Phase portraits

To get an overview of the dynamics of P we study its phase portraits at representative parameter points in three fundamental domains $(1, 1)$, $(2, 1)$, and $(2, 2)$ near the origin of the parameter plane, and the domain $(12, 6)$ farther away.

For the first three domains, representative parameter points are selected by computing phase portraits at lattice points in the parameter plane, and sorting out interesting ones. Since the regions of stability in the parameter plane are very small for large β, each region in the domain has its own lattice, instead of a single lattice for the entire domain or the entire parameter plane. In the other two domains the stable regions are extremely tiny (and other stable dynamics become more important, see section 3.5), and therefore phase portraits are computed at a few randomly chosen parameter points, in the region where both equilibria are unstable. Since there is a big difference between the first three domains and the last two, we treat them separately.

The fundamental domains near the origin of the parameter plane

The phase portraits in the fundamental domains $(1, 1)$, $(2, 1)$ and $(2, 2)$ are displayed in figures 35 to 38. Each figure shows a stability diagram and some phase portraits. The stability diagram displays the stability curves in the fundamental domain under consideration, drawn in black, while stability curves outside this domain are grayed. As before, regions (in the current fundamental domain) where the upper or lower equilibrium is stable are shaded. The stability diagram further displays, in each stability region, the phase portrait of the integrable skeleton, compare the previous subsection, especially figure 34 where the same skeletons are shown.

The phase portraits show a representative collection of orbits of P, obtained simply by iteration using an integrator based on Taylor series expansion, cf. Broer and Simó [BS98], Simó [Sim01, appendix], Jorba and Zou [JZ] or appendix C for a discussion of this method. The integrator is very efficient and preserves the symmetries of the system, but (formally) not the symplectic structure, see appendix C.

In each phase portrait, the origin corresponds to the upper equilibrium, while the point $(x, y) = (\pm\pi, 0)$ corresponds to the lower equilibrium. Each diagram (except for the blowups) contains about 46000 points; its caption states the parameter point (α, β) where the phase portrait is taken, and a diagram number corresponding to that in the stability diagram. In case the upper or lower equilibrium is unstable, (finite parts of) its invariant manifolds, computed by DsTool [BGM$^+$92, KO00], are displayed. The locations and stability types of the upper and lower equilibria and the period one and two points bifurcated from them are marked. These are found using numerical continuation.

We now discuss the fundamental domains one by one.

Fundamental domain $(1, 1)$**.** In this domain there are only two stability regions. A stability diagram and phase portraits are displayed in figure 35. In the lower region ('SU') the upper equilibrium is unstable, while the lower is stable, surrounded by invariant circles, see diagram 1 in figure 35. The chaotic sea can be associated to the unstable upper equilibrium, as explained in section 4.

In the upper region ('SS') both equilibria are stable, see diagram 2, but with smaller stability domains than in diagram 1. The four satellites around the upper equilibrium have rotation number $\frac{1}{4}$. They have been observed in another numerical study of the same system, see Acheson [Ach95], and are likely to come from a broken invariant circle. We note that both figures show two stable domains above and below the lower equilibrium, both around a stable fixed point. These are due to a broken invariant circle winding around the cylindrical phase space.

Fundamental domain $(2, 1)$**.** Figure 36 shows a stability diagram and phase portraits. In the lower left region ('UU') the upper and lower equilibria are unstable. As suggested by the location of their invariant manifolds, see diagram 3 in figure 36, a large part of the chaotic sea can be associated to these two points. There is a stable period two orbit on the x-axis, see diagram 3 and the blowup in diagram 4. This is the period two point that bifurcated from the lower equilibrium at the curve of period doubling bifurcations to the left of region 'UU'. Its stability domain decreases as β increases. Again there are two stable domains above and below the lower equilibrium.

In the lower right region ('SU') the lower equilibrium is stable, while the upper is unstable, causing a chaotic sea. For small β the Poincaré map is as in diagram 5. For larger β the stability domain of the lower equilibrium becomes smaller and smaller. Diagram 6 displays the situation near the upper edge of the region. The stable period two points already present in diagram 3 have destabilized (in a pitchfork bifurcation, compare figures 41 and 42 below), and move towards the upper equilibrium as the parameters (α, β) increase. An unstable period two orbit has bifurcated from the lower equilibrium at the stability boundary between regions 'UU' and 'SU', and moves away from the equilibrium in y direction. At some parameter points a stable period two orbit, that did not bifurcate from one of the equilibria, is found on the x axis, like in diagram 6.

In the upper left region ('US') the chaotic sea corresponds to the unstable lower equilibrium. Compared with diagram 3 there are two additional unstable fixed points on the x-axis that bifurcated from the upper equilibrium, that has become stable at this bifurcation. There are 4 satellites around the upper equilibrium, just as in diagram 2 of figure 35. The stable fixed points above and below the lower equilibrium of diagrams 1, 2 and 3 have bifurcated, creating a stable period 2 orbit,

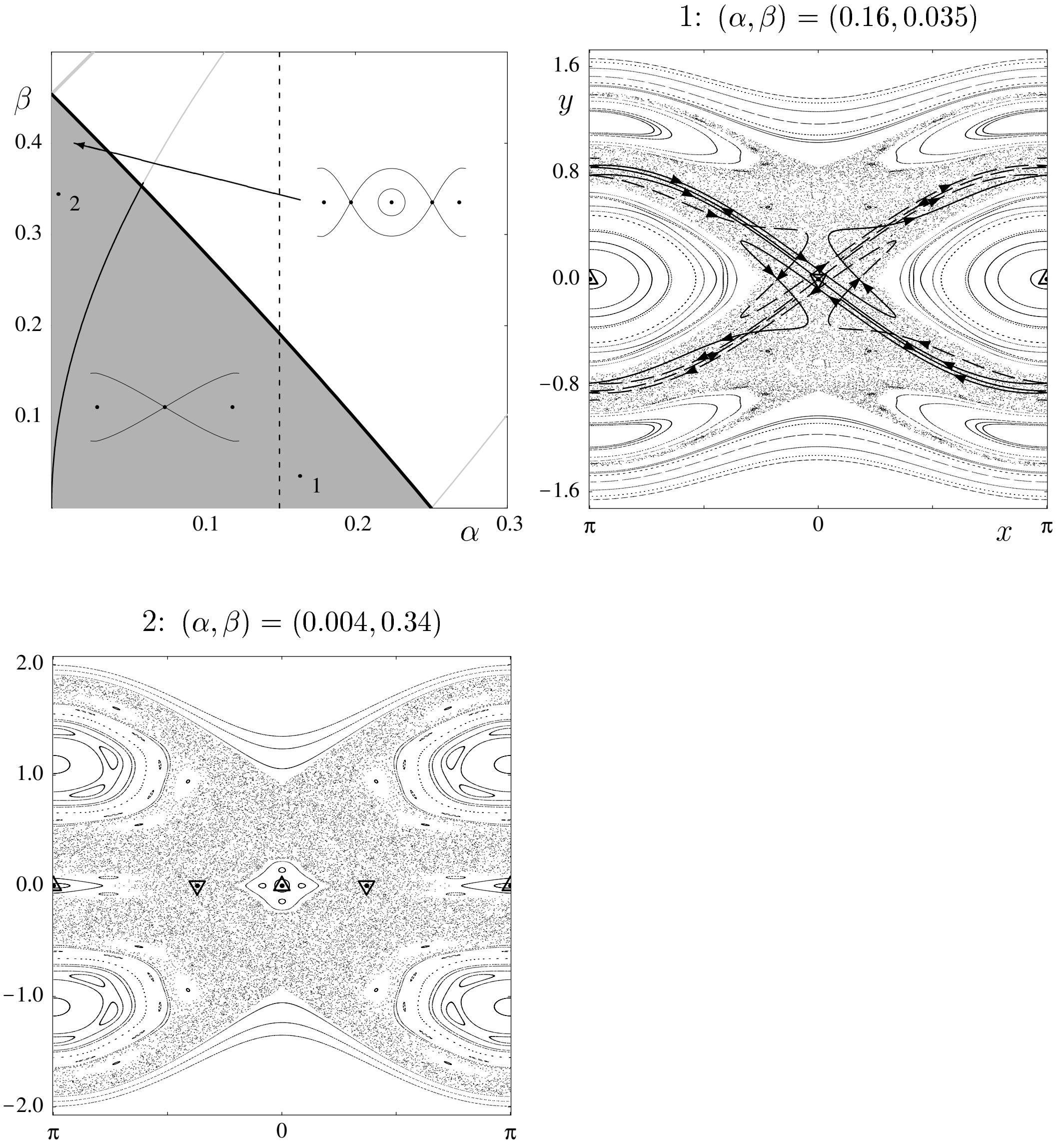

Figure 35: Stability diagram and phase portraits of the Poincaré map P in fundamental domain $(1, 1)$. The stability diagram also shows the bifurcation scheme. The stability curves in the fundamental domain under consideration are drawn in black, outside this domain they are grayed. The dashed vertical lines in the stability diagram indicate the parameter lines where bifurcation diagrams are made, see section 4.4.1 for details. See section 4.3 for more comments, and figure 2 for the coding of periodic points and invariant manifolds.

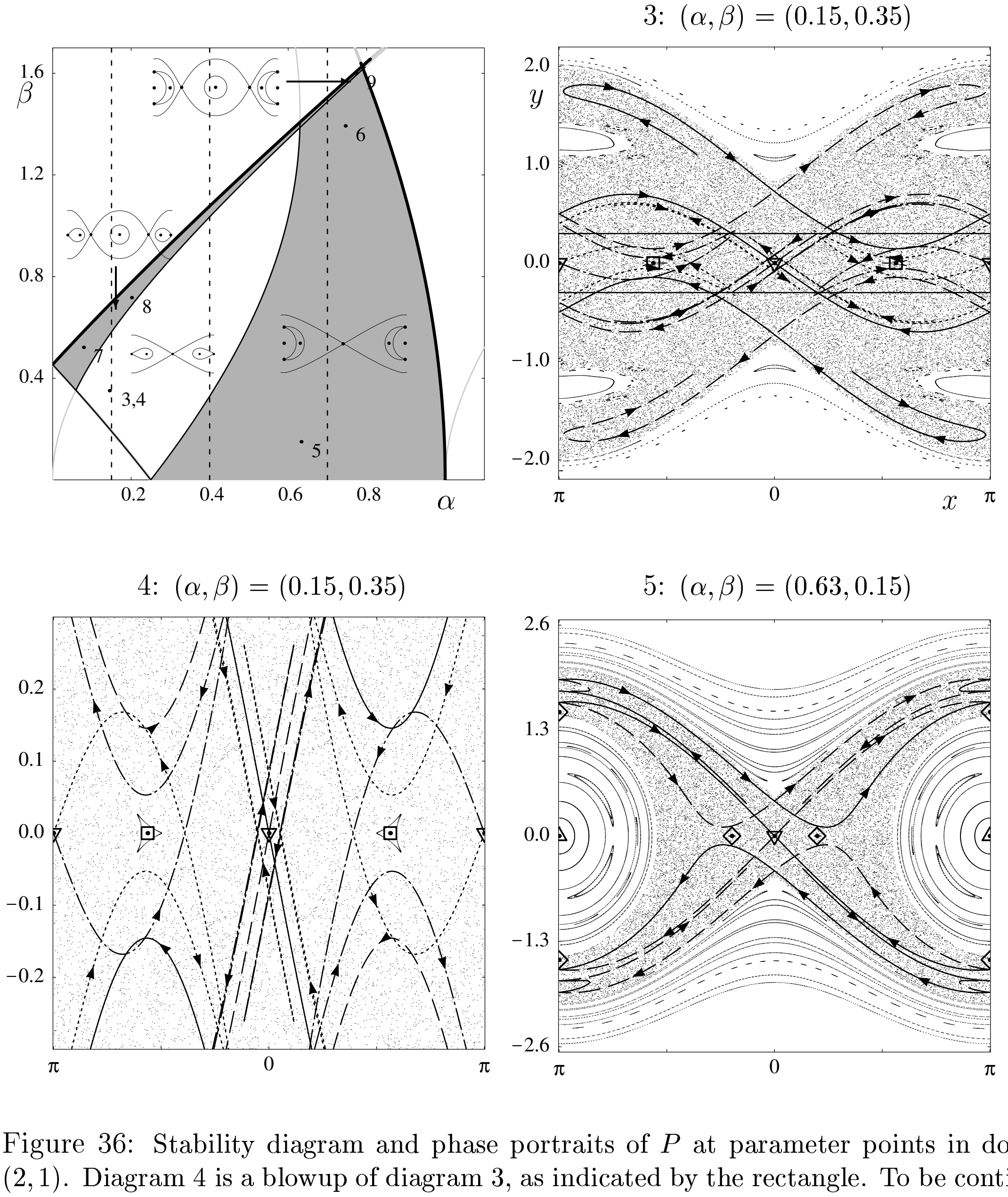

Figure 36: Stability diagram and phase portraits of P at parameter points in domain $(2, 1)$. Diagram 4 is a blowup of diagram 3, as indicated by the rectangle. To be continued in figure 37.

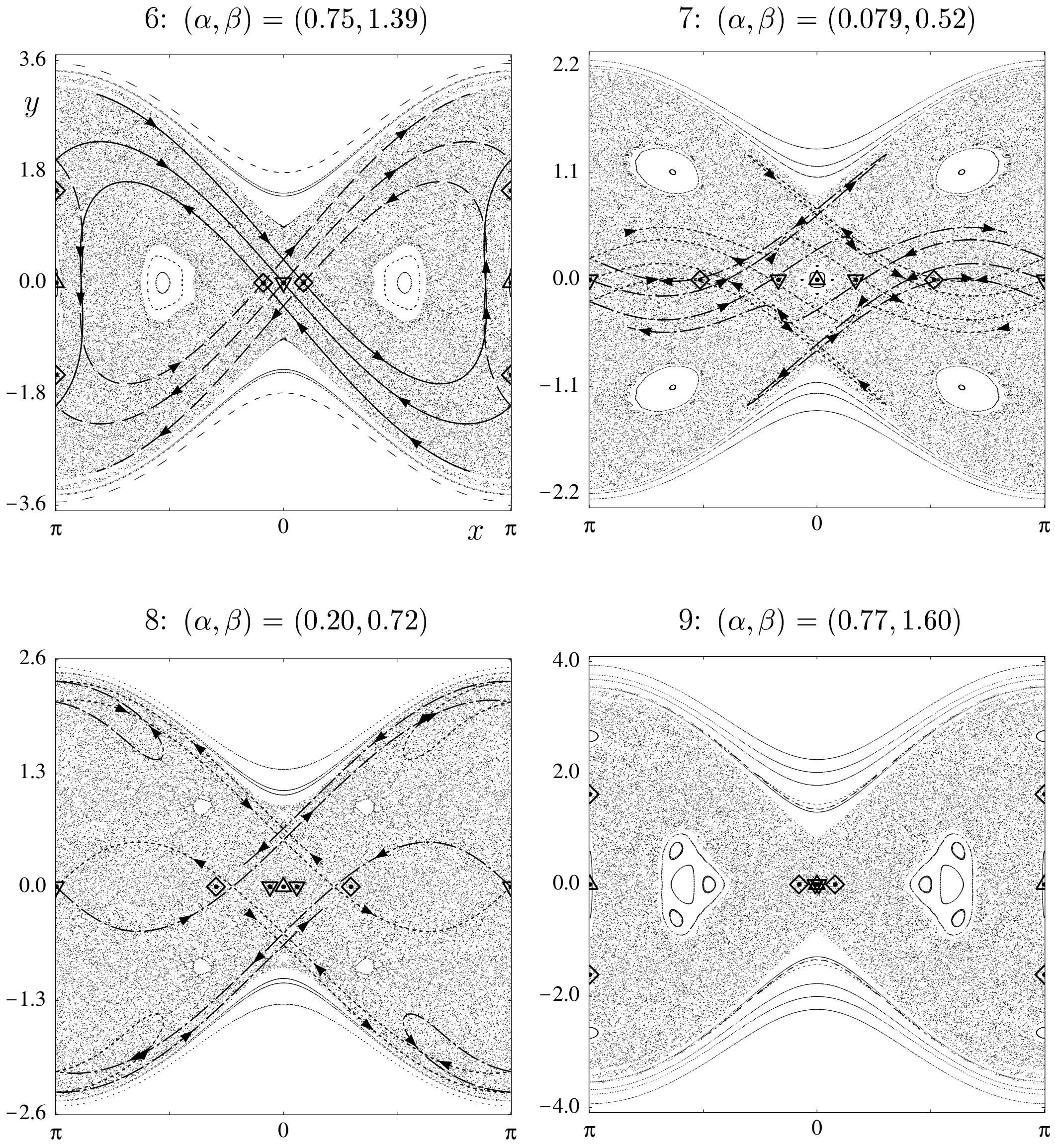

Figure 37: Continued from figure 36. Phase portraits of P at parameter points in domain $(2,1)$.

that moves towards the upper equilibrium as α and β increase, see diagram 8 (also taken from region 'US').

In the upper right region ('SS') both stable equilibria have very small stability domains, see diagram 9. This region in the parameter plane is very narrow, and the Poincaré map does not vary much in it. Therefore just one diagram is shown. The saddle fixed points bifurcated from the upper equilibrium at the stability boundary between regions 'SU' and 'SS' are very close to it and hardly distinguishable. Two unstable period two orbits, bifurcated from the lower equilibrium, can be found on the x-axis and on the line $x = \pi$. Like in region 'SU' there are two period two centers on the x, in this case surrounded by a period 6 satellite. The stable domains above and below the lower equilibrium are also present.

Fundamental domain $(2, 2)$**.** This domain consists of three regions. The stability diagram and Poincaré maps are displayed in figure 38. In the lower left region ('UU') the two unstable equilibria cause a large chaotic sea, see diagrams 10 and 11. Near the upper equilibrium there are two saddles on the x-axis and a period two orbit on the y-axis, all bifurcated from the upper equilibrium, and a period two orbit on the x-axis bifurcated from the lower equilibrium. Both period two orbits were stable when they bifurcated from the equilibria, but have destabilized in further bifurcations. At some parameter values we find four period two points on the x axis, as in diagram 11. If we count the periodic points from left to right, then the first and third form an orbit, and so do the second and fourth.

In the lower right region ('SU') the lower equilibrium has stabilized, with a small stability domain. Two unstable period two points have bifurcated off in y direction. The chaotic see can now be associated with the unstable upper equilibrium. Indeed, its manifolds seem to fill up a large part of the sea, see diagrams 12 to 14. In diagram 12 we find a stable period two orbit on the x axis, surrounded by two (hardly visible) stable period four orbits. As β increases the period 2 points undergo a pitchfork bifurcation, resulting in two additional period 2 centers and saddles, compare diagram 13. As in diagram 11, the first and third center form one orbit, as do the second and fourth. Diagram 14 and its zoom in diagram 15 show that the centers and saddles move away from each other as β increases.

Region 'SS' is very small and the Poincaré map varies little in it. Both stable equilibria have very small stability domains. At some parameter points a stable period two orbit is found on the x-axis, as in diagram 16, where it lies close to the lower equilibrium. Apart from that there seems to be only chaos in the 'region of interest'.

The fundamental domain away from the origin of the parameter plane

Figure 40 shows a stability diagram and phase portraits for the fundamental domain $(12, 6)$. The stability diagram does not show integrable skeletons, since these contain too many periodic points, but simply displays the fundamental domain under consideration, with an indication of the location of the computed phase portraits. The

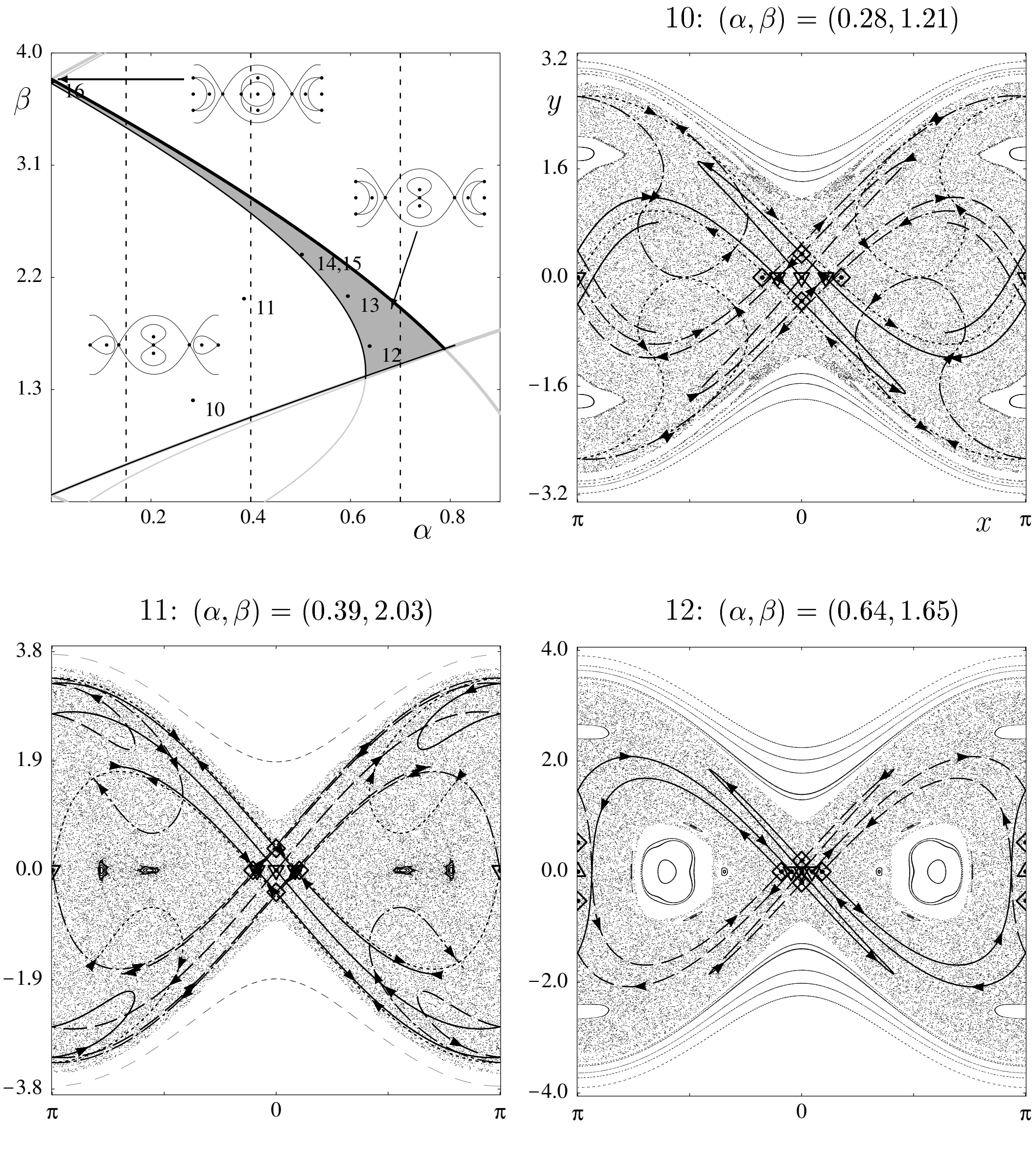

Figure 38: Stability diagram and phase portraits of P at parameter points in domain $(2, 2)$. To be continued in figure 39.

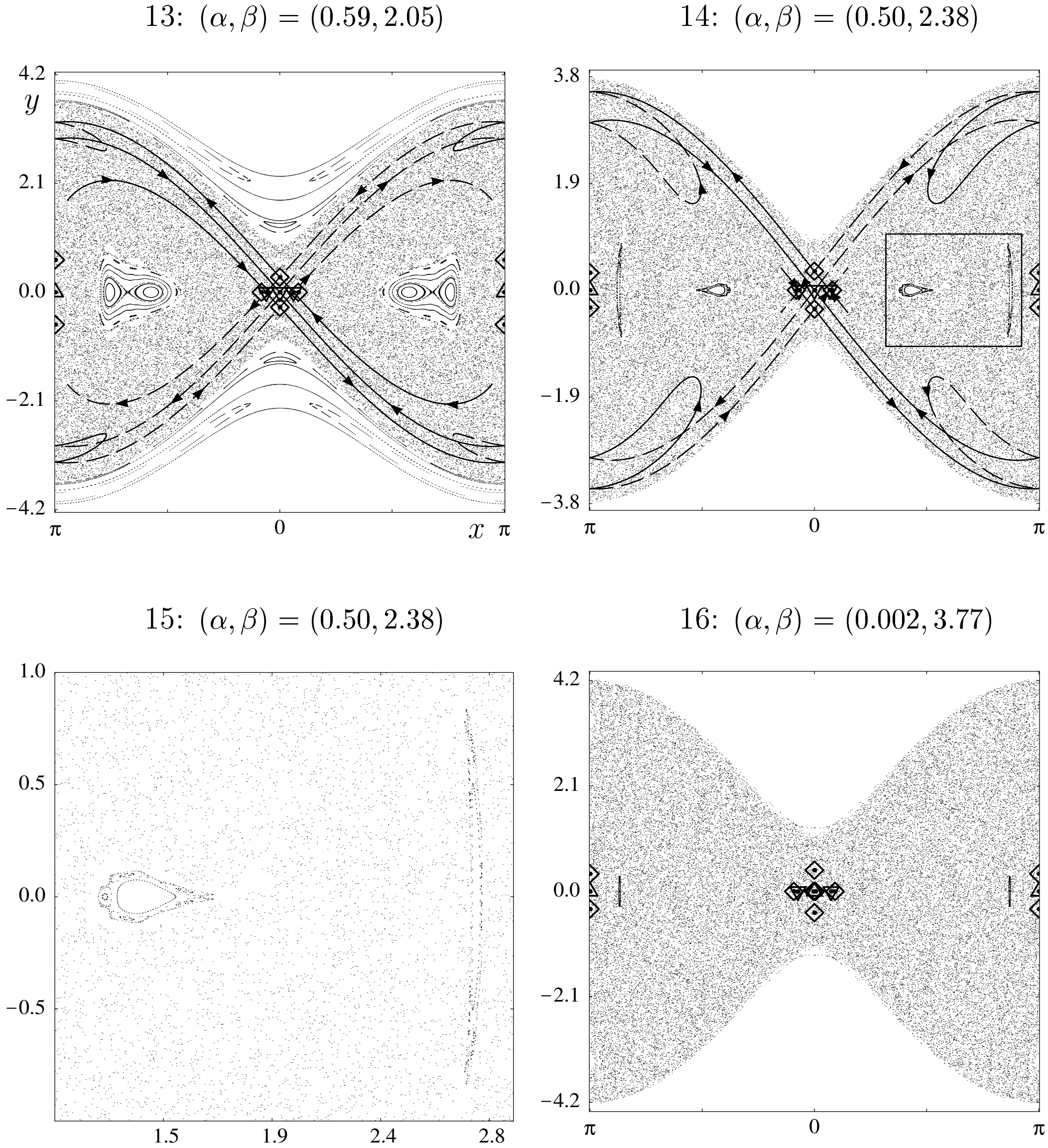

Figure 39: Continued from figure 38. Phase portraits of P at parameter points in domain $(2, 2)$. Diagram 15 is a blowup of diagram 14, as indicated. Diagram 16 is taken from region 'SS'.

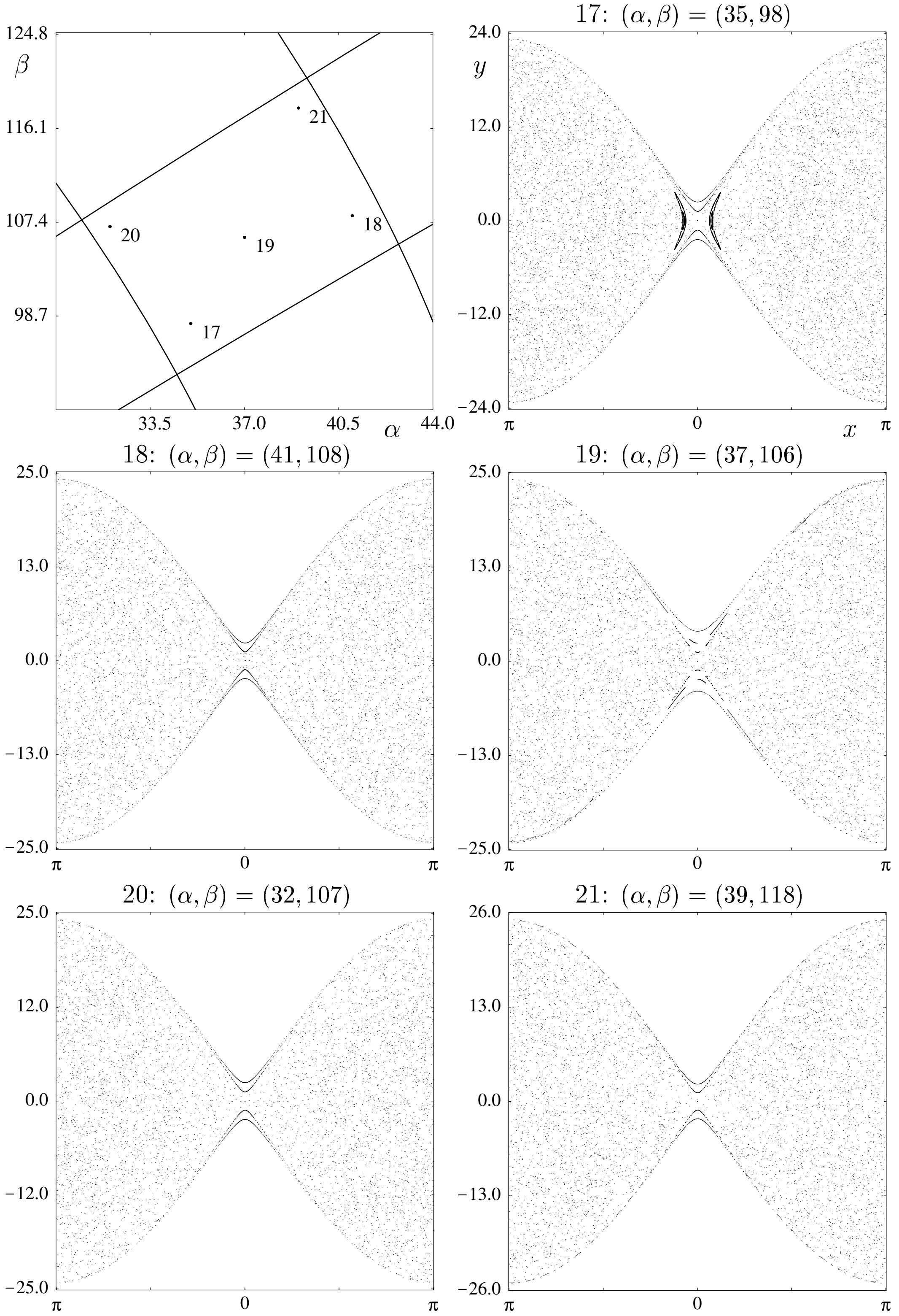

Figure 40: Stability diagram and phase portraits of the Poincaré map at parameter points in fundamental domain $(12, 6)$. See section 4.3 for more comments on the dynamics.

stable regions in the stability diagram are too narrow to be detected, therefore all phase portraits are taken from the region 'UU' where both equilibria are unstable.

The phase portraits display a representative collection of orbits of P. The periodic points that bifurcated from the upper and lower equilibrium are not shown, because there are so many. The phase portraits show only chaotic dynamics, except in diagram 17, where two stable regions surrounding a period two orbit are found on the x-axis. In other domains (of the same type) at large parameter values the dynamics is qualitatively the same.

4.4 Numerical analysis

In this section some of the dynamical features encountered in the phase portraits of the Poincaré map are studied in more detail. The analysis is restricted to the domains near the origin of the parameter plane, since they show the most interesting dynamics. We first give an overview of the phenomena that we want to study, and then discuss them one by one.

The equilibria undergo bifurcations as determined by the skeleton. Section 4.4.1 presents numerically computed bifurcation diagrams of the equilibria that give more quantitative information, and show the stability types and bifurcations of the periodic points that bifurcated from the equilibria.

In some phase portraits, e.g. diagrams 6 and 9 in figure 36 or diagrams 12 and 16 in figure 38, there is a stable period two orbit on the x axis. It originates from a saddle-center bifurcation. This bifurcation, as well as a subsequent pitchfork bifurcation, resulting in a pair of period two orbits that can be observed in diagrams 11, 13, 14 and 15 in figure 38, is studied in section 4.4.2.

The large stable regions above and below the lower equilibrium, see diagrams 1 and 2 in figure 35, diagrams 3 and 9 in figure 36 and diagrams 10 and 12 in figure 38, are caused by a broken invariant circle. Section 4.4.3 presents a bifurcation analysis.

Finally, around stable periodic points satellites are born at resonances. For the equilibria and their satellites this is discussed in more detail in section 4.4.4.

4.4.1 Bifurcation diagrams of the equilibria

To study the period one and two points of the Poincaré map P bifurcating from the upper and lower equilibria of the pendulum, we compute some bifurcation diagrams at lines $\alpha =$ constant in the parameter plane,with β as bifurcation parameter. We choose the lines $\alpha = 0.15$, $\alpha = 0.4$ and $\alpha = 0.7$. They intersect the three domains near the origin of the parameter plane considered in subsection 4.3, as indicated by vertical lines in the stability diagrams of figures 35 – 38. Other lines give rise to similar bifurcation diagrams. Each diagram is invariant under reflection in the (x, β) and (y, β) planes due to the symmetries S and R.

The bifurcation diagrams are displayed in figures 42 – 44 for the respective parameter lines. They show branches of periodic points emanating from bifurcation points of the upper and lower equilibria, called *primary* branches and bifurcation

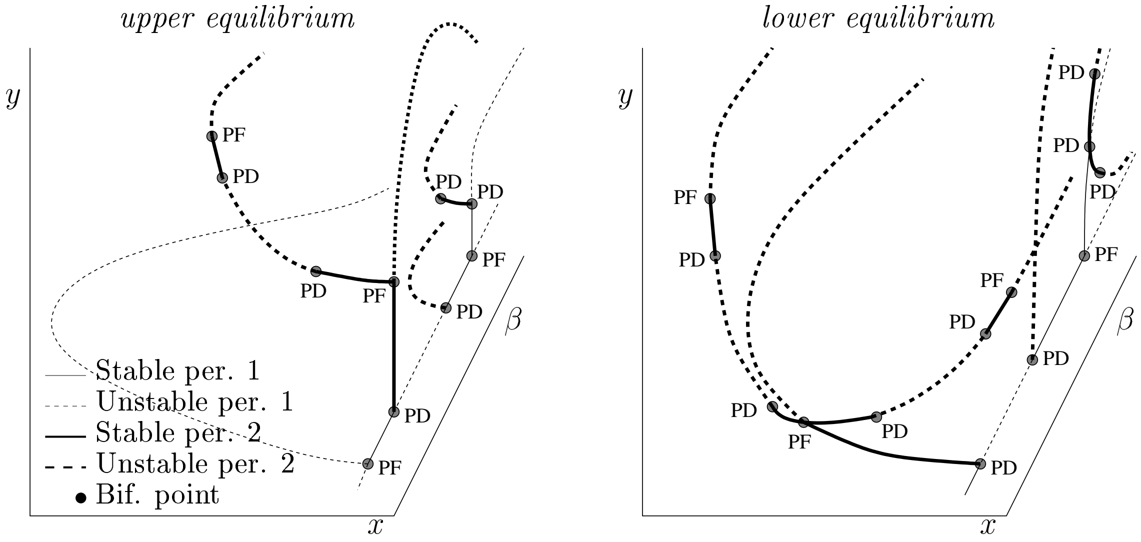

Figure 41: Schematic view of the bifurcation diagrams on lines α = constant. The straight lines parallel to the β-axis correspond to the positions of the equilibria. The distances between bifurcation points and solution branches are exaggerated for clarity. The presented diagram of the upper equilibrium is valid on any line $\alpha =$ constant, that of the lower equilibrium only if the constant is in $(0, \frac{1}{4})$, and has to be adapted otherwise. For simplicity only the branches in one quadrant of (β, x, y)-space are displayed, the others are their S- and R-symmetric counterparts.

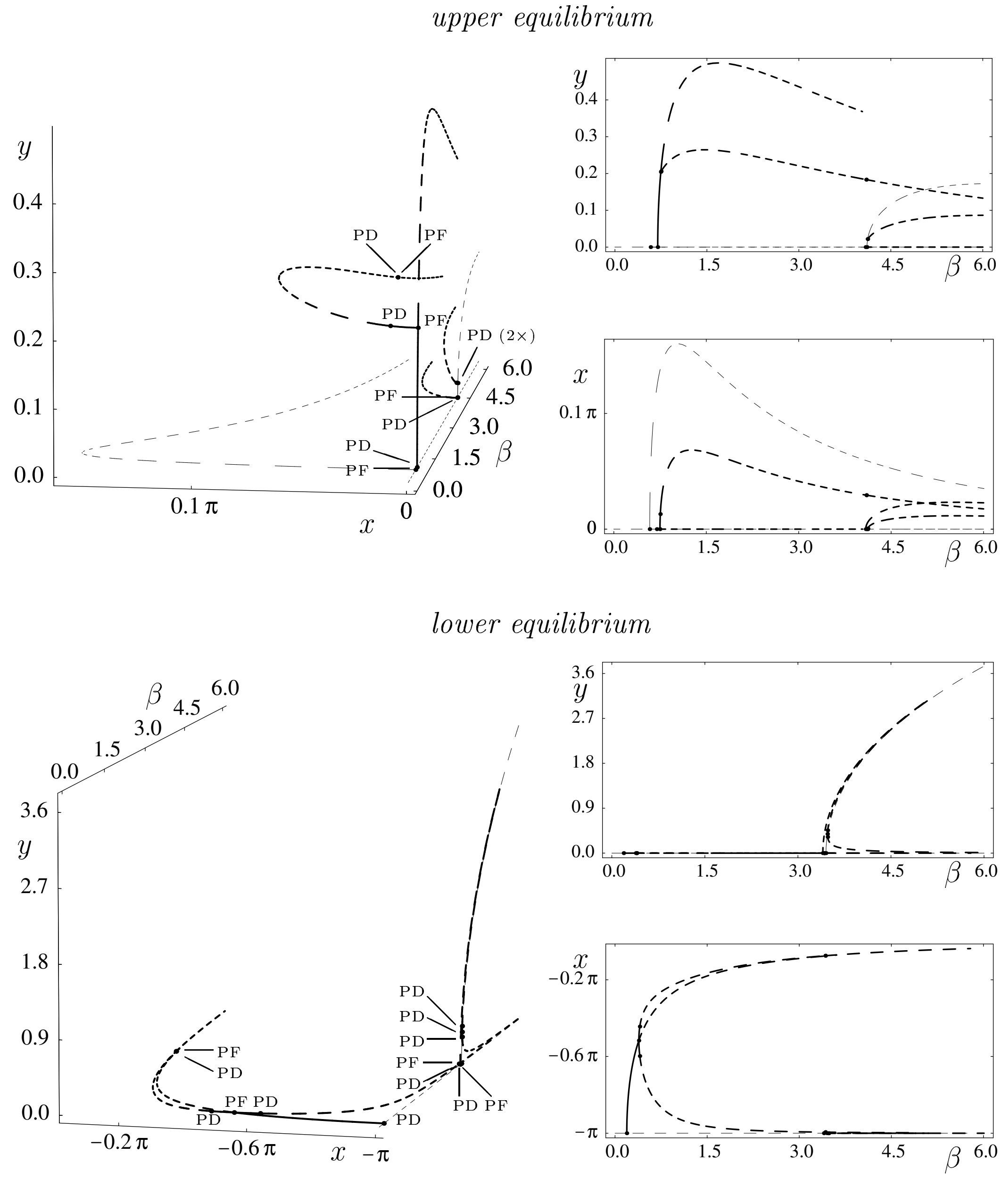

Figure 42: Bifurcation diagrams on the line $\alpha = 0.15$, and their projections onto the (β, x)- and (β, y)-planes, displaying primary and secondary branches of period one and two points of P. The straight lines parallel to the β axis correspond to the positions of the equilibria. For simplicity only the branches in one quadrant of (β, x, y)-space are displayed, the others are their symmetric counterpart under reflection in the (β, x)- or (β, y)-plane. Both diagrams are in agreement with the schemes of figure 41.

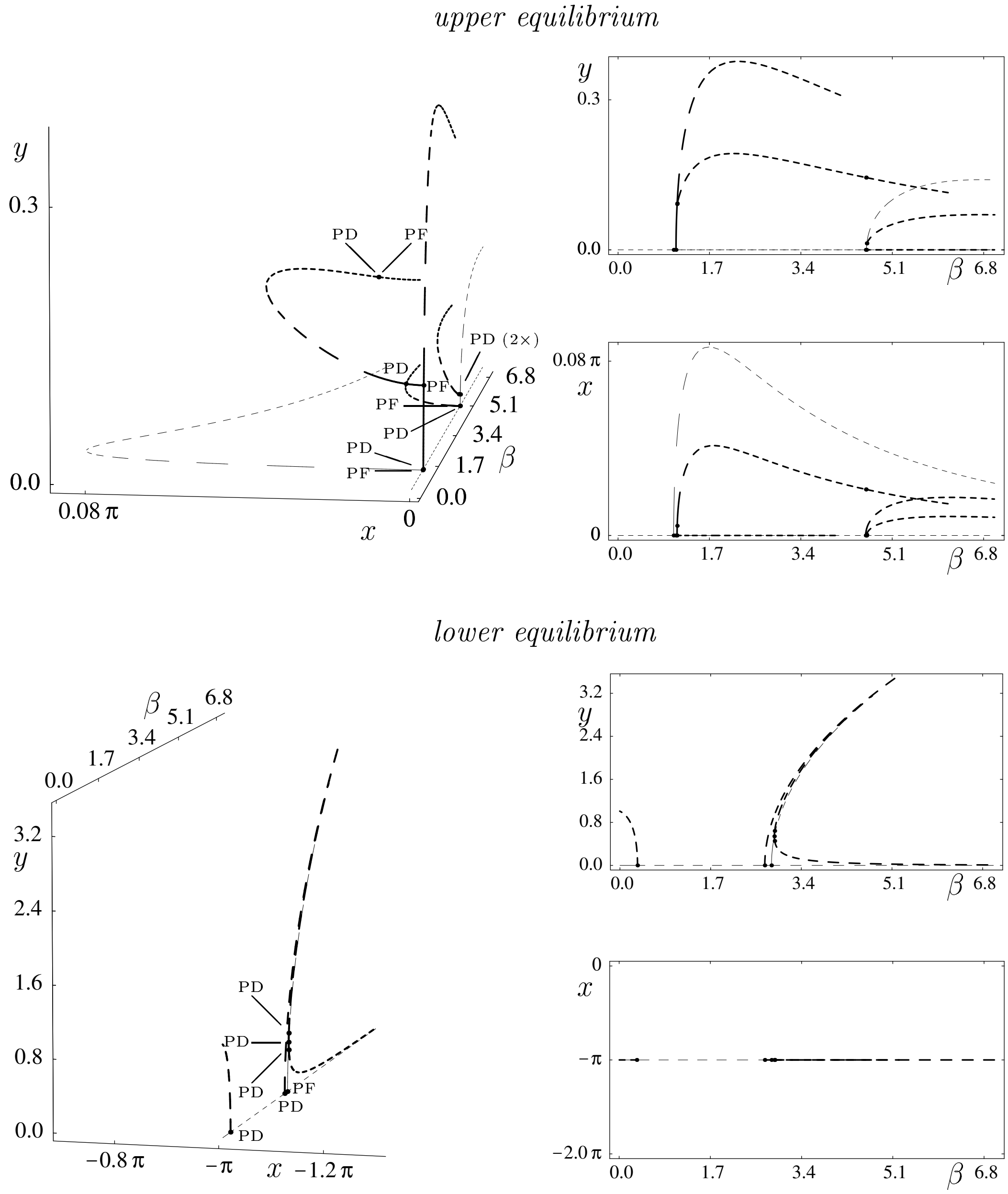

Figure 43: Bifurcation diagrams on the line $\alpha = 0.4$, and their projections onto the (β, x)- and (β, y)-planes, displaying primary and secondary branches of period one and two points of P. As in figure 42, the lines parallel to the β-axis correspond to the positions of the equilibria, and only the branches in one quadrant are displayed. The leftmost stability boundary of the lower equilibrium is not intersected, while the next one is intersected twice. Thus the leftmost period doubling point of the lower equilibrium in figure 41 is absent, but *another* period doubling has appeared, with a branch turning back towards $\beta = 0$.

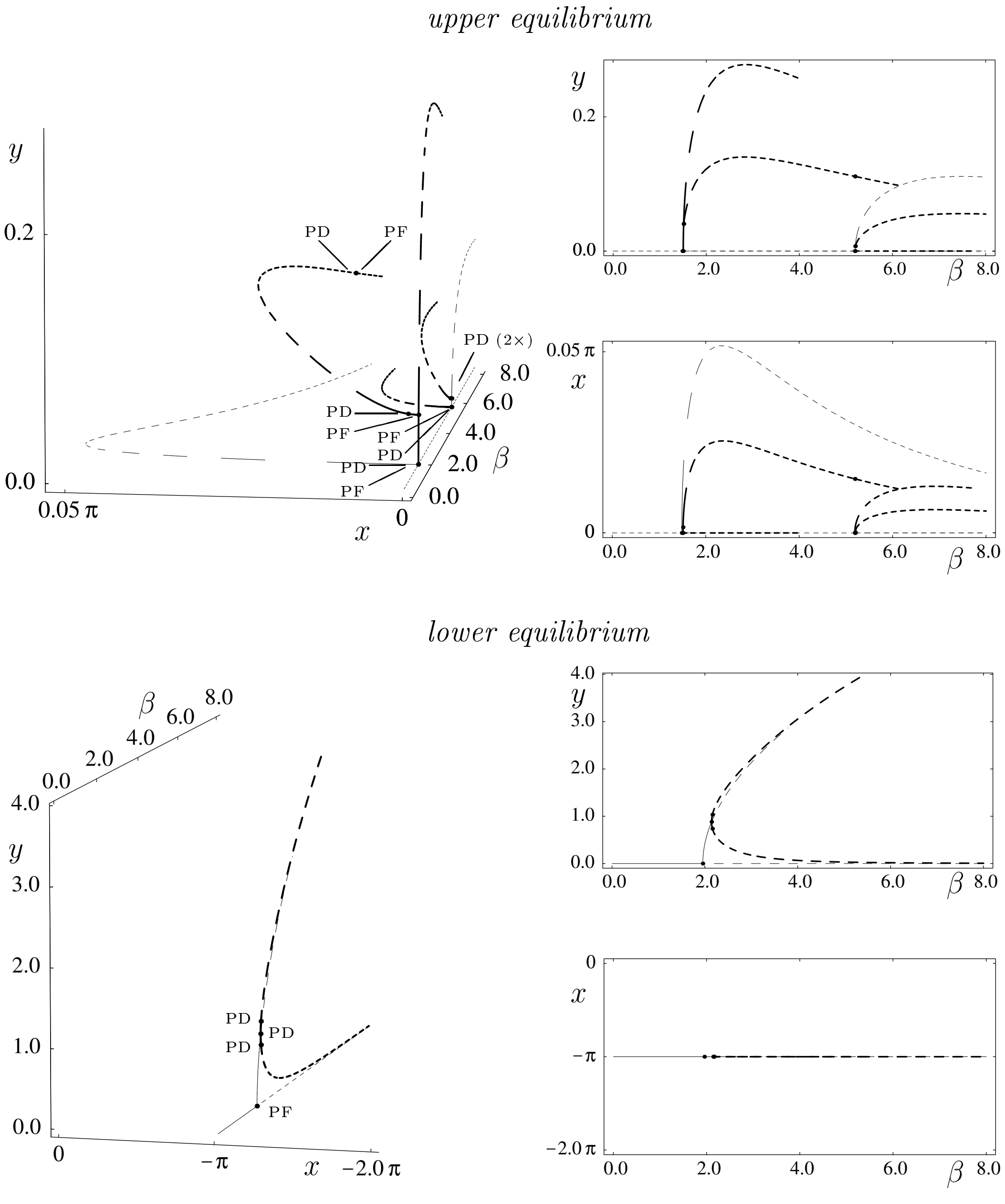

Figure 44: Bifurcation diagrams on the line $\alpha = 0.7$, and their projections onto the (β, x)- and (β, y)-planes, displaying primary and secondary branches of period one and two points of P. The lines parallel to the β-axis correspond to the positions of the equilibria, and only the branches in one quadrant are displayed. Both stability boundaries of the lower equilibrium originating from the first resonance point $(\alpha, \beta) = (\frac{1}{4}, 0)$ are not intersected, so the two period doublings of this equilibrium shown in figure 41 are absent here.

points. The bifurcation points on the primary branches and the periodic points born there are called *secondary*. We note that for simplicity only the branches in one quadrant of (β, x, y)-space are displayed, the others are their symmetric counterpart with respect to the symmetries S and R. Indeed, at each primary bifurcation point, and at some secondary bifurcation points, just one of the two newly born periodic points is shown. The diagrams are obtained by numerical continuation of periodic points. For general background and examples on numerical continuation we refer to Simó [Sim89], Doedel et al. [DKK91a, DKK91b], Kuznetsov [Kuz95] and Castellà and Jorba [CJ00].

Since some of the bifurcation points and their branches are very close together, in figure 41 we present a sketch of the bifurcation diagrams, where the points and branches are easier to distinguish. The bifurcation diagram of the upper equilibrium is qualitatively the same on all lines $\alpha =$ constant, since on any such line one encounters the same bifurcation sequence as β increases from 0. This can be concluded from the stability diagram, see figures 1 and 5. For the lower equilibrium this is not true. For example, both stability curves originating from the first resonance point $(\alpha, \beta) = (\frac{1}{4}, 0)$ intersect the line $\alpha = 0.15$, none intersect the line $\alpha = 0.7$, and for $\alpha = 0.4$ the right hand curve is intersected twice, the other one not at all. The sketch in figure 41 is valid for constant $\alpha \in (0, \frac{1}{4})$, i.e., where any stability curve of the lower equilibrium is intersected exactly once. The examples in figures 43 and 44 illustrate how this diagram should be modified to match other cases.

The bifurcations from the upper and lower equilibria found by Broer et al. [BHN98, BHNV99, BV92], using perturbation theory, agree with the numerical results, compare figures 8 and 9. Because of the symmetries S and R the location of the primary periodic points is restricted to the lines $y = 0$, $x = 0$ and $x = \pi$. In all diagrams we see similar behavior: for the upper equilibrium, as β increases the primary branches first move away from the equilibrium along the x or y axis, but at higher β values they turn back. The secondary branches also go towards the upper equilibrium, but their location is not restricted to the axes.

As β increases, the primary branches of the lower equilibrium move either towards the upper equilibrium along the x-axis, or they escape in y direction along the line $x = \pi$, and do not seem to return. Some of the secondary branches return to the lower equilibrium, while others go to the upper equilibrium or go away in y direction. (Observe that the range of plotted y values is much larger for the lower equilibrium than for the upper equilibrium). Moreover it seems that no periodic point can be stable for a large interval of parameter values. Indeed, any stable periodic point rapidly bifurcates, while unstable points remain in existence over a large parameter range. This is true on primary and secondary branches.

4.4.2 The saddle-center bifurcation

In some of the phase portraits of section 4.3 there are two or four stable period 2 orbits on the x axis that did not bifurcate from one of the equilibria. We analyze these points by computing their bifurcation diagrams and some phase portraits at

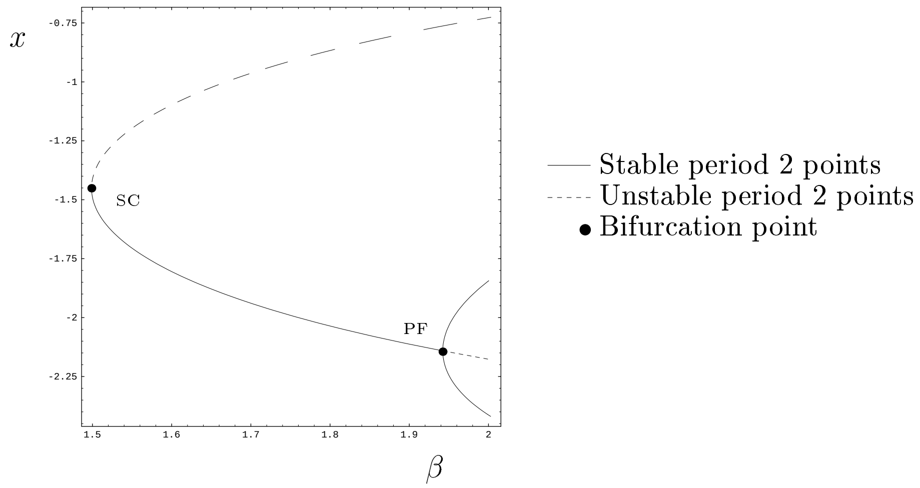

Figure 45: Bifurcation diagram on the line $\alpha = 0.2836$, displaying a saddle-center bifurcation. On the stable branch a pitchfork bifurcation occurs.

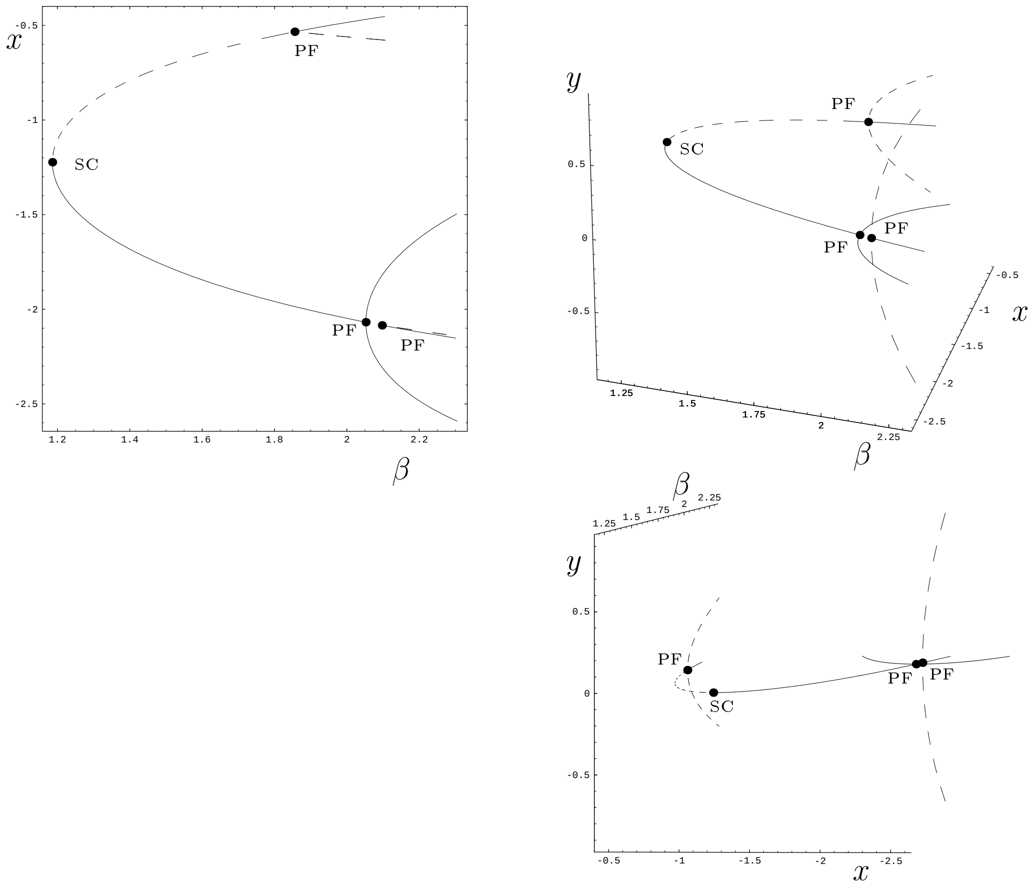

Figure 46: Bifurcation diagram on the line $\alpha = 0.7738$, showing the same bifurcations as the previous diagram, added with a pair of pitchfork points. The three-dimensional bifurcation diagrams to the right, with different view points, show that the branches coming from these two points do not lie in the plane $y = 0$, unlike the other branches. Stability types and bifurcation points are indicated as before.

relevant parameter values.

The bifurcation diagrams are shown in figures 45 and 46. They have β as bifurcation parameter, while α is constant equal to 0.2836 and 0.7738, respectively. (These lines pass through the parameter points where the phase portraits of diagrams 10 and 9 in figures 36 and 38 are taken).

The bifurcation diagrams show a period 2 saddle-center bifurcation. In both figures, we consider the period 2 points to the left of the upper equilibrium. Those to the right are their images under P, and their bifurcation diagrams can be obtained by a reflection $x \mapsto -x$. By symmetry, the branches coming from the saddle-center point satisfy $y = 0$. The stable orbit born at this bifurcation bifurcates further in a pitchfork bifurcation, creating the pair of stable period 2 orbits seen in for example in the phase portrait in figure 38, diagram 14.

Both the saddle-center bifurcation and this pitchfork have codimension 1 and takes place at curves in the parameter plane. These curves are computed in section 4.5 below. In the diagram at $\alpha = 0.7738$ more pitchfork bifurcation points on the stable and unstable branch of the saddle-center bifurcation are found. These have branches with nonzero y-coordinate.

Phase portraits of the Poincaré map are shown in figure 47, for several parameter points on the line $\alpha = 0.2836$. Their captions state the parameter values, and the diagrams also display primary periodic points and invariant manifolds of (unstable) equilibria. In the first phase portrait, at $(\alpha, \beta) = (0.2836, 1.2134)$ — this is the same as diagram 10 in figure 38 — the saddle-center bifurcation has not yet occurred. The bifurcation takes place at $\beta \approx 1.4989$, corresponding to the second diagram. For higher β values there is one stable and one unstable period two orbit on the x-axis, see the diagram at $\beta = 1.6$. The stable orbit undergoes a pitchfork bifurcation at $\beta \approx 1.9423$, that creates a pair of stable period two orbits, see the last diagram. Here the first and third period two point (counted from the left) form an orbit, and so do the second and fourth.

In the last diagram two very small stable regions can be seen at $(x, y) =\approx (\pi, \pm 2.9)$. These are due to another saddle-center bifurcation. Its bifurcation diagram is given in figure 48. This bifurcation diagram is very similar to the previous one. In fact, the curve of saddle-center bifurcations mentioned above yields, by the symmetry $T \circ U$, involving reflection in the β-axis, another curve of saddle-center bifurcations in the parameter plane. It can be shown that the second saddle-center bifurcation lies on the reflected curve, which explains the similarity. See section 4.5 below for more details.

The saddle-center bifurcation is possibly due to the Newhouse phenomenon, cf. [New74, OS93], which states that a homoclinic tangency, like the one in the top left diagram of figure 47, gives rise to infinitely many periodic points, created in saddle-center bifurcations at nearby parameter values. In figure 49 we illustrate this for period 8 points, that are created closer to the tangency than the period 2 points of figure 47. For fixed $\alpha = 0.2836$ as before, the two top diagrams of figure 49 show the x-axis and its image under P^8 shortly before and after the saddle center bifurcation, which takes place approximately at $\beta = 1.3505853379$. One of the

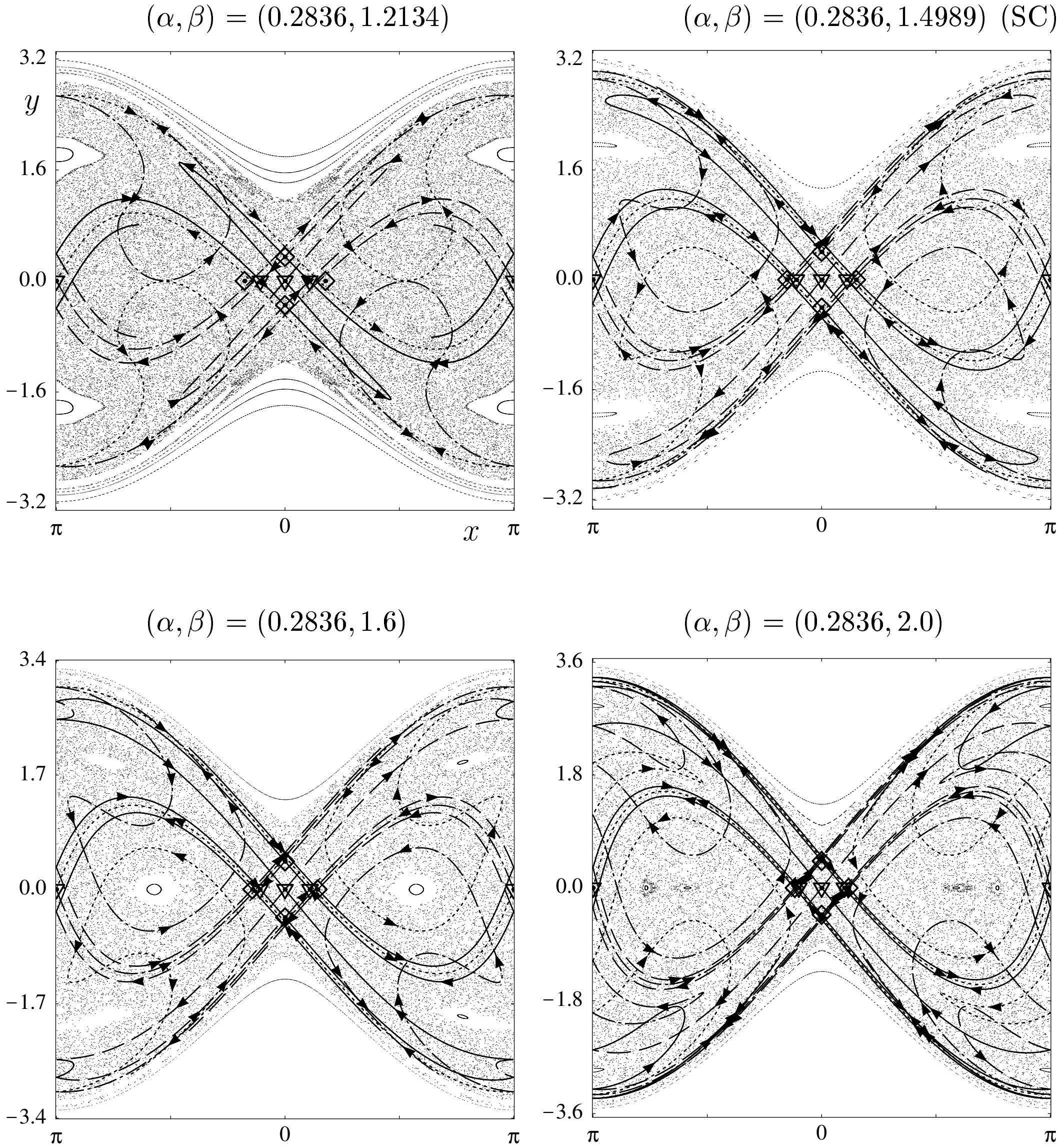

Figure 47: Phase portraits of the Poincaré map P at several parameter points on the line $\alpha = 0.2836$, showing a saddle-center and subsequent pitchfork bifurcation. All centers and saddles involved are of period 2, jumping from the right half plane to the left one, and back. See section 4.4.2 for more comments.

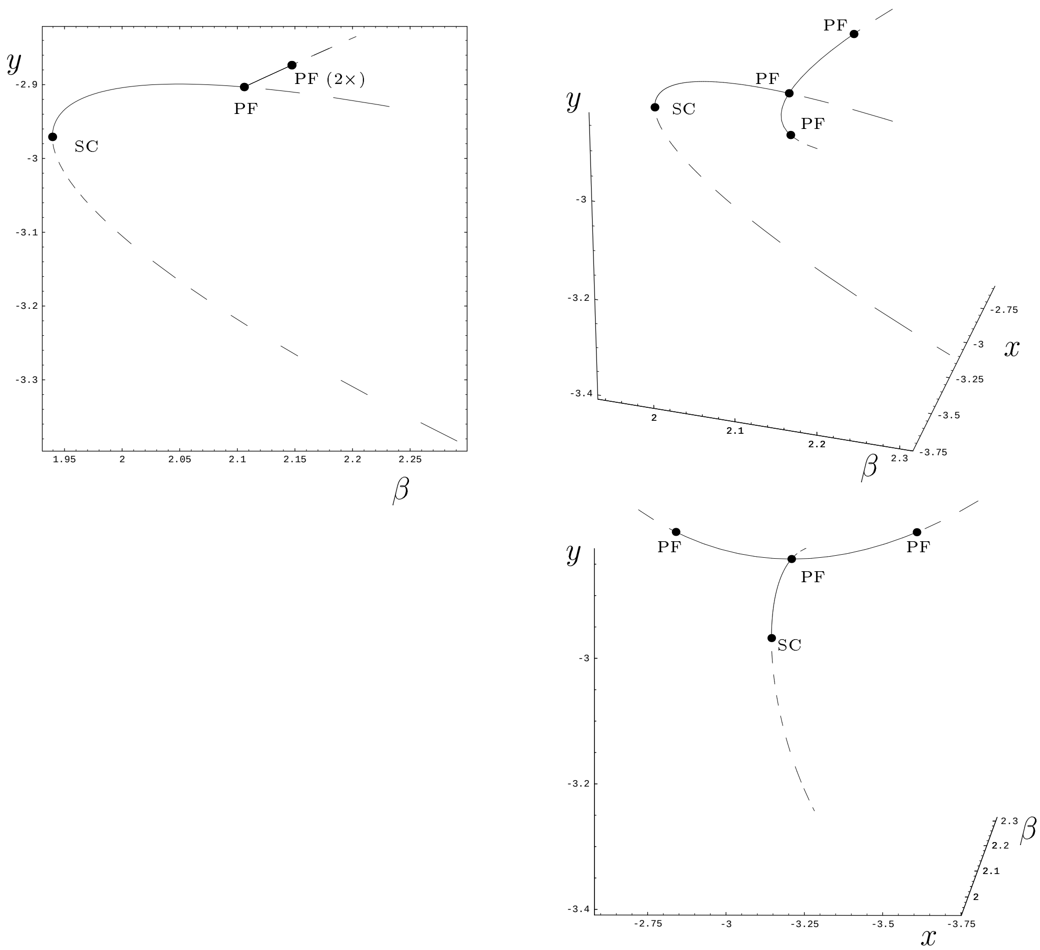

Figure 48: Bifurcation diagram on the line $\alpha = 0.2836$ of a second saddle-center bifurcation, taking place at a higher β value than the previous one, compare figure 45. Qualitatively the bifurcation diagram is the same. The branches of the saddle-center point lie in the plane $x = \pi$, but the other branches do not. Therefore three-dimensional bifurcation diagrams from different view points are added for clarity. Stability types and bifurcation points are indicated as in previous diagrams.

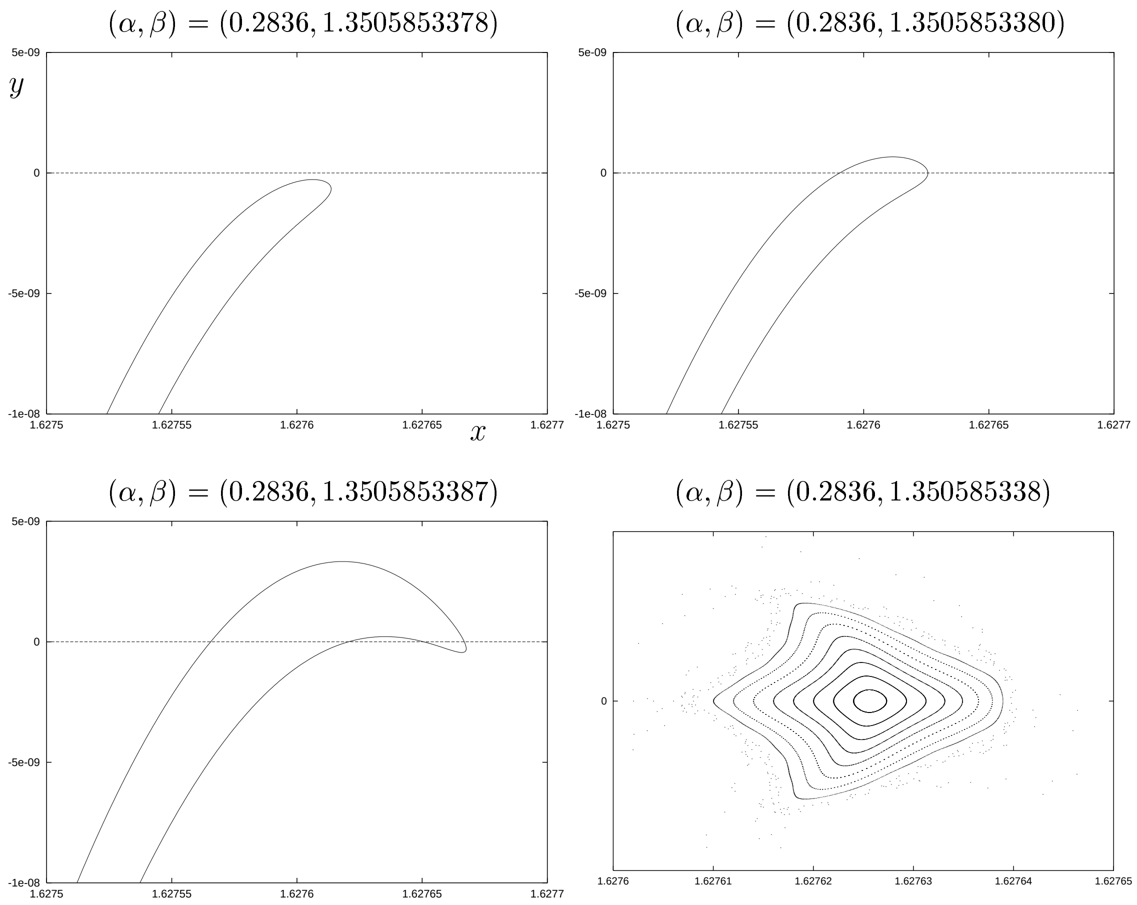

Figure 49: Illustration of the Newhouse phenomenon. Top, and bottom left: Part of the x-axis and its image under P^8, at the indicated parameter points, showing a saddle-center and subsequent period doubling bifurcation. Bottom right: one of the stable period 8 points that is created in the saddle-center bifurcation (and destroyed in the period doubling).

period 8 stable points is shown in the bottom right diagram. At a slightly higher β value, namely $\beta \approx 1.3505853384$, this stable orbit is destroyed in a period doubling bifurcation, as shown in the bottom left diagram. In a similar way, if instead of period 8 we consider a period $2k > 8$, then patterns like the ones displayed in figure 49 appear. The value β_k at which the saddle-center bifurcation occurs tends to the value at which the homoclinic tangency is produced (roughly $\beta_{\text{hom}} = 1.2134$, as seen in figure 47 top left) when k tends to ∞.

4.4.3 The broken invariant circle

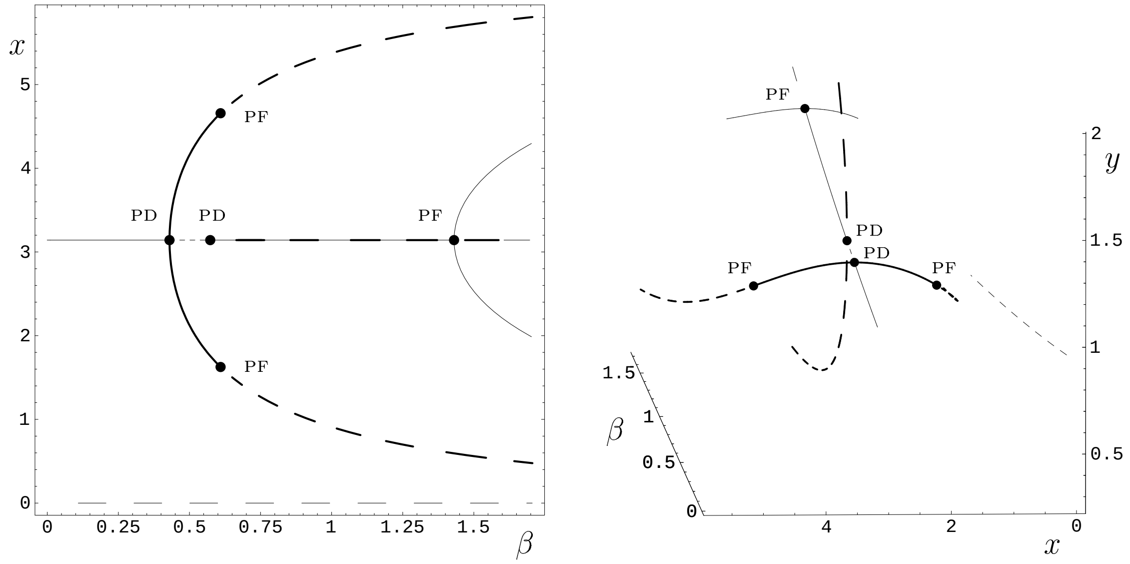

Figure 50: Bifurcation diagram on the line $\alpha = 0.079$, displaying the center and the saddle coming from the broken invariant circle with rotation number 1. The center undergoes two period doubling bifurcations and one pitchfork. Since some of the branches lie in the plane $x = \pi$, a three-dimensional bifurcation diagram is shown as well. Stability types and bifurcation points are indicated as before.

The Poincaré map of the integrable system at $\beta = 0$ has a continuous family of invariant circles winding around the cylindrical phase space, and filling the region above the separatrix. (For simplicity we restrict to circles in the upper half cylinder $y > 0$.) For any $\beta > 0$, generically only circles satisfying a certain Diophantine condition persist, compare section 3.2 and references therein. In particular, the resonant circle with rotation number 1 does not exist for *any* $\beta > 0$, and gives rise to the large stable domains above the lower equilibrium that can be seen in many phase portraits, for example diagrams 1 and 2 in figure 35.

Figures 50 and 51 display bifurcation diagrams at the lines $\alpha = 0.079$ and $\alpha = 0.28$, respectively. For phase portraits we refer back to figure 3. Both bifurcation diagrams show that the invariant circle under consideration is broken for all $\beta > 0$, yielding one stable and one unstable fixed point, at $x = \pi$ and $x = 0$, respectively.

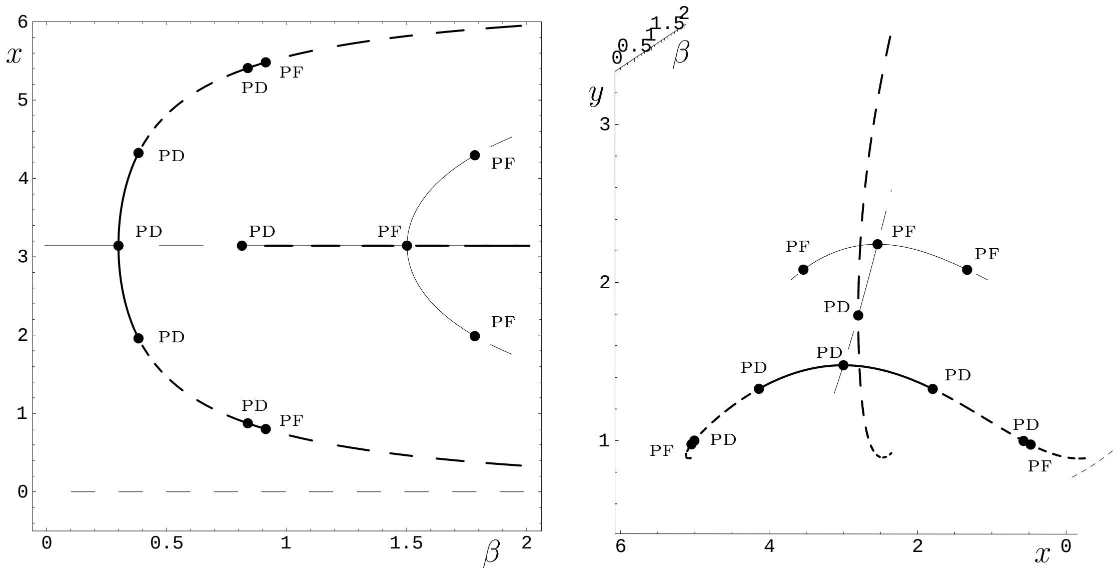

Figure 51: Bifurcation diagram on the line $\alpha = 0.28$ of the same center and saddle as in the previous figure. Now there are some more bifurcation points. Again, a three-dimensional bifurcation diagram is shown for clarity.

The saddle point does not bifurcate, while the center undergoes two period doubling bifurcations, followed by a pitchfork. The first period doubling bifurcation yields a stable period two orbit moving away from the line $x = \pi$, as illustrated by the third diagram of figure 3. This period two orbit in turn undergoes a pitchfork bifurcation, see the diagram at $\beta = 0.65$ in figure 3.

Furthermore, a subharmonic saddle-center bifurcation occurs at $\beta = 0.2148\ldots$, creating (for higher β values) a stable and an unstable period three orbit, near the stable fixed point coming from the broken invariant circle. The stable period three orbit can clearly be seen in the phase portrait at $\beta = 0.22$. It moves away from the stable fixed point as β increases. The unstable period three orbit intersects the stable fixed point at $\beta \approx 0.218$ and $(x, y) \approx (\pi, 1.14)$. At this point the eigenvalues of the linearized Poincaré map DP are (non-real) third roots of unity. This is a generic codimension one bifurcation sequence, compare Duistermaat [Dui84]. A bifurcation diagram is presented in figure 52.

4.4.4 Satellites

This section deals with satellites of the equilibria, that is, strings of stable and unstable periodic orbits of period at least three, that encircle one of the equilibria. Orbits of period one and two are not discussed here: they are born at pitchfork and period doubling bifurcations, respectively, and are already dealt with above. For the forced pendulum satellites of period $q \geq 3$ are created in two different ways, where the symmetries and non-dissipativity of the system play an important role, compare [BV92].

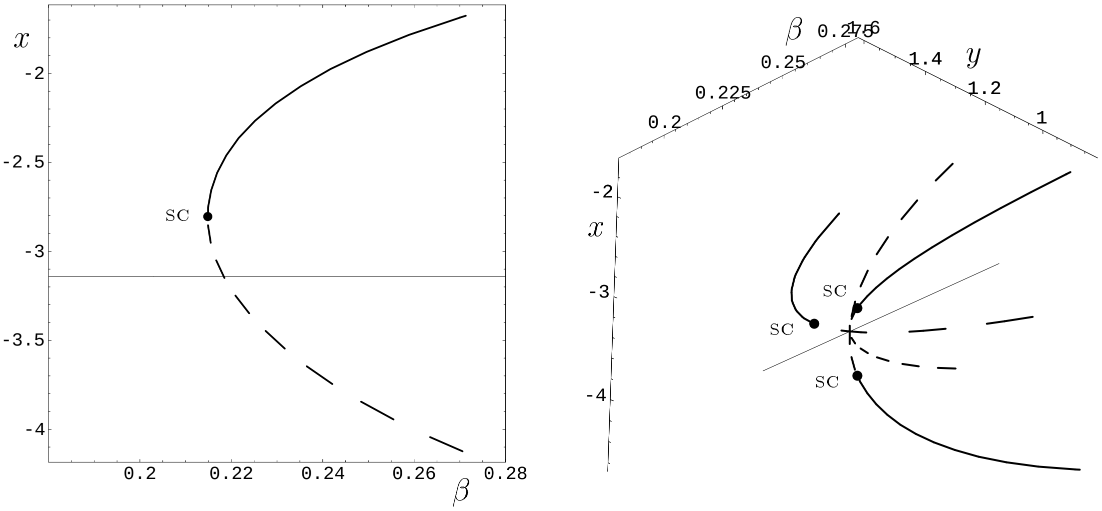

Figure 52: Right: bifurcation diagram on the line $\alpha = 0.079$ of a stable and an unstable period three orbit that are created in a saddle-center bifurcation point at $\beta = 0.2148\ldots$. On the left the projection to (β, x)-space of one of the three branches is shown. (The thicker curves now indicate period three points.) The unstable periodic points intersect the stable fixed point (from the broken invariant circle) at $\beta \approx 0.218$. The curves of periodic points passing through the saddle-center points lie in three different manifolds. Due to symmetry, one is the plane $x = \pi$.

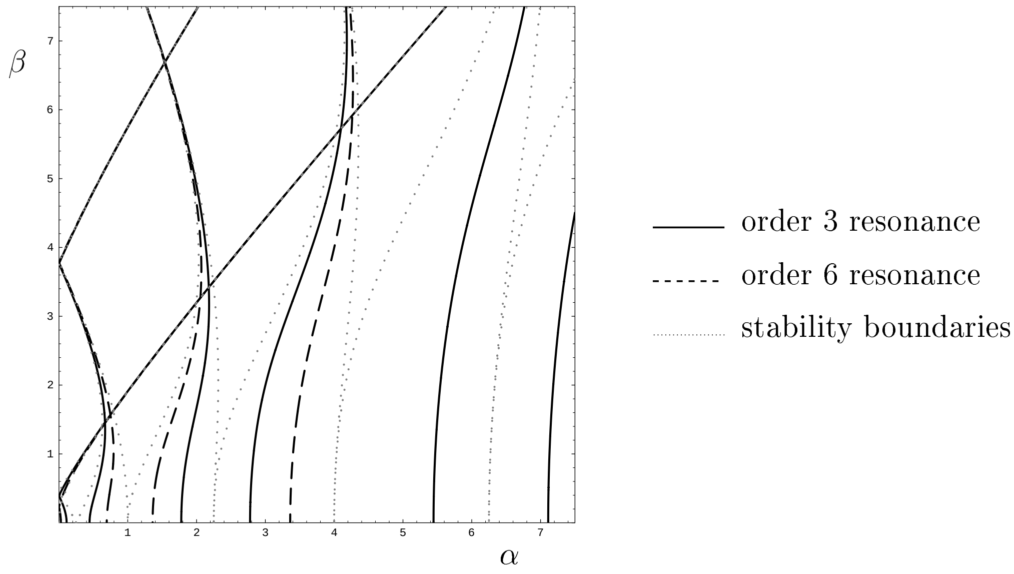

Figure 53: Diagram in the parameter plane showing curves of subharmonic bifurcation points, where period 3 or 6 points are created at the upper or lower equilibrium, as indicated. For clarity the stability boundaries of the equilibria are also indicated.

The first is at a Poincaré-Birkhoff bifurcation, cf. [Bir13, Bir25, BV92], where a resonant invariant circle of P breaks. This bifurcation takes place at the α-axis, where the map is integrable and hence has resonant invariant circles. For $\beta \neq 0$ these generically break into satellites, with transversally intersecting stable and unstable manifolds of the saddle points, as follows from a subharmonic Melnikov theorem, see e.g. Guckenheimer and Holmes [GH83] and Broer and Takens [BT89]. On the α axis the lower equilibrium is surrounded by a region of invariant circles, bounded by the separatrices. At a point $\alpha = \alpha_0$ on the α-axis the range of rotation numbers of these invariant circles is $(0, \sqrt{\alpha_0})$. Thus if β is increased from this point we only expect $p : q$ resonance bifurcations with $p/q < \alpha_0^2$.

The second is at a resonance of a fixed or a periodic point. As the eigenvalues of the linearized Poincaré map at this point pass through a resonance, satellites are born there, see, e.g., Meyer [Mey70], Takens [Tak74b] and Duistermaat [Dui84], also compare Takens [Tak74a] and Arnol'd [Arn88, Arn94] for the dissipative case. For the lower equilibrium the $p : q$ resonance bifurcation takes place at a curve in the parameter plane that passes through the point $\alpha = (p/q)^2$ on the α axis. The resonance curves of the upper equilibrium are the images of those of the lower equilibrium under reflection in the β axis (like the stability curves, cf. section 2). At a $p : q$ resonance curve the eigenvalues of the linearized Poincaré map pass through $e^{(\pm 2\pi i p/q)}$, but stay on the unit circle since P is area preserving. Thus the fixed point can only be unstable *at* the resonance.

In figure 54 we sketch (for the lower equilibrium) where the two bifurcations take place in the case of the $1 : 3$ resonance, and also the corresponding phase portraits. The latter only give a *qualitative* description of the dynamics involved, whereas the real map P of course has no heteroclinic connections, etc. Moreover, the width of the 'annulus' of $p : q$ resonant dynamics is $O(\sqrt{\beta})$ as $\beta \to 0$, hence resonant dynamics are a small phenomenon, cf. Duistermaat [Dui84], Arnol'd [Arn93] and Wiggins [Wig90]. Finally, we observe that, due to the spatial and temporal symmetries S and R of P, at both resonance bifurcations two period 3 satellites are created simultaneously, leading to a total of 6 stable and 6 unstable periodic points.

Thus, if one starts for example at $(\alpha, \beta) = (1/4, 0)$, there is an invariant circle of rotation number $1/3$ around the lower equilibrium. When β is increased, say to $1/10$, this circle breaks into a string of islands. If we then go the left in the parameter plane until we hit the $1 : 3$ resonance curve, the radius of the broken invariant circle shrinks to zero, and at the resonance curve it vanishes at the equilibrium.

Figure 53 shows curves in the parameter plane where the linearized map has a resonance of order 3 or 6, as indicated. Curves passing through the α-axis correspond to resonances of the lower, the others to resonances of the upper equilibrium. The stability boundaries of the equilibria are displayed for clarity. Obviously the curves of resonance points have to lie in the stable regions of the parameter plane. They converge to the stability boundaries as β increases. An easy computation reveals that the resonance points of order k on the α-axis are given by

$$\alpha = \left(n + \frac{m}{k}\right)^2,$$

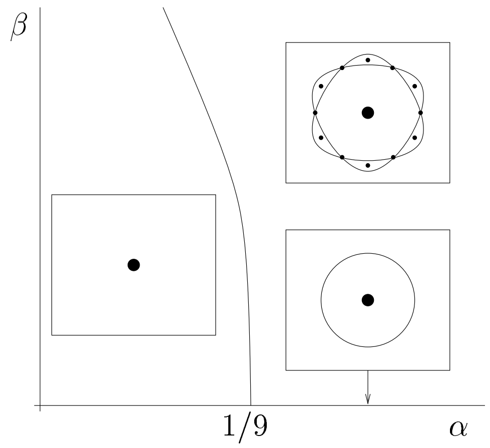

Figure 54: Sketch of the two types of 1 : 3 resonance bifurcations in the parameter plane, with phase portraits. For simplicity only the lower equilibrium and the 1 : 3 resonant dynamics are shown, for the regions to the left and right of the 1 : 3 resonance curve, and for the α-axis to the right of this curve. On the α axis (for $\alpha > 1/9$) a Poincaré-Birkhoff bifurcation takes place, and on the 1 : 3 resonance curve passing through $\alpha = 1/9$ the lower equilibrium goes through a 1 : 3 resonance bifurcation. Observe that there are two stable and two unstable period 3 orbits, due to the symmetries S and R.

with $m \in \{1, 2, \ldots, k-1\}$ relatively prime with k, and $n = 0, 1, \ldots$. Thus the resonance points of order 3 on the α-axis are given by

$$\alpha = \frac{1}{9}, \frac{4}{9}, \frac{16}{9}, \frac{25}{9}, \ldots,$$

and those of order 6 are given by

$$\alpha = \frac{1}{36}, \frac{25}{36}, \frac{49}{36}, \frac{121}{36}, \ldots,$$

as can be seen in the diagram.

Figure 55 displays a bifurcation diagram on the line $\alpha = 0.079$, showing four period 3 orbits, two stable and two unstable, branching off of the lower equilibrium in a subharmonic bifurcation. The satellites are born in a third order resonance at the lower equilibrium, at $\beta \approx 0.195$. Poincaré maps before and after the bifurcation are shown in figure 3 (the first two diagrams). The diagram at $\beta = 0.22$ clearly shows two stable period three orbits around the lower equilibrium. We remark that in the preceding sections satellites of other periods were encountered in several phase portraits, e.g., period 4 satellites around the upper equilibrium in diagram 2 in figure 35 and diagram 7 in figure 36.

Remark 21 : The p:q subharmonic bifurcations of the forced pendulum take place in a Hamiltonian equivariant context with a discrete $\mathbb{Z}_2 \times \mathbb{Z}_2$ symmetry group,

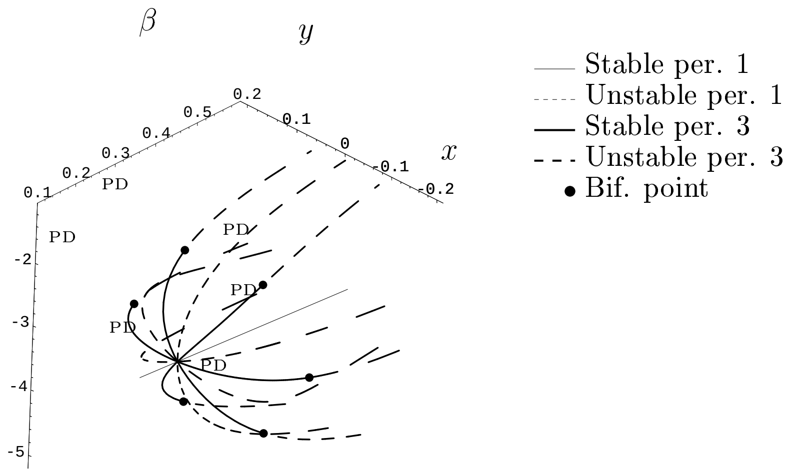

Figure 55: Bifurcation diagram on the line $\alpha = 0.079$ of the stable and unstable period three orbits (four in total) that are created in a bifurcation at the lower equilibrium point at $\beta \approx 0.195$. All orbits are created at the same bifurcation point due to symmetries. The stable periodic points undergo a period doubling bifurcation.

generated by the symmetries S and R. A complete analysis of the $p : q$ resonance in this setting requires an equivariant version of the subharmonic bifurcation theory developed by [Mey70, Tak74b, Dui84]. As far as we know no systematic study of these equivariant resonance bifurcations is available at this moment. However, for partial results in this direction, see [BLV98, BHLV98, Lun99].

Remark 22 : In case the twist condition is violated at a stable fixed point, another bifurcation scenario is possible, leading to 'meandering' invariant circles. We do not discuss this matter here, but refer for more details to [Sim98, DMS00].

4.5 The extended stability diagram

In the previous subsection we studied several bifurcations of saddle-center, pitchfork and period doubling type. They are all codimension one bifurcations, and hence take place on curves in the parameter plane. (For the bifurcations of the upper and lower equilibrium these are just the stability boundaries shown, e.g., in figure 5.) The curves are computed numerically using a continuation method, summarized in figure 56. It contains the following curves of bifurcation points:

- pitchfork and period doubling bifurcations of the equilibria, and bifurcations of the same type on the primary branches of the equilibria. For the lower equilibrium, we consider two secondary bifurcations, namely the pitchfork on the primary branch coming from the leftmost stability boundary, and the period doubling on the branch born at the third boundary from the left, compare the

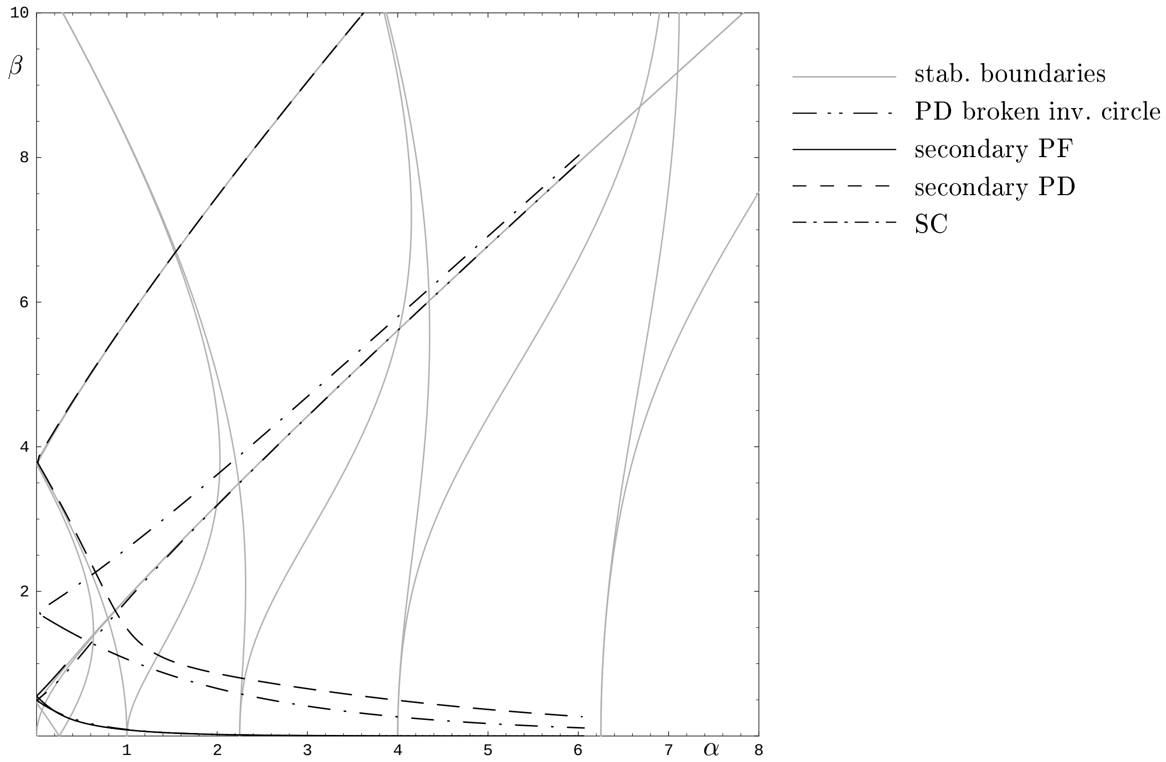

Figure 56: Curves of codimension one bifurcations in the parameter plane. The curves correspond to stability changes of the equilibria, a period doubling bifurcation of a broken invariant circle, bifurcations on the primary branches, and a saddle-center bifurcation,as indicated. See section 4.5 for more comments.

sketch in figure 41. The corresponding bifurcations are displayed for the upper equilibrium, namely the pitchfork and period doubling points on the second and fourth primary branches from below, respectively. See section 4.4.1 for details on these bifurcations.

- saddle-center bifurcations corresponding to the large stable regions on the x-axis (and smaller ones above and below the lower equilibrium), discussed in section 4.4.2. Curves of the pitchfork bifurcations on the stable and unstable branches of the saddle-center are not computed.

- period doubling bifurcations of the stable fixed point coming from the broken invariant circle with rotation number 1 (i.e., the 1:1 torus of the corresponding vector field), cf. section 4.4.3.

Curves of subharmonic bifurcations are shown in figure 53, and are omitted in the present diagram for clarity. Like the stability diagram, figure 56 is symmetric in both coordinate axes because of the symmetries T and U of P, and therefore only the first quadrant $\alpha, \beta \geq 0$ is displayed. As α increases, all curves seem to tend either to a stability boundary of the upper equilibrium, or to the α-axis.

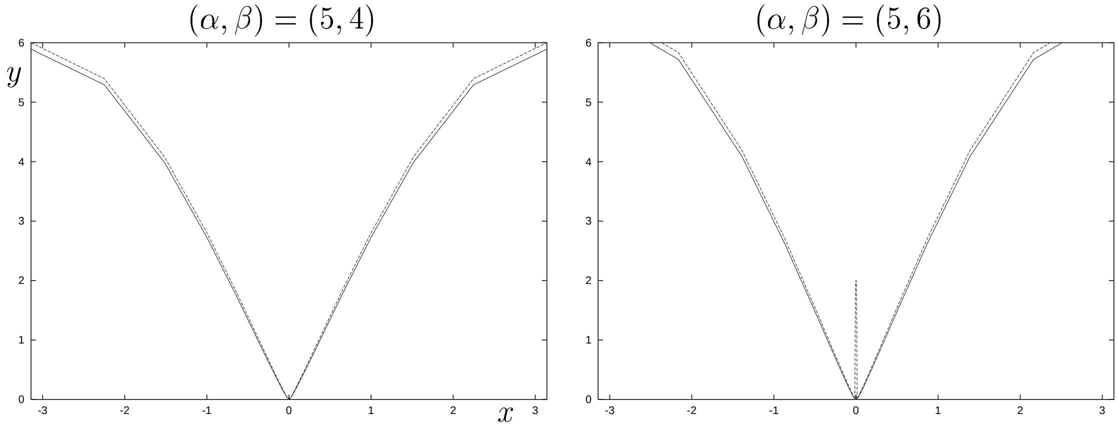

Figure 57: Comparison of a periodic orbit $(t, x(t), y(t))$ resulting from the broken 1:1 torus of the vector field (drawn line) with the frozen separatrix (dashed line), at $(\alpha, \beta) = (5, 4)$ (left diagram) and $(\alpha, \beta) = (5, 6)$ (right). The orbit is projected on the (x, y)-plane. The frozen separatrix is a two-dimensional manifold, introduced in section 3.3, and we plot the submanifold given by $x = x(t)$. The diagrams clearly illustrate that the orbit is close to the frozen separatrix, except near the upper equilibrium for $\beta > \alpha$.

Remark 23 : The symmetries T and U not only involve reflections and rotations in the parameter plane but also a transformation in phase space. Hence a bifurcation curve and its reflection in the β axis correspond to bifurcations at different locations in phase space. This is clearly illustrated in section 4.4.2, where it is shown that a saddle-center bifurcation on the lower branch of the bifurcation curve takes place at the x-axis, while on the upper part it takes place at the line $x = \pi$, see figures 45, 47, and 48.

We observe that the bifurcation curves seem to converge to the stability boundaries of the upper equilibrium as α and β go to infinity. It is remarkable that this is even true for bifurcations that are not related to this equilibrium (for example, the saddle-center bifurcations mentioned above). As far as we know, there is up to now no explanation for this. A possible approach, that we intend to take in future research, is to study the so-called separatrix map, cf. Simó and Treschev [STb], that describes the dynamics in a neighborhood of the frozen separatrix of the pendulum system in a suitable rescaling, cf. section 3.3. Some numerical evidence that the bifurcations we consider are described by this map is given in figure 57. The same approach can be useful to prove the regularity seen in the 'lobster' diagrams in figures 4 and 30 – 32.

A A normal form computation

In section 3.4 we observed that, for any parameter point, the 'lowest' invariant curve attains its maximal y-value at $x = \pi$, except for a small region near the origin, where this maximum is reached at $x = 0$. In this appendix we prove a normal form theorem, to show that the lower boundary of this region satisfies $\alpha = \frac{1}{2}\beta^3 + O(\beta^4)$. The normal form procedure is standard, except that

- it starts with a transformation that is not near the identity, and that is used to obtain a suitable perturbation problem.

- the effect of the transformations is duely recorded, to enable a quantitative analysis of the original system, using the normal form.

The numerical study of section 3.4 showed that along the lower boundary $\alpha = \frac{1}{2}\beta^3 + O(\beta^4)$ the maximal y-value of the 'lowest' invariant curve is given by $y = \frac{1}{2}\sqrt{2}\beta + O(\beta^2)$. We first perform a rescaling of the vector field of the forced pendulum reflecting the numerical data.

As before, the vector field of the forced pendulum is given by

$$X(x, y, t; \alpha, \beta) = \frac{\partial}{\partial t} + y\frac{\partial}{\partial x} + (\alpha + \beta \cos t) \sin x.$$

Let $y = \beta\tilde{y}$ and $\alpha = c\beta^3$, then the rescaling $(x, y, t; \alpha, \beta) \mapsto (x, \tilde{y}, t; c, \beta)$ takes X to the form (dropping the tildes)

$$X(x, y, t; c, \beta) = \frac{\partial}{\partial t} + \beta y\frac{\partial}{\partial x} + (c\beta^2 + \cos t) \sin x,$$

where β is a small parameter. In the rescaled setting, y and c are of order 1 in β. We observe that this vector field is again Hamiltonian.

Theorem 24 *Let X be the rescaled system defined above. Then, for β sufficiently small, there exists a symplectic, analytic transformation $\Psi : \mathbb{S}^1 \times \mathbb{R} \times \mathbb{S}^1 \longrightarrow \mathbb{S}^1 \times \mathbb{R} \times \mathbb{S}^1$, preserving t and the symmetries $\mathcal{S}$ and $\mathcal{R}$, such that*

$$\Psi_* X = \frac{\partial}{\partial t} + \beta y \frac{\partial}{\partial x} + \left(-\frac{1}{4}\beta \sin 2x + c\beta^2 \sin x \right) \frac{\partial}{\partial y} + O(\beta^3).$$

Moreover, on the section $t = 0$, Ψ leaves the lines $x = 0$ and $x = \pi$ invariant, and maps y to $y - \beta y \cos x + O(\beta^2)$.

The section $t = 0$ is important, because the Poincaré map is defined there. The t-dependence of the transformed system is pushed to the higher order terms by normal form (or averaging) transformations. We first discuss the consequences of the theorem, and sketch the proof afterwards.

Recall that we want to find the curve where the y-coordinates of the 'lowest' invariant circle at $x = 0$ and $x = \pi$ (and in the section $t = 0$) are equal. We call these y-coordinates $\tilde{y}_0$ and $\tilde{y}_\pi$, respectively. According to the theorem, the corresponding y-coordinates y_0 and y_π in the transformed setting satisfy:

$$y_0 = (1 - \beta)\tilde{y}_0 + O(\beta^2) \text{ , and } y_\pi = (1 + \beta)\tilde{y}_\pi + O(\beta^2). \tag{7}$$

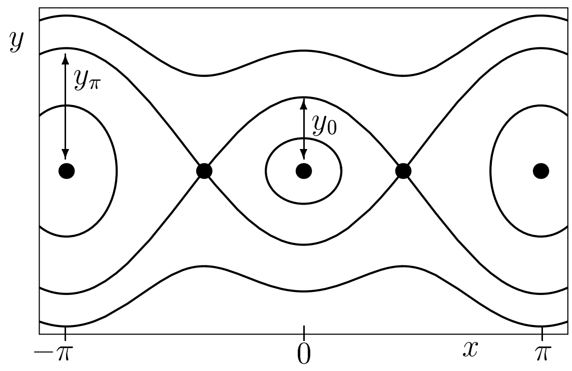

Figure 58: Sketch of the level sets of the Hamiltonian $H(x, y, t; c, \beta) = \frac{1}{2}\beta y^2 - \frac{1}{8}\beta \cos 2x + c\beta^2 \cos x$, for $\beta > 0$ and small, and $c > \frac{1}{2}$. Up to an $O(\beta^3)$ remainder, this is the Hamiltonian of the transformed system of theorem 24.

Let us consider the dynamics of the transformed system. It is Hamiltonian, with Hamilton function

$$H(x, y, t; c, \beta) = \frac{1}{2}\beta y^2 - \frac{1}{8}\beta \cos 2x + c\beta^2 \cos x + O(\beta^3).$$

It has four singularities, at $x = 0$, $x = \pi$ and $x \approx \pm\frac{1}{2}\pi$, all on the x axis, compare figure 58. The 'lowest' invariant circle of this system is arbitrarily close to the separatrix connecting the last two singularities. Therefore y_0 and y_π equal the y-coordinates of the separatrix at $x = 0$ and $x = \pi$, respectively. A brief calculation yields that the two singularities on the separatrix are given by

$$\frac{1}{2}\cos x + c\beta = O(\beta^2) \text{ , that is, } x = \pm(\frac{1}{2}\pi + 2c\beta + O(\beta^2)),$$

and hence the Hamiltonian on the separatrix equals

$$H = h := \frac{1}{8}\beta + O(\beta^3).$$

Using $H(0, y_0) = h$, $H(\pi, y_\pi) = h$, and (7), this yields the following equations for $\tilde{y}_0$ and $\tilde{y}_\pi$:

$$\begin{aligned} \frac{1}{2}\tilde{y}_0^2 - \frac{1}{4} + \beta\left(-\tilde{y}_0^2 + c\right) + O(\beta^2) &= 0, \\ \frac{1}{2}\tilde{y}_\pi^2 - \frac{1}{4} + \beta\left(\tilde{y}_\pi^2 - c\right) + O(\beta^2) &= 0. \end{aligned}$$

Letting $\tilde{y}_0 = \tilde{y}_\pi$, this finally implies that

$$\begin{aligned} \tilde{y}_0 &= \frac{1}{2}\sqrt{2} + O(\beta), \\ \tilde{y}_\pi &= \frac{1}{2}\sqrt{2} + O(\beta), \\ c &= \frac{1}{2} + O(\beta), \end{aligned}$$

in good agreement with the numerical results.

We conclude this appendix by sketching a proof of theorem 24. First let us introduce an action variable J conjugate to the angle t, turning the rescaled vector field X, defined above, into a two degree of freedom autonomous Hamiltonian system. given by the Hamilton function

$$H(x, y, t, J; c, \beta) = J + \cos t \cos x + \frac{1}{2}\beta y^2 + c\beta^2 \cos x.$$

To obtain a system suitable for averaging, we now remove the term $\cos t \cos x$, transforming H by the time one flow G_1^1 of a Hamiltonian vector field with Hamilton function

$$G_1 = -\cos x \sin t.$$

Since G_1 is independent of the actions y and J, this transformation is invertible. In fact,

$$G_1^1 : (x, y, t, J) \mapsto (x, y - \sin x \sin t, t, J + \cos x \cos t).$$

We observe that on the section $t = 0$ this transformation does not change x or y. A straightforward calculation, using Poisson brackets, or applying G_1^1 directly, yields

$$G_1^1{}_* H = H \circ G_1^{-1} = J + \frac{1}{2}\beta y^2 + \beta(y \sin x \sin t + \frac{1}{2}\sin^2 x \sin^2 t) + c\beta^2 \cos x.$$

The resulting Hamiltonian can be seen as a small perturbation of the Hamiltonian J, and hence it can be averaged with respect to t. After two averaging steps, where the transformations are duely tracked, we obtain the theorem.

B Numerical computation of the 'lowest' invariant circle

This appendix describes the numerical method to compute the location of the 'lowest' invariant circle, used in subsection 3.4. This location is computed at grid points in the parameter plane. In fact, we compute the intersection of the 'lowest' invariant circle with the line $x = 0$, since the islands in between the circles are much larger there than at $x = \pi$. At each parameter point we start with an estimate for y which is below the location of the 'lowest' invariant circle, e.g., $y = 0$. We then increase y with a fixed increment until an invariant circle is obtained. Then the step is refined to improve the estimate. We start with a step size between 10^{-4} and 10^{-3}, depending on the parameter point, and refine each time by a factor of 10 until the step size is 10^{-6}.

At each y, we compute 2500 iterates of the corresponding orbit of P, and supplement them with their symmetric counterparts (under the reversible symmetry $SR : (x, y) \mapsto (-x, y)$) to get a total of 5000 points. The x-coordinates of the corresponding orbit of the lift of P on $\{(x, y)\} = \mathbb{R} \times \mathbb{R}$ are also computed. Further, to estimate the Lyapunov exponent, the orbit of a random vector under the map DP is tracked. Each time that the next iterate is computed, the following tests are performed to check whether the orbit is an invariant circle:

- If the y-coordinate is negative, the orbit is definitely not an invariant circle (of rotational type), and hence is discarded.
- If the norm of the transported random vector is larger than some given value (typically of the order 10^6), the orbit is considered chaotic, so it is discarded.
- If the maximal difference between x-coordinates of successive points on the lift is more than 2π larger than the minimal difference, the orbit can not be an invariant circle, and is discarded.

If the orbit is discarded, we increase y and try the next orbit. Otherwise, at each tenth iterate the orbit points are sorted by their x-coordinate and the following tests are done:

- The orbit is discarded if its slope is larger than a given value, depending on the parameters. For this value we take $2\sqrt{\alpha + \beta}$ (this is twice the maximal slope of the 'frozen' separatrix, compare section 3.2). The slope is estimated by the difference of neighboring points, and this test is only done for x close to zero (we take $|x| < 0.1$), where the slope of the invariant circles is large.
- If the ordering of the points in the sorted list is not invariant under the map P, the orbit is discarded. This means the following. Let $z_0, z_1, \ldots, z_n$ be the unsorted finite orbit, with $z_j = (x_j, y_j)$, and $z_j = P^j(z_0)$. Suppose that z_k and z_{k+m}, for some $k, k + m \in \{0, 1, \ldots, n\}$, are two consecutive points in the sorted list. If the orbit corresponds to an invariant circle, then the map P^m

maps the part of the curve between z_k and z_{k+m} to the part between z_{k+m} and z_{k+2m}. Hence the next point in the ordered list has to be z_{k+2m}, except in the case that $k+2m$ falls outside the range $0, 1, \ldots, n$, or there is a point between z_{k+m} and z_{k+2m} whose pre-image under P^m falls outside the range. If the orbit is not an invariant circle, but for example chaotic, then the ordering is generically not preserved.

- We compute an upper and lower bound on the rotation number. If the lower bound is larger than the upper bound, the orbit is discarded. The bounds are computed as follows. Using the notation of the previous test, let n_k be the number of 'turns' around the cylinder of the map P between z_0 and z_k (i.e., n_k is the number of times that $x_{j+1} < x_j$ for $0 \leq j < k$). Let z_k and z_{k+m} be two consecutive points in the sorted list, with $x_k < x_{k+m}$. If $m > 0$, then the rotation number is at least $\frac{n_{k+m}-n_k}{m}$. Otherwise, it is at most $\frac{n_{k+m}-n_k}{m}$.

Again, if the orbit is discarded, we proceed with the next y. Otherwise it is accepted as an invariant circle, and the estimate for y is refined as described above. To obtain an estimate for the corresponding y-value at $x = \pi$ (this is the desired location of the 'lowest' invariant circle), we take the 20 points on the orbit nearest to $x = \pi$, and fit a parabola through them. A numerical test, recomputing the orbit with many more points (e.g., 10000), shows that this is a good approximation of the desired value, with an error of at most 10^{-6}.

C Numerical integration by the Taylor series method.

In this appendix we discuss the numerical integrator used to compute phase portraits and bifurcation and stability diagrams, called the Taylor series method, compare, e.g., [BWZ71, BS98, JZ]. For phase portraits one simply needs to compute the Poincaré map P. Stability and bifurcation diagrams are obtained by numerical continuation, which also requires the first and (at bifurcation points) second variationals of P. We concentrate here on integration of P only; the variationals can be treated similarly.

Let us first explain why we use the Taylor series method. For long time integrations of a Hamiltonian vector field, a symplectic method is more efficient than a non-symplectic one, in terms of required CPU time for a given *global* error tolerance, because its propagated error grows linear with the integration time, compared to quadratic growth for non-symplectic methods, see [CSS93, CSS97, SS92b, SSC94]. Although formally the Taylor series method is non-symplectic, numerical experiments show that it preserves the symplectic form very well, because of its large time step, compared with a high order approximation of the orbit. Moreover, the integrator preserves the equivariant and reversible symmetries $\mathcal{S}$, $\mathcal{R}$, $\mathcal{T}$ and $\mathcal{U}$ of the forced pendulum. For more background on symplectic and non-symplectic integrators we refer to [CSS92, HNW93, MQR99, SS92a, Ske99].

We first describe the Taylor series method. As before, let the vector field X of the forced pendulum be given by the differential equations

$$\begin{aligned} \dot{x} &= y \\ \dot{y} &= -\left(\alpha + \beta\rho(t)\right) V'(x) \\ \dot{t} &= 1, \end{aligned} \tag{8}$$

where $\rho(t) = \cos t$ and $V(x) = \cos x - 1$. Let $(x(t), y(t), t)$ be a solution of this system, depending on the parameters α, β, with initial condition $(x(t_0), y(t_0)) = (x_0, y_0)$. Since $x(t)$ and $y(t)$ are analytic functions of t, they satisfy

$$(x(t+h), y(t+h)) = \sum_{k\geq 0} \frac{h^k}{k!} \left(\frac{\partial}{\partial t}\right)^k (x(t), y(t)), \tag{9}$$

for $|h|$ sufficiently small. The Taylor series method approximates $x(t+h)$ and $y(t+h)$ by $\hat{x}(t+h)$ and $\hat{y}(t+h)$, given by

$$\hat{x}(t+h) = \sum_{k=0}^{N} \hat{x}_k h^k, \ \hat{y}(t+h) \text{ analogous}, \tag{10}$$

for some $N \in \mathbb{N}$, and

$$\hat{x}_k = \frac{1}{k!} \left(\frac{\partial}{\partial t}\right)^k \hat{x}(t).$$

Here the dependence of $\hat{x}_k$ (and $\hat{y}_k$) on t is suppressed. Given $\hat{x}$ and $\hat{y}$, all coefficients $\hat{x}_k$ and $\hat{y}_k$ can be computed using the differential equations (8).

Remark 25 : The coefficients $\hat{x}_k$ and $\hat{y}_k$ are efficiently computed by recursion. Abbreviate $q(t) = \alpha + \beta \cos t$, $u(\hat{x}(t)) = \sin(\hat{x}(t))$ and $v(\hat{x}(t)) = \cos(\hat{x}(t))$, and define q_k, u_k and v_k analogous to $\hat{x}_k$. Then $\hat{x}_0 = x(t)$, $\hat{y}_0 = y(t)$, and for $k > 0$, by (8) and Leibniz' rule

$$\begin{aligned} \hat{x}_k &= \frac{1}{k}\hat{y}_{k-1} \\ \hat{y}_k &= \frac{1}{k}\sum_{j=0}^{k-1} q_j u_{k-1-j}. \end{aligned}$$

The coefficients q_k and u_k are computed recursively. Indeed, $u_0 = \sin(\hat{x}(t))$, $v_0 = \cos(\hat{x}(t))$, and for $k > 0$, again using Leibniz' rule

$$\begin{aligned} u_k &= \sum_{j=1}^{k} \frac{j}{k} v_{k-j}\hat{x}_j \\ v_k &= -\sum_{j=1}^{k} \frac{j}{k} u_{k-j}\hat{x}_j. \end{aligned}$$

Thus each integration step only requires four trigonometric evaluations.

The local (truncation) error ε in $(\hat{x}(t+h), \hat{y}(t+h))$ is defined by $\varepsilon = ||(x(t+h), y(t+h)) - (\hat{x}(t+h), \hat{y}(t+h))||$, assuming that $(x(t), y(t)) = (\hat{x}(t), \hat{y}(t))$. Let R be the radius of convergence of (9), then

$$||(\hat{x}_k, \hat{y}_k)|| \approx AR^{-k} \text{ for } k \text{ sufficiently large, and some constant } A > 0.$$

Hence the truncation error is given by

$$\varepsilon \approx \sum_{k>N} A \left(\frac{h}{R}\right)^k \approx ||(\hat{x}_{N+1}, \hat{y}_{N+1})|| h^{N+1} \frac{1}{1 - h/R},$$

and for small h/R we can approximate

$$\varepsilon \approx ||(\hat{x}_{N+1}, \hat{y}_{N+1})|| h^{N+1}.$$

For given step size h and error tolerance ε this determines an optimal choice for N, namely N is the smallest integer for which $||(\hat{x}_k, \hat{y}_k)|| h^k < \varepsilon$ holds for all $k > N$.

Taking $h = 2\pi/M$ for some $M \in \mathbb{N}$, an approximation $\hat{P}$ to the Poincaré map P is obtained by applying the above algorithm M times to a given point (x_0, y_0). This yields an approximation (x_1, y_1) to $P(x_0, y_0)$. Since the local error in the integrator is of order h^{N+1}, and the number of integration steps in one period is of order $1/h$, the symplectic form satisfies

$$\mathrm{d}x_1 \wedge \mathrm{d}y_1 - \mathrm{d}x_0 \wedge \mathrm{d}y_0 = O(h^N).$$

We define the error ε_k in the symplectic form after k iterates by

$$\mathrm{d}x_k \wedge \mathrm{d}y_k = (1 + \varepsilon_k)\mathrm{d}x_0 \wedge \mathrm{d}y_0,$$

where (x_k, y_k) is the numerical approximation to the k-th iterate of (x_0, y_0). We note that $1 + \varepsilon_k$ is the determinant of $D(\hat{P}^k)$.

Table 2 shows the results of a few numerical experiments with this integrator. In each experiment, we computed 10000 iterates (x_k, y_k), $k = 0, \ldots, 10000$ of the chaotic orbit of P starting at $(x, y) = (0, 0.1)$. The experiments were done using a Pentium II 400 MHz with Debian Linux 2.2.17. The integrator was written in C++, and compiled using g++ –O (version 2.95.2). The table shows for several parameter points the speed of the integrator and the error $|\varepsilon_k|$ in the symplectic form after $k = 2000, 4000, 6000, 8000, 10000$ iterates. To compute the error ε_k, we calculated the determinant of $D(\hat{P}^k)$ by integrating the variational equations with the Taylor series method. We conclude that even at high parameter values the integrator achieves a reasonable speed, and preserves the symplectic form for a large number of iterates.

D Proof of lemma 19

In this appendix we prove lemma 19. For convenience it is repeated here.

α	β	speed	$\lvert\varepsilon_{2000}\rvert$	$\lvert\varepsilon_{4000}\rvert$	$\lvert\varepsilon_{6000}\rvert$	$\lvert\varepsilon_{8000}\rvert$	$\lvert\varepsilon_{10000}\rvert$
0.5	1.0	1830	$3 \cdot 10^{-11}$	$6 \cdot 10^{-11}$	$5 \cdot 10^{-11}$	$4 \cdot 10^{-11}$	$1 \cdot 10^{-11}$
5	10	650	$8 \cdot 10^{-8}$	$8 \cdot 10^{-8}$	$2 \cdot 10^{-6}$	$2 \cdot 10^{-6}$	$2 \cdot 10^{-6}$
50	100	210	$3 \cdot 10^{-5}$	$1 \cdot 10^{-6}$	$3 \cdot 10^{-4}$	$3 \cdot 10^{-4}$	$1 \cdot 10^{-3}$

Table 2: Speed and symplecticness of the Taylor integrator, tested at several parameter points, by computing 10000 iterates of the chaotic orbit starting at $(x, y) = (0, 0.1)$. The speed is measured in iterates per second, and the error ε_k in the symplectic form is computed after $k = 2000, 4000, 6000, 8000, 10000$ iterates.

Lemma 26 *The eigenvalues of the linearized Poincaré map at the upper or lower equilibrium are ± 1 on curves in the parameter plane of the form*

$$\mathbb{R} \ni \beta \mapsto (\alpha, \beta) = (f(\beta), \beta) \in \mathbb{R}^2,$$

for some smooth function f. At these curves the stability of the equilibrium changes.

The linearized Poincaré map at the upper or lower equilibrium corresponds to the 2π-flow of the linearized vector field

$$DX = y\frac{\partial}{\partial x} + (\alpha + \beta\rho(t))x\frac{\partial}{\partial y} + \frac{\partial}{\partial t},$$

where $\rho(t) = \cos t$. It needs to be shown that the eigenvalues of the linearized map are ± 1 on curves in the parameter plane that can be represented as graphs over β. We shall prove this for the more general case that ρ is a 2π-periodic, even function.

In short, the proof runs as follows. Each stability curve is given by an implicit equation of the form $g(\alpha, \beta) = 0$. We show that $\frac{\partial}{\partial \alpha} g(\alpha, \beta) \neq 0$ at any zero (α, β) of g. Hence the implicit function theorem implies that at *any* point (α, β) on the stability curve, this curve can locally be seen as a graph over β. Hence the graph can not have 'endpoints', and the stability curve is a graph over β defined on the whole of $\mathbb{R}$, as needs to be shown.

Let us first drive the implicit equation $g(\alpha, \beta) = 0$. In general, the linearized Poincaré map $DP = DP(\alpha, \beta)$ is given by

$$DP = \begin{pmatrix} a(\alpha, \beta) & b(\alpha, \beta) \\ c(\alpha, \beta) & d(\alpha, \beta) \end{pmatrix},$$

where $ad - bc = 1$, because the map is area-preserving. Since the function ρ is even, the maps P and DP are R-reversible, for the temporal symmetry $R : (x, y) \mapsto (x, -y)$ defined in section 2. A brief calculation shows that for the linear map DP this means

$$a(\alpha, \beta) \equiv d(\alpha, \beta).$$

At the stability curves the eigenvalues of DP are both $+1$ or both -1, and hence the trace $a + d$ equals $+2$ or -2. Together with $a = d$ and $ad - bc = 1$ this means that $b = 0$ or $c = 0$. Vice versa, if $b = 0$ or $c = 0$, then area-preservation and $a = d$ imply that the eigenvalues are ± 1. Thus we have proved the following.

Lemma 27 *Let the coefficients b and c of the linear Poincaré map DP be defined as above. Then the stability curves are given by the equations*

$$b(\alpha,\beta)=0, \text{ or } c(\alpha,\beta)=0.$$

Remark 28 : Each resonance point of the lower equilibrium on the α axis lies on two stability curves. One is given by $b=0$, the other by $c=0$.

Now let (α^*,β^*) be such that $c(\alpha^*,\beta^*)=0$. To prove that $\frac{\partial}{\partial\alpha}c(\alpha^*,\beta^*)\neq 0$ — the proof for b runs similar — we consider the integral curve $t\mapsto(x(t),y(t),t)$ of the linearized vector field with initial condition $(x(0),y(0))=(0,1)$. Evaluated at $t=2\pi$ this solution gives the second column of the matrix DP. Thus $x(2\pi)=c(\alpha^*,\beta^*)=0$ and $y(2\pi)=\pm 1$ equals the eigenvalues. Let $(u(t),v(t))=\frac{\partial}{\partial\alpha}(x(t),y(t))$, then $(u(0),v(0))=(0,0)$ and $t\mapsto(u(t),v(t),t)$ is an integral curve of the first variational of DX, given by

$$v\frac{\partial}{\partial u}+((\alpha^*+\beta^*\rho t)u+x(t))\frac{\partial}{\partial v}+\frac{\partial}{\partial t}.$$

It has to be shown that $u(2\pi)\neq 0$. The vector fields for (x,y) and (u,v) yield

$$x(t)\dot{v}(t)-u(t)\dot{y}(t)=x(t)^2.$$

Integrating this equation from $t=0$ to $t=2\pi$, using $\frac{\partial}{\partial t}(xv-uy)=x\dot{v}-u\dot{y}$ and the initial and final conditions $x(2\pi)=u(0)=v(0)=0$ and $y(2\pi)=\pm 1$, we obtain

$$\mp u(2\pi)=\int_0^{2\pi}x^2(t)\mathrm{d}t>0,$$

and hence $u(2\pi)\neq 0$, as needed.

Thus by the implicit function theorem, locally around any zero (α^*,β^*) of c there exists a curve of the form $\beta\mapsto(f(\beta),\beta)$, such that f is smooth, $f(\beta^*)=\alpha^*$, and $c(f(\beta),\beta)=0$ for $|\beta-\beta^*|$ sufficiently small. This local graph can be extended to all β. Indeed, suppose that I is the largest interval containing β^* on which the stability curve can be defined as a graph over β. Then I is open since at any point of I the 'local graph' construction can be done. Furthermore, I is closed because of continuity of c. Thus $I=\mathbb{R}$, and lemma 19 is proved.

References

[AA68] V.I. Arnol'd and A. Avez. *Ergodic problems of classical mechanics.* Mathematical physics monograph series. W.A. Benjamin, 1968.

[Ach95] D. Acheson. Multiple-nodding oscillations of a driven inverted pendulum. *Proc. Royal Soc. London A*, 448:89 – 95, 1995.

[AM78] R. Abraham and J.E. Marsden. *Foundations of mechanics.* The Benjamin/Cummings publishing company, second edition, 1978.

[Arn62] V.I. Arnol'd. On the behavior of an adiabatic invariant under slow periodic variation of the Hamiltonian. *Soviet Math. Dokl.*, 3:136 – 140, 1962.

[Arn63] V.I. Arnol'd. Proof of a theorem of A.N. Kolmogorov on the preservation of conditionally periodic motions under a small perturbation of the Hamiltonian (in Russian). *Russian Math. Surveys*, 18(5):9 – 36, 1963.

[Arn88] V.I. Arnol'd. *Geometrical methods in the theory of ordinary differential equations.* Springer-Verlag, second edition, 1988.

[Arn89] V.I. Arnol'd. *Mathematical methods of classical mechanics*, volume 60 of *Graduate Texts in Mathematics.* Springer-Verlag, second edition, 1989.

[Arn93] V.I. Arnol'd, editor. *Dynamical systems. III.* Springer-Verlag, 1993. Mathematical aspects of classical and celestial mechanics, Translation of *Current problems in mathematics. Fundamental directions, Vol. 3* (Russian), Akad. Nauk SSSR, Vsesoyuz. Inst. Nauchn. i Tekhn. Inform., Moscow, 1985, Translation by A. Iacob.

[Arn94] V.I. Arnol'd, editor. *Dynamical systems. V.* Springer-Verlag, 1994. Bifurcation theory and catastrophe theory, Translation of *Current problems in mathematics. Fundamental directions. Vol. 5 (Russian)*, Akad. Nauk SSSR, Vsesoyuz. Inst. Nauchn. i Tekhn. Inform., Moscow, 1986, Translation by N. D. Kazarinoff.

[BC91] M. Benedicks and L. Carleson. The dynamics of the Hénon map. *Ann. of Math. (2)*, 133(1):73 – 169, 1991.

[Ben88] G. Benettin. Nekhoroshev-like results for Hamiltonian dynamical systems. In *Nonlinear evolution and chaotic phenomena (Noto, 1987)*, pages 121–146. Plenum, New York, 1988.

[BGM+92] A. Back, J. Guckenheimer, M.R. Myers, F.J. Wicklin, and P.A. Worfolk. Dstool: Computer assisted exploration of dynamical systems. *Notices Amer. Math. Soc.*, 39:303 – 309, 1992.

[BHLV98] H.W. Broer, I. Hoveijn, G.A. Lunter, and G. Vegter. Resonances in a spring-pendulum: algorithms for equivariant singularity theory. *Nonlinearity*, 11(6):1569 – 1605, 1998.

[BHN98] H.W. Broer, I. Hoveijn, and M. van Noort. A reversible bifurcation analysis of the inverted pendulum. *Phys. D*, 112(1 – 2):50 – 63, 1998. Time-reversal symmetry in dynamical systems (Warwick, 1996).

[BHNV99] H.W. Broer, I. Hoveijn, M. van Noort, and G. Vegter. The inverted pendulum: a singularity theory approach. *J. Diff. Eq.*, 157:120 – 149, 1999.

[BHS96] H.W. Broer, G.B. Huitema, and M.B. Sevryuk. *Quasi-periodic motions in families of dynamical systems. Order amidst chaos*, volume 1645 of *Lecture Notes in Mathematics*. Springer-Verlag, 1996.

[BHT90] H.W. Broer, G.B. Huitema, and F. Takens. Unfoldings of quasi-periodic tori. *Mem. Amer. Math. Soc.*, 83(421):1 – 81, 1990.

[Bir13] G.D. Birkhoff. Proof of Poincaré's geometric theorem. *Trans. Am. Math. Soc.*, 14(1):14 – 22, 1913.

[Bir25] G.D. Birkhoff. An extension of Poincaré's last geometric theorem. *Acta Math.*, 47:297 – 311, 1925.

[BL95] H.W. Broer and M. Levi. Geometrical aspects of stability theory for Hill's equations. *Arch. Rational Mech. Anal.*, 131(3):225 – 240, 1995.

[BLS] H.W. Broer, M. Levi, and C. Simó. In preparation.

[BLV98] H.W. Broer, G.A. Lunter, and G. Vegter. Equivariant singularity theory with distinguished parameters. Two case studies of resonant Hamiltonian systems. *Phys. D*, 112(1 – 2):64 – 80, 1998. Time-reversal symmetry in dynamical systems (Warwick, 1996).

[BNS] H.W. Broer, M. van Noort, and C. Simó. In preparation.

[BR01] H.W. Broer and R. Roussarie. Exponential confinement of chaos in the bifurcation sets of real analytic diffeomorphisms. In H.W. Broer, B. Krauskopf, and G. Vegter, editors, *Global analysis of dynamical systems – Festschrift dedicated to Floris Takens for his 60th birthday.* ?, 2001.

[BRS96] H.W. Broer, R. Roussarie, and C. Simó. Invariant circles in the Bogdanov-Takens bifurcation for diffeomorphisms. *Ergodic Theory Dynam. Systems*, 16(6):1147 – 1172, 1996.

[BS98] H.W. Broer and C. Simó. Hill's equation with quasi-periodic forcing: resonance tongues, instability pockets and global phenomena. *Bol. Soc. Brasil. Mat. (N.S.)*, 29(2):253 – 293, 1998.

[BS00] H.W. Broer and C. Simó. Resonance tongues in Hill's equation: a geometric approach. *J. Diff. Eq.*, 166(2):290 – 327, 2000.

[BST98] H.W. Broer, C. Simó, and J.C. Tatjer. Towards global models near homoclinic tangencies of dissipative diffeomorphisms. *Nonlinearity*, 11(3):667 – 770, 1998.

[BT89] H.W. Broer and F. Takens. Formally symmetric normal forms and genericity. *Dynam. Report.*, 2:39 – 59, 1989.

[BV92] H.W. Broer and G. Vegter. Bifurcational aspects of parametric resonance. *Dynam. Report. (N.S.)*, 1:1 – 53, 1992.

[BWZ71] D. Barton, I.M. Willers, and R.V.M. Zahar. Taylor series methods for ordinary differential equations – an evaluation. In J.R. Rice, editor, *Mathematical software. Proceedings of the Mathematical Software Symposium, Purdue University, Lafayette, Indiana 1970, April 1–3, 1970*, ACM Monograph Series, pages 369 – 390, 1971.

[BY93] M. Benedicks and L.S. Young. Sinaĭ-Bowen-Ruelle measures for certain Hénon maps. *Invent. Math.*, 112(3):541 – 576, 1993.

[CC88a] A. Celletti and L. Chierchia. Construction of analytic KAM surfaces and effective stability bounds. *Comm. Math. Phys.*, 118(1):119 – 161, 1988.

[CC88b] A. Celletti and L. Chierchia. On rigorous stability results for low-dimensional KAM surfaces. *Phys. Lett. A*, 128(3–4):166–168, 1988.

[CC91] A. Celletti and L. Chierchia. Invariant curves for area-preserving twist maps far from integrable. *J. Stat. Phys.*, 65(3–4):617 – 643, 1991.

[CFP87] A. Celletti, C. Falcolini, and A. Porzio. Rigorous numerical stability estimates for the existence of KAM tori in a forced pendulum. *Ann. Inst. H. Poincaré Phys. Théor.*, 47(1):85–111, 1987.

[CGL00] A. Celletti, A. Giorgilli, and U. Locatelli. Improved estimates on the existence of invariant tori for Hamiltonian systems. *Nonlinearity*, 13(2):397–412, 2000.

[CJ00] E. Castellà and À. Jorba. On the vertical families of two-dimensional tori near the triangular points of the bicircular problem. *Celestial Mech. Dynam. Astronom.*, 76(1):35 – 54, 2000.

[CSS92] M.P. Calvo and J.M. Sanz-Serna. Variable steps for symplectic integrators. In *Numerical analysis 1991 (Dundee, 1991)*, volume 260 of *Pitman Res. Notes Math. Ser.*, pages 34–48. Longman Sci. Tech., Harlow, 1992.

[CSS93] M.P. Calvo and J.M. Sanz-Serna. Reasons for a failure. The integration of the two-body problem with a symplectic Runge-Kutta-Nyström code with stepchanging facilities. In *International Conference on Differential Equations, Vol. 1, 2 (Barcelona, 1991)*, pages 93–102. World Sci. Publishing, River Edge, NJ, 1993.

[CSS97] B. Cano and J.M. Sanz-Serna. Error growth in the numerical integration of periodic orbits, with application to Hamiltonian and reversible systems. *SIAM J. Numer. Anal.*, 34(4):1391–1417, 1997.

[CZ89] L. Chierchia and E. Zehnder. Asymptotic expansions of quasiperiodic solutions. *Ann. Scuola Norm. Sup. Pisa Cl. Sci. (4)*, 16(2):245–258, 1989.

[DG96] A. Delshams and P. Gutiérrez. Effective stability and KAM theory. *J. Diff. Eq.*, 128(2):415 – 490, 1996.

[DKK91a] E. Doedel, H.B. Keller, and J.-P. Kernévez. Numerical analysis and control of bifurcation problems. I. Bifurcation in finite dimensions. *Internat. J. Bifur. Chaos Appl. Sci. Engrg.*, 1(3):493 – 520, 1991.

[DKK91b] E. Doedel, H.B. Keller, and J.-P. Kernévez. Numerical analysis and control of bifurcation problems. II. Bifurcation in infinite dimensions. *Internat. J. Bifur. Chaos Appl. Sci. Engrg.*, 1(4):745 – 772, 1991.

[DMS00] H. R. Dullin, J. D. Meiss, and D. Sterling. Generic twistless bifurcations. *Nonlinearity*, 13(1):203–224, 2000.

[Dui84] J.J. Duistermaat. Bifurcation of periodic solutions near equilibrium points of Hamiltonian systems. In *Bifurcation theory and applications (Montecatini, 1983)*, volume 1057 of *Lecture Notes in Mathematics*, pages 57–105. Springer Verlag, 1984.

[EE91] Y. Elskens and D.F. Escande. Slowly pulsating separatrices sweep homoclinic tangles where islands must be small: an extension of classical adiabatic theory. *Nonlinearity*, 4(3):615 – 667, 1991.

[Fas90] F. Fassò. Lie series method for vector fields and Hamiltonian perturbation theory. *Z. Angew. Math. Phys.*, 41(6):843 – 864, 1990.

[GH83] J. Guckenheimer and P. Holmes. *Nonlinear oscillations, dynamical systems, and bifurcations of vector fields*, volume 42 of *Applied Mathematical Sciences*. Springer-Verlag, 1983.

[GLS97] A. Giorgilli, V.F. Lazutkin, and C. Simó. Visualization of a hyperbolic structure in area preserving maps. *Regular and Chaotic Dynamics*, 2(3 – 4):47 – 61, 1997. Correction in same journal, 3(2):115, 1998.

[GP81] J.M. Greene and I.C. Percival. Hamiltonian maps in the complex plane. *Phys. D*, 3(3):530–548, 1981.

[Hal63] J.K. Hale. *Oscillations in nonlinear systems.* McGraw-Hill, 1963. Republication: Dover publications, 1992.

[Hal69] J.K. Hale. *Ordinary differential equations.* Wiley-Interscience, 1969. Second edition: Krieger, 1980.

[HH64] M. Hénon and C. Heiles. The applicability of the third integral of motion; some numerical experiments. *Astronom. J.*, 69:73 – 79, 1964.

[HNW93] E. Hairer, S.P. Nørsett, and G. Wanner. *Solving ordinary differential equations I – Nonstiff problems*, volume 8 of *Springer series in Computational Mathematics.* Springer-Verlag, second revised edition, 1993.

[Hua98] H. Huang. Destruction of invariant tori in pendulum-type equations. *J. Diff. Eq.*, 146(1):67–89, 1998.

[Hui88] G.B. Huitema. *Unfoldings of quaisperiodic tori.* PhD thesis, University of Groningen, 1988.

[JdlLZ99] À. Jorba, R. de la Llave, and M. Zou. Lindstedt series for lower-dimensional tori. In *Hamiltonian systems with three or more degrees of freedom (S'Agaró, 1995)*, pages 151–167. Kluwer Acad. Publ., Dordrecht, 1999.

[JM99] À. Jorba and J. Masdemont. Dynamics in the center manifold of the collinear points of the restricted three body problem. *Phys. D*, 132(1-2):189–213, 1999.

[JV97] À. Jorba and J. Villanueva. On the normal behaviour of partially elliptic lower-dimensional tori of Hamiltonian systems. *Nonlinearity*, 10(4):783 – 822, 1997.

[JZ] À Jorba and M. Zou. On the numerical integration of ode by means of high-order taylor methods. preprint.

[KH98] S.-Y. Kim and B. Hu. Resurrection of an inverted pendulum. *Chaotic Dynamics*, 1998. Electronic journal: *http://xxx.lanl.gov/abs/chao-dyn/9802015v1.*

[KO00] B. Krauskopf and H.M. Osinga. Investigating torus bifurcations in the forced van der Pol oscillator. In *Numerical methods for bifurcation problems and large-scale dynamical systems (Minneapolis, MN, 1997)*, volume 119 of *IMA Vol. Math. Appl.*, pages 199–208. Springer, New York, 2000.

[Kol54] A.N. Kolmogorov. On conservation of conditionally periodic motions for a small change in Hamilton's function (in Russian). *Dokl. Akad. Nauk SSSR (N.S.)*, 98:527 – 530, 1954. English translation in Lecture Notes in Physics 93, 51–56 (1979).

[Kol57] A.N. Kolmogorov. Théorie générale des systèmes dynamiques et mécanique classique. In *Proceedings of the International Congress of Mathematicians, Amsterdam, 1954, Vol. 1*, pages 315 – 333. Erven P. Noordhoff N.V., Groningen; North-Holland Publishing Co., Amsterdam, 1957. English translation in [AM78].

[Kuz95] Y.A. Kuznetsov. *Elements of applied bifurcation theory*, volume 112 of *Applied Mathematical Sciences*. Springer-Verlag, 1995.

[Lev88] M. Levi. Stability of the inverted pendulum — a topological explanation. *SIAM Rev.*, 30(4):639 – 644, 1988.

[Lev90] M. Levi. KAM theory for particles in periodic potentials. *Ergod. Th. Dynam. Sys.*, 10:777 – 785, 1990.

[Lev91] M. Levi. Quasiperiodic motions in superquadratic time-periodic potentials. *Comm. Math. Phys.*, 143(1):43 – 83, 1991.

[LL91] S. Laederich and M. Levi. Invariant curves and time-dependent potentials. *Ergod. Th. Dynam. Sys.*, 11(2):365–378, 1991.

[LL92] A.J. Lichtenberg and M.A. Lieberman. *Regular and chaotic dynamics*, volume 38 of *Applied Mathematical Sciences*. Springer-Verlag, second edition, 1992.

[Loc99] U. Locatelli. *Contribution a l'etude de la theorie KAM: applications a la mechanique celeste et liens avec la theorie des nombres*. PhD thesis, l'Observatoire de la Côte d'Azur, 1999.

[Lun99] G. Lunter. *Bifurcations in Hamiltonian systems: computing singularities by Gröbner bases*. PhD thesis, Rijksuniversiteit Groningen, 1999.

[LW95] M. Levi and W. Weckesser. Stabilization of the inverted linearized pendulum by high frequency vibrations. *SIAM Rev.*, 37(2):219 – 223, 1995.

[McL81] J.B. McLaughlin. Period-doubling bifurcations and chaotic motion for a parametrically forced pendulum. *J. Stat. Phys.*, 24(2):375 – 388, 1981.

[Mey70] K.R. Meyer. Generic bifurcation of periodic points. *Trans. Amer. Math. Soc.*, 149:95–107, 1970.

[Mos62] J. Moser. On invariant curves of area-preserving mappings of an annulus. *Nachr. Akad. Wiss. Göttingen. Math.-Phys. Kl. II*, pages 1 – 20, 1962.

[Mos67] J. Moser. Convergent series expansions for quasi-periodic motions. *Math. Ann.*, 169:136–176, 1967.

[Mos68] J. Moser. Lectures on Hamiltonian systems. *Mem. Amer. Math. Soc.*, 81:1 – 60, 1968.

[Mos89a] J. Moser. Minimal foliations on a torus. In M. Giaquinta, editor, *Topics in calculus of variations (Montecatini Terme, 1987)*, volume 1365 of *Lecture Notes in Mathematics*, pages 62–99. Springer-Verlag, 1989.

[Mos89b] J. Moser. Quasi-periodic solutions of nonlinear elliptic partial differential equations. *Bol. Soc. Brasil. Mat. (N.S.)*, 20(1):29–45, 1989.

[MQR99] R.I. McLachlan, G.R.W. Quispel, and N. Robidoux. Geometric integration using discrete gradients. *R. Soc. Lond. Philos. Trans. Ser. A Math. Phys. Eng. Sci.*, 357(1754):1021–1045, 1999.

[MS54] J. Meixner and F.W. Schäfke. *Mathieusche Funktionen und Sphäroidfunktionen.* Springer-Verlag, 1954.

[Nei84] A.I. Neishtadt. The separation of motions in systems with rapidly rotating phase. *J. Appl. Math. and Mech.*, 48(2):133 – 139, 1984.

[New74] S.E. Newhouse. Diffeomorphisms with infinitely many sinks. *Topology*, 13:9–18, 1974.

[NST97] A.I. Neishtadt, V.V. Sidorenko, and D.V. Treschev. Stable periodic motions in the problem on passage through a separatrix. *Chaos*, 7(1):2 – 11, 1997.

[OS93] A. Olvera and C. Simó. Elliptic non-Birkhoff periodic orbits in the twist maps. *Internat. J. Bifur. Chaos Appl. Sci. Engrg.*, 3(1):165–185, 1993.

[Pös82] J. Pöschel. Integrability of Hamiltonian systems on Cantor sets. *Comm. Pure Appl. Math.*, 35(5):653 – 696, 1982.

[PS28] B. van der Pol and M.J.O. Strutt. On the stability of the solutions of Mathieu's equation. *London Edinburgh Dublin Philos. Mag.*, 5:18 – 38, 1928.

[Rob70] R.C. Robinson. Generic properties of conservative systems I, II. *Amer. J. Math.*, 92:562 – 603 and 897 – 906, 1970.

[Sim89] C. Simó. On the analytical and numerical approximation of invariant manifolds. In D. Benest and C. Froeschlé, editors, *Les méthodes modernes de la mécanique céleste*, pages 285 – 329. Goutelas, 1989.

[Sim94] C. Simó. Averaging under fast quasiperiodic forcing. In *Hamiltonian mechanics (Toruń, 1993)*, pages 13–34. Plenum, New York, 1994.

[Sim98] C. Simó. Invariant curves of analytic perturbed nontwist area preserving maps. *Regul. Chaotic Dyn.*, 3(3):180–195, 1998. J. Moser at 70.

[Sim01] C. Simó. Global dynamics and fast indicators. In H.W. Broer, B. Krauskopf, and G. Vegter, editors, *Global analysis of dynamical systems – Festschrift dedicated to Floris Takens for his 60th birthday*, pages 373 – 389. Institute of Physics Publishing, 2001.

[Ske99] R.D. Skeel. Symplectic integration with floating-point arithmetic and other approximations. *Appl. Numer. Math.*, 29(1):3–18, 1999. Proceedings of the NSF/CBMS regional conference on numerical analysis of Hamiltonian differential equations (Golden, CO, 1997).

[SS92a] J.M. Sanz-Serna. Symplectic integrators for Hamiltonian problems: an overview. In *Acta numerica, 1992*, pages 243–286. Cambridge Univ. Press, Cambridge, 1992.

[SS92b] J.M. Sanz-Serna. Symplectic Runge-Kutta and related methods: recent results. *Phys. D*, 60(1–4):293–302, 1992. Experimental mathematics: computational issues in nonlinear science (Los Alamos, NM, 1991).

[SSC94] J.M. Sanz-Serna and M.P. Calvo. *Numerical Hamiltonian problems*, volume 7 of *Applied Mathematics and Mathematical Computation*. Chapman & Hall, London, 1994.

[STa] C. Simó and D.V. Treschev. Evolution of the "last" invariant curve in a family of area preserving maps. preprint.

[STb] C. Simó and D.V. Treschev. Stability islands in the vicinity of separatrices of near-integrable symplectic maps. preprint.

[Sto50] J.J. Stoker. *Nonlinear vibrations in mechanical and electrical systems.* Interscience Publishers, New York, 1950.

[Tak74a] F. Takens. Forced oscillations and bifurcations. In *Applications of global analysis I (Sympos., Utrecht State Univ., Utrecht, 1973)*, number 3 in Comm. Math. Inst. Rijksuniv. Utrecht, pages 1 – 59. Math. Inst. Rijksuniv. Utrecht, Utrecht, 1974.

[Tak74b] F. Takens. *Introduction to global analysis.* Mathematisch Instituut, Rijksuniversiteit Utrecht, Utrecht, 1974. Lectures held at Utrecht State University, October–December, 1972, Communications of the Mathematical Institute, Rijksuniversiteit Utrecht, No. 1973-2.

[Via00] M. Viana. Dynamical systems: moving into the next century. In B. Enquist and W. Schmid, editors, *Mathematics unlimited – 2001 and beyond*. Springer-Verlag, 2000.

[Wig90] S. Wiggins. *Introduction to applied nonlinear dynamical systems and chaos*, volume 2 of *Texts in Applied Mathematics*. Springer-Verlag, 1990.

[WK85] M.I. Weinstein and J.B. Keller. Hill's equation with a large potential. *SIAM J. Appl. Math.*, 45(2):200 – 214, 1985.

[WK87] M.I. Weinstein and J.B. Keller. Asymptotic behaviour of stability regions for Hill's equation. *SIAM J. Appl. Math.*, 47(5):941 – 958, 1987.

[You90] J. You. Invariant tori and Lagrange stability of pendulum-type equations. *J. Diff. Eq.*, 85:54 – 65, 1990.

[You98] L.-S. Young. Developments in chaotic dynamics. *Notices Amer. Math. Soc.*, 45(10):1318–1328, 1998.